DEVELOPMENT AND DESIGN OF A NEAR-FIELD HIGH-ENERGY GAMMA CAMERA FOR USE WITH NEUTRON STIMULATED EMISSION COMPUTED TOMOGRAPHY

by

Amy Congdon Sharma

Department of Biomedical Engineering
Duke University

Date: November 14, 2007
Approved:

_____
Gregg E. Trahey, Ph.D., Co-Supervisor

_____
Georgia D. Tourassi, Ph.D., Co-Supervisor

_____
Calvin R. Howell, PhD

_____
Srinivasan Mukundan, Jr., Ph.D., M.D.

_____
Timothy G. Turkington, Ph.D.

Dissertation submitted in partial fulfillment of
the requirements for the degree of Doctor
of Philosophy in the Department of
Biomedical Engineering in the Graduate School
of Duke University

2007

ABSTRACT

DEVELOPMENT AND DESIGN OF A NEAR-FIELD HIGH-ENERGY GAMMA CAMERA FOR USE WITH NEUTRON STIMULATED EMISSION COMPUTED TOMOGRAPHY

by

Amy Congdon Sharma

Department of Biomedical Engineering
Duke University

Date: November 14, 2007
Approved:

_____
Gregg E. Trahey, Ph.D., Co-Supervisor

_____
Georgia D. Tourassi, Ph.D., Co-Supervisor

_____
Calvin R. Howell, PhD

_____
Srinivasan Mukundan, Jr., Ph.D., M.D.

_____
Timothy G. Turkington, Ph.D.

An abstract of a dissertation submitted in partial fulfillment of the requirements for the degree of Doctor of Philosophy in the Department of Biomedical Engineering in the Graduate School of Duke University

2007

Copyright by
Amy Congdon Sharma
2007

Abstract

A new gamma imaging method, Neutron Stimulated Emission Computed Tomography (NSECT), is being developed to non-invasively and non-destructively measure and image elemental concentrations *in vivo*. In NSECT a beam of fast neutrons (3 – 5 MeV) bombards a target, inelastically scattering with target nuclei and exciting them. Decay from this excited state produces characteristic gamma emissions. Collecting the resulting gamma energy spectrum allows identification of elements present in the target. As these gamma rays range in energy from 0.3 – 1.5 MeV, outside the useable energy range for existing gamma cameras (0.1 – .511 MeV), a new gamma imaging method must be developed. The purpose of this dissertation is to design and develop a near-field (less then 0.5 m) high-energy (0.3 – 1.5 MeV) gamma camera to facilitate planar NSECT imaging. Modifying a design implemented in space-based imaging (focus of infinity), a prototype camera was built. Experimental testing showed that the far-field space-based assumptions were inapplicable in the near-field. A new mathematical model was developed to describe the modulation behavior in the near-field. Additionally, a Monte Carlo simulation of the camera and imaging environment was developed. These two tools were used to facilitate optimization of the camera parameters. Simulated data was then used to reconstruct images for both small animal and human fields of view. Limitations of the camera design were identified and

quantified. Image analysis demonstrated that the camera has the potential to identify regions of interest in a human field of view.

Contents

Abstract iv

List of Tables ix

List of Figures x

List of Abbreviations xiii

Acknowledgements xiv

1. Introduction 1

2. Background Information 3

2.1 Elemental Composition 3

2.2 Clinical Significance of Elemental Composition 4

2.3 NSECT 6

2.4 Gamma Cameras 9

2.4.1 Current Technology 9

2.4.2 Experimental Camera Designs 11

2.4.3 Semi-Conductors – Superior Energy Resolution 12

2.4.4 RMC for spatial information 14

2.5 MLEM Reconstruction Method 15

2.6 Research Goal 19

3. The Rotation Modulation Collimator Camera 20

3.1 RMC Design 20

3.2 Prototype Camera 22

3.3 Near-Field Models 26

3.3.1 Schnopper and Hurford Model 26

3.3.2 Proposed Near-Field Model 28

3.4 Summary 36

4. Monte Carlo Simulation 39

4.1 GEANT4 39

4.2 GEANT4 Verification 42

4.3 Summary 47

5. Optimization of RMC Parameters 49

5.1 Two Collimator Design 49

5.2 Separation 54

5.3 Slat Offset 56

5.4 Collimator Material 57

5.5 Slat Height, Slat Width and Slot Width 59

5.6 Summary 65

6. Imaging Limits of Near-Field RMC Camera 67

6.1 Field of View for Small Animal Imaging (10 x 10 pixels) 68

6.1.1 Visual Inspection 68

6.1.2 Data Analysis 70

6.1.3 Effect of additional cameras on reconstruction quality 74

6.2 Field of View for Imaging Humans (25 x 25 pixels) 79

6.3 Reconstructed Image Quality Metrics 81

6.3.1 10 x 10 Image Reconstructions 84

6.3.2 25 x 25 Image Reconstructions 86

6.4 Summary 88

7. Summary, Conclusion and Future Work 92

7.1 Summary 92

7.2 Conclusion 94

7.3 Future Work 94

References 97

Biography 106

Education 106

Scholarship, Grants and Awards 106

Peer Reviewed Publications 107

Manuscripts to be Submitted 108

Conference Proceedings 108

Abstracts 111

Posters 111

List of Tables

Table 1: Differences in measured Fe and Cu content in the liver in humans and rats.....6

Table 2. RMC orientations. 25

Table 3. Comparison between Monte Carlo simulation and experimental data. 46

Table 4. One collimator vs. two collimator Monte Carlo simulation parameters.....51

Table 5. Change in modulation profile shape at different RMC configurations.....52

Table 6. RMC configuration for Monte Carlo experiment on affect of height on modulation profile. 54

Table 7. Results of modulation profile comparisons between RMC configurations with different heights. 55

Table 8. Properties of possible collimator materials. 57

Table 9. RMC configurations for test of different collimator materials.....58

Table 10. 15 different RMC configurations used to determine effect of slat height, slat width and slot width on image quality.....60

Table 11. Parameters producing 160 different RMC configurations. 62

Table 12. RMC configurations for testing 10 x 10 FOV.....69

Table 13. Monte Carlo parameters to test image quality.....82

Table 14. Monte Carlo simulation of hypothetical Homeland Security application. 95

List of Figures

Figure 1. Energy spectrum obtained from NSECT interrogation of a fixed mouse. 8

Figure 2. An 'N' shaped phantom made from iron '\' and copper '|' 9

Figure 3. Change in event transmission as collimators rotate about the z-axis. 15

Figure 4. Schematic of RMC system. 21

Figure 5. Dimensions associated with the imaging plane and collimators. 22

Figure 6. Prototype RMC. 23

Figure 7. Experimental setup including, HPGe detector, RMC and point source on an imaging plane. 24

Figure 8. Modulation profiles obtained for 511 keV gamma rays (left) and 1274 keV gamma rays (right) with the RMC at SID 50 cm and Separation 20 cm. 25

Figure 9. Schnopper and Hurford predicted near-field modulation profile. 27

Figure 10. Top: front view of collimator. Bottom: Side view of collimator depicting point source, collimators and detectors. 29

Figure 11. Illustrations of the geometry of the rotating ROA. 30

Figure 12. Modulation profiles predicted by the geometry of the collimator 33

Figure 13. Modulation profile with four distinguisihing characteristics labeled: peak location, FWHM, maximum value and minimum value. 34

Figure 14. Experimentally collected data compared to near-field model prediction from camera orientation 4. 36

Figure 15. Schematic of the GEANT4 simulation with the point source, two collimators and HPGe. 41

Figure 16. Experimental vs. Monte Carlo results for RMC orientation 4. 43

Figure 17. Side by side comparson of modulation profiles obtained by experiment and Monte Carlo simulation for both 511 keV and 1.274 MeV gamma energies.. 43

Figure 18. Modulation profiles obtained by experiment, Monte Carlo simulation and geometric model. 45

Figure 19. Angle of acceptance for various collimator slat orientations. 50

Figure 20. Simulated modulation profiles. 53

Figure 21. Modulation profiles from matching RMCs that only vary in separation. 56

Figure 22. Average FWHM (left) and peak to valley (right) of modulation profiles obtained testing various collimator slat materials. 59

Figure 23. Image quality score vs. peak to valley for 500 keV gamma rays. 63

Figure 24. Average predicted score sorted by RMC dimension. 64

Figure 25. Predicted image quality score vs. efficiency for 25, 30 mm slat height RMCs. 65

Figure 26. Point source reconstructions for a 10 x 10 pixel four camera system at the optimal radius for each pixel size. 70

Figure 27. Probability matrix parameters for a 10 by 10 pixel FOV using 4 cameras. 72

Figure 28. FOV locations for 4 camera views and 8 camera views. 74

Figure 29. FOV modulation profile symmetry for 4 camera FOV and 8 camera FOV system. 75

Figure 30. A FOV from the 4 camera and 8 camera system. 76

Figure 31. Point source reconstructions for a 10 x 10 pixel eight camera system at the optimal radius for each pixel size. 77

Figure 32. Probability matrix parameters for 1.25 cm pixels (A), 1.0 cm pixels (B) and 0.75 cm pixels (C) for both the 8 camera (solid lines) and 4 camera (dashed lines) systems. . 78

Figure 33. Line source reconstructions for a 25 x 25 pixel eight camera system at the optimal radius for each pixel size. 79

Figure 34. Probability matrix parameters for a 25 x 25 pixel FOV using 8 cameras..... 80

Figure 35. Images of a horizontal line and vertical line in a 10 x 10 FOV. 85

Figure 36. Image quality measurements comparing the different 10 x 10 systems. 86

Figure 37. Images of a vertical and horizontal line in a 25 x 25 pixel FOV. 87

Figure 38. Image quality measurements comparing the different 25 x 25 systems. 88

Figure 39. Four reconstructed images obtained from mid-field simulated data. 96

List of Abbreviations

1D: One-Dimensional
2D: Two-Dimensional
CERN: European Organization for Nuclear Research, located on Franco-Swiss border near Geneva.
CZT: Cadmium Zinc Telluride
CT: Computed Tomography
DOE: Department of Energy
FBP: Filtered Back Projection
FOV: Field of View
FWHM: Full-Width at Half-Maximum
GEANT4: Monte-Carlo simulation environment developed by CERN
HPGe: High-Purity Germanium
LSF: Line Spread Function
MCA: Multi-Channel Analyzer
MLEM: Maximum Likelihood Expectation Maximization
MTF: Modulation Transfer Function
NSECT: Neutron Stimulated Emission Computed Tomography
PET: Positron Emission Tomography
RHESSI: Reuven Ramaty High Energy Solar Spectroscopic Imager
RMC: Rotating Modulation Collimator
SNR: Signal to Noise Ratio
SPECT: Single Photon Emission Computed Tomography
TUNL: Triangle Universities Nuclear Laboratories

Acknowledgements

NSECT is the child of Dr. Carey Floyd. I honestly never thought I would work on it. Three years ago I had a meeting with Carey (to which he was late) and sat in wonder as he described this new imaging modality. The likelihood of my working with him on this wonderful, yet bizarre, project was summed up by the statue of the winged pig on his desk. Yet, I am glad I took the risk. When his cancer was deemed terminal, and I found out I would be finishing without him, again, I flashed back to that pig. In fact, the flying pig is a good theme for my entire graduate career.

I would like to thank the many people that helped get this pig off the ground.

I would not be here without my wonderful committee, who selflessly helped out with research entirely different from their own. Gina, thank you for stepping in as my advisor. You tirelessly read, read and reread my multiple manuscripts and drafts. You have checked in on me, given career advice and made sure I kept going. You have been a true mentor, advisor and friend. Gregg, the man behind the curtain, thank you for pulling the proper strings and always watching out for me. I am not sure why, but I know graduate school would have been much harder without you around. I always knew it would all work out okay as long as you were there. Calvin, thank you for keeping the physics in check and patiently educating my un-physics mind. Tim, thank you for helping keep the camera science real, dealing with those pesky reviewers and

telling terrible puns. Finally thank you Srini, for keeping this grounded in medicine and helping think the big thoughts.

A special thanks to the NSECT dream-team of Janelle Bender and Anuj Kapadia. You two have been critical in making sure NSECT kept going and have been an incredible source of ideas and critiques.

I thank the people of DAILabs for being a fantastic source of support. Especially, thanks to Brian Harrawood. You have been an invaluable resource in developing and maintaining GEANT4 and have put up with my ability to break computers by just looking at them. Through it all you have made it fun.

I thank the people of TUNL. Especially, Calvin Howell, Alex Crowell and Matt Kiser for teaching me physics and dealing with my crankiness after 24 hours locked in a concrete bunker. Your presence made the time both enjoyable and valuable. And thanks for not getting too upset when I set some equipment on fire. I would also like to thank Anthony Hutcheson and Anton Tonchev for their detector setup and knowledge.

I also thank my "shadow advisor" Uncle Chip who has supported my entire journey through the land of academia.

I thank my family for their love and support. Especially, Mom and Dad, look how far I've come from my cynical 2nd grade prediction of housewife. A special thanks to my friends for making my time in school entertaining and enjoyable.

I especially thank my husband, Navin. You have edited manuscripts that made no sense, listened to my rants and celebrated my victories. It's been a long journey and you have dealt with it every step of the way.

Last, but never least, thank you to Carey for believing in me and inspiring me. I only knew and worked with him for a short time, but in that time he instilled his passion for science, his quest for knowledge and his love of life. Working for Carey was never dull: one minute he could be explaining high-energy physics and the next telling a story of super-gluing his face to a table. He began this project and I hope that I have finished it in a fitting tribute.

1. Introduction

A new imaging modality – Neutron Stimulated Emission Computed Tomography (NSECT) – is under development to image elemental quantities and distributions nondestructively and non-invasively *in vivo*. To acquire the elemental composition information, a region of interest is illuminated with a beam of 3 – 5 MeV neutrons (referred to as "fast neutrons"). Through inelastic scatter, these neutrons excite the individual elemental nuclei, which then relax by emitting characteristic gamma radiation. Acquiring the gamma energy spectrum of this radiation enables the identification of elements within the sample. The purpose of the research presented herein is to develop a high-energy gamma camera for use with NSECT imaging.

Chapter 2 provides a brief introduction on the elemental composition of humans and of rats, the clinical significance of elemental composition, NSECT, gamma cameras, and the image reconstruction method used in this research. The chapter concludes with the research goal of the doctoral thesis.

Chapter 3 describes the design, development, and testing of a prototype camera. The camera is modeled after a space-based imaging system that operates at an infinite focus. The challenges of bringing this technology into a near-field (< 1 m) focus are discussed, including the inability of existing far-field models to describe the near-field behavior of the camera. The chapter concludes with the development of a new model to

describe the near-field behavior. This model predicts and explains the near-field behavior observed in experiments with the prototype camera.

Chapter 4 describes the development of a Monte Carlo simulation of the camera. This simulation environment is necessary to accurately model high-energy gamma interactions with the camera – the near-field model introduced in Chapter 3 can only describe ideal situations. Accurate modeling is necessary as iterating on the multiple design options through building, testing and rebuilding prototype cameras is expensive in terms of both time and monetary cost. Use of a Monte Carlo environment speeds the rate of camera design and development. Results from the Monte Carlo simulations are verified against experimental data acquired from the prototype camera.

Chapter 5 describes the optimization of camera parameters using the Monte Carlo simulation. The numerous camera configurations are discussed, and the impact of each individual factor is assessed to determine an optimal camera setup.

Chapter 6 first identifies the optimal imaging field of view and explains the limits on the camera resolution. It then provides reconstructed images using Monte Carlo simulation data for both small animal and human imaging fields-of-view. Image quality and camera efficiency are discussed along with feasibility for both imaging realms.

Finally, chapter 7 summarizes the results of this research and discusses future directions for the overall project.

2. Background Information

2.1 Elemental Composition

A review of the literature has found that many elements of biological interest have been measured in both humans [1-7] and rats [8-13].

Certain elements are vital to the body. For example, Cu and Zn are essential to central nervous system development [10, 14]. In addition, Cu helps the liver utilize Fe for hemoglobin development and plays a role in adrenaline synthesis and oxidative phosphorylation [15]. Zn is also essential for enzymatic activity, human growth [1, 16, 17] and DNA repair (along with Mg). Nucleotide excision repair requires Ni, Cd, Co, and As [18]. Other examples include Fe which is essential to humans for oxygen transport and neurological health [15] and Mn which stabilizes membrane activity [8, 15].

Some elements are essential at low levels but become toxic at high levels (e.g., Se and Sb) [17]. Studies have identified elemental imbalances that occur in conjunction with different diseases. Elemental composition studies of rat brains have shown that ischemia leads to a decrease in K and P [11-13], and radiation exposure leads to a decrease in Cl, Fe, and Zn [13]. In a seizure study, there was decreased Cu in the kidney and Fe in the brain [8]. Two studies found an increase in trace elements in the lesions

and organs of mice with skin tumors [19, 20]. A change in trace element concentration was also noted in the kidneys of mice with malignant ascites [21].

Several studies have shown that trace element concentrations in human tissue may allow differentiation between malignant and benign tissue in the breast (Al, Br, Ca, Cl, Co, Cs, Cu, Fe, K, Mn, Na, Rb, Sb, Se, Zn), prostate (Ca, Cu, Fe, Mg, Ni, Zn) and brain (B, Ba, Sr, Zn) [1, 16-18, 22-24]. These findings could be due to the elements' roles in DNA and nucleotide excision repair (As, Cd, Co, Mg, Zn) or toxicity at high levels (Cu, Se, Sb) [17, 18].

Several techniques have been utilized for determining the amount of elements within tissue samples, including: atomic absorption spectrophotometry (AAS), Rutherford backscattering analysis, inductively coupled plasma-atomic emission spectrometry (ICPA), inductively coupled plasma-mass spectrometry (ICPM), neutron activation analysis (NAA), X-ray fluorescence spectrometry (XRF) and particle-induced X-ray emission analysis (PIXE). All of these techniques require tissue samples to be prepared in specific ways that are not compatible with *in-vivo* studies [5, 11, 22, 25-27].

2.2 Clinical Significance of Elemental Composition

NSECT has the potential to non-invasively identify and map elemental concentrations within the body. As seen above, there are many elements of biological interest that would be suitable candidates for NSECT imaging in both human and

animal models of human diseases. While cancer detection is a promising application for NSECT [28], this thesis focuses primarily on iron and copper. An excess of these elements in the liver is a sign of certain diseases, and typically this excess is very large (see Table 1) [3, 16].

Two specific diseases, hemochromatiosis and Wilson's Disease, cause elemental imbalances in the liver. Hemochromatiosis is a disorder whereby inappropriate amounts of iron are absorbed by the body causing an iron overload in certain organs, especially the liver. It is brought about by specific genes, and a genetic screen is available. Genetic inducement is not the only cause, as patients with blood disorders that require frequent blood transfusions can acquire it. Therefore, those receiving multiple transfusions should be monitored for early symptoms. Wilson's Disease is genetically induced and causes copper toxicity in both the brain and the liver. There is no practical genetic screen for Wilson's disease. Early detection and treatment is desirable in both diseases, and biopsy is the "gold standard" test in both cases. Due to the lifelong nature of these diseases, there is a need for long-term monitoring, which makes biopsies less than ideal due to their invasive and painful nature [29-32].

CT and MR have been explored as non-invasive measurement techniques. CT has been shown to be insensitive to mild changes in concentrations, as well as highly sensitive to changes in fatty tissue [33]. Several groups have identified MR as a promising method [32-34]. However, others have shown that MR detection may not be

possible when the iron concentration is great enough to distort the MR signal or when fibrosis is present, thereby causing measurement errors in patients with the most severe iron overload [35]. Biopsies have also been questioned, since the elements might not be distributed evenly, causing variable biopsy results [36] . Development of a non-invasive, image-based, spectroscopic measurement technique would improve patient care and treatment.

Long–Evans Cinnamon (LEC) rats have been identified as a disease model for Wilson's disease. They have large amounts of both copper and iron in their livers, and they have a healthy counterpart: Long–Evans Agouti (LEA) rats [37-41]. These rats would be an appropriate animal model to image with NSECT, allowing the testing of NSECT's ability to detect differences in both iron and copper. Table 1 lists the normal and diseased iron and copper concentrations in the livers of both humans and rats.

Table 1: Differences in measured Fe and Cu content in the liver in both humans (μg/g dry weight) [29, 30] and rats (μg/g wet weight) [40].

	Copper (μg/g)	*Iron (μg/g)*
Normal Human	20-50	300-1400
Wilson's Disease	> 200	
Hemochromatiosis		6000-18,000
LEA (healthy rat)	2.6 ± 0.5	103.7 ± 37.5
LEC (diseased rat)	155.3 ± 38.4	188.9 ± 20.8

2.3 NSECT

Neutron Stimulated Emission Computed Tomography (NSECT) is a spectroscopic imaging technique. Fast neutrons (3 – 5 MeV) illuminate the body of

interest and scatter inelastically off of individual nuclei within the body. Inelastic scatter results in a transfer of energy from the incident neutron to the target nucleus, leaving the nucleus in an excited state. This nucleus then relaxes to its ground state by emitting the excess energy as gamma radiation (in NSECT applications the energy range is 0.4-6.5 MeV). Due to its nuclear composition, each elemental nucleus exists in a unique state and has unique excited energy levels; therefore, the energy of the gamma emission is characteristic of the nucleus of origin. The elemental composition of the body being interrogated can be determined by measuring these emissions.

These gamma ray emissions are collected by High-Purity Germanium (HPGe) detectors, which have an energy resolution of 0.1% FWHM at 1000 keV with little change over a large energy range, making them the preferred choice in high-energy spectroscopy [42]. These detectors have a large surface area (radius 3.5 cm) and function as single pixel elements; thus they provide no spatial information. As an example, an energy spectrum from NSECT interrogation of a fixed mouse is shown below (Figure 1). Further details of the mouse experiment can be found in [43].

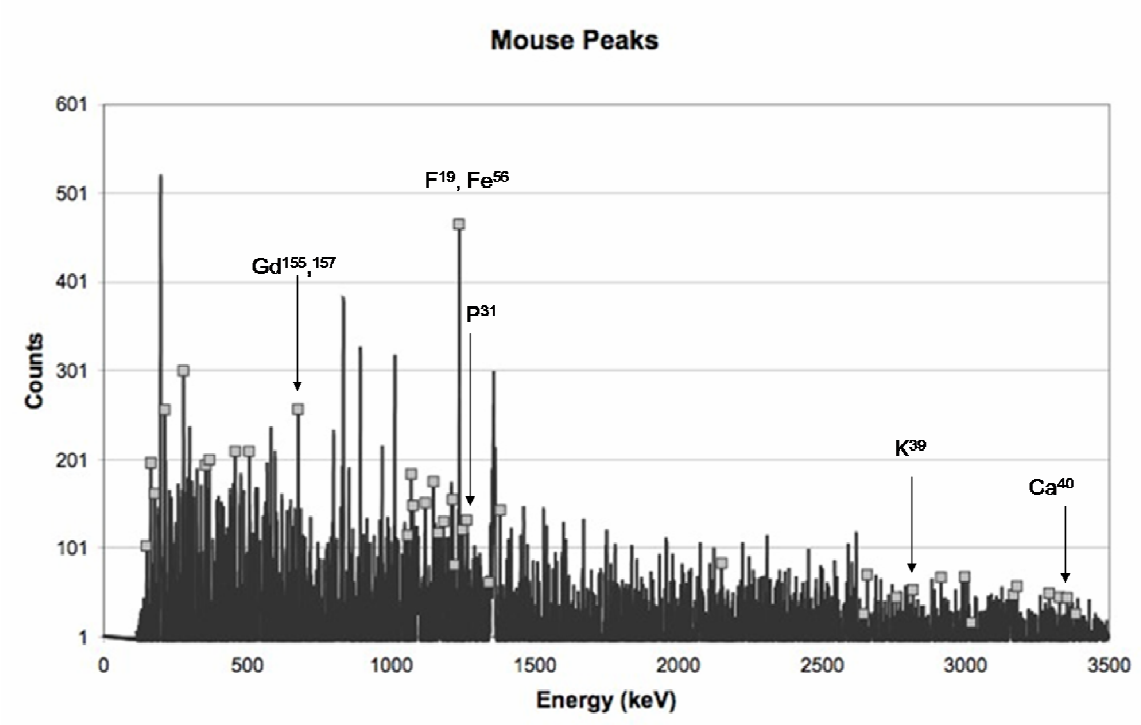

Figure 1. Energy spectrum obtained from NSECT interrogation of a fixed mouse. Energy peaks from several biologically relevant elements are labeled.

Currently, tomographic images for NSECT are created through first generation CT technology (scan a thin line, detect, translate, repeat). While this method has been proven successful (see Figure 2) [44], it limits resolution to the beam size. It is difficult, however, to reduce beam size while maintaining adequate neutron flux [45]. A possible solution is to illuminate the entire body at once and measure the gamma emissions with a position sensitive gamma camera.

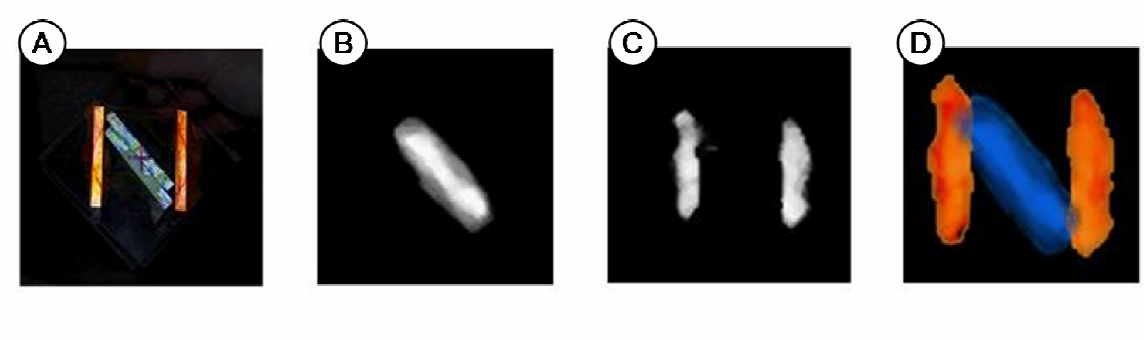

Figure 2. An 'N' shaped phantom made from iron '\' and copper '|' (A). The iron (B) and copper (C) individual NSECT reconstructions. The combined image overlaid on the original phantom (D).

2.4 Gamma Cameras

2.4.1 Current Technology

Anger cameras are currently utilized in all single-photon nuclear medicine applications including SPECT. They are composed of a large inorganic scintillator crystal (NaI) coupled to a grid of photomultiplier tubes (PMT). When a photon interacts with the detector the centroid of the PMT pulses is calculated, resulting in an estimate of the photon's interaction location. In order to create meaningful images, the incoming radiation must be collimated so that only gamma rays orthogonal to the camera face are detected. The most popular collimation pattern is a hexagonal grid, "parallel hole" collimator [46].

Anger camera imaging systems have two design compromises between spatial resolution and efficiency. The first compromise involves crystal thickness. Thicker crystals increase intrinsic efficiency but reduce spatial resolution. Intrinsic efficiency is

the ratio of the number of photons that are detected by the detector to the number that are incident on the face of the detector. This ratio is inversely related to incident photon energy; therefore, thicker crystals are required to stop higher energy photons, but as the crystal thickens the scintillator light spread increases, reducing spatial resolution [46]. The second compromise involves collimator design including septal thickness, hole diameter, and hole length. Longer and thinner holes provide greater spatial resolution but at the cost of reduced system efficiency. Collimator penetration increases with photon energy, requiring thicker collimators and thicker septa to maintain spatial resolution, which reduces system efficiency. This is an important dilemma as typical low-energy collimators only accept about 2/10,000 emitted photons [46, 47]. Most modern camera systems come with several different collimators that can be used depending on the energy of the radiotracer being imaged and the required spatial resolution [46].

PET utilizes radiotracers that create a 511 keV annihilation reaction. At this high energy, Anger cameras are not very effective; instead, PET creates images through "annihilation coincidence detection." Scintillator detectors are placed in a ring about the patient and spatial information is gathered by measuring annihilation coincidences and assuming that two gamma rays detected at approximately the same time came from the same annihilation reaction; therefore, since the photons are emitted at ~180° from each other, they are assumed to have originated on the line connecting the two detectors [46].

2.4.2 Experimental Camera Designs

To reduce costs it would be favorable to have a dual-head Anger camera that could perform both SPECT and PET imaging [48, 49]. However, this scenario would require a scintillation camera that functions well for 511 keV gamma rays. Several groups have proposed using parallel slat collimators with the standard scintillation crystal / PMT setup. The slats provide only 1D information about the body being imaged. By rotating the slats in front of the crystal/PMT setup, and obtaining count patterns at each collimator location, 2D images can be reconstructed. Parallel slats only cover one dimension; therefore, when the septa grow thicker, the resultant decrease in efficiency is only linear. In contrast, when septa grow thicker in parallel hole collimators, the growth is in several dimensions, causing the efficiency to decrease by greater than the square of the increase in collimator thickness. Also, due to the wider acceptance angle afforded by the slats, oblique rays are accepted, which allows for a longer path in the crystal, enhancing attenuation and detection. Thus, as gamma energy increases, the crystal thickness does not need to increase to maintain reasonable detection efficiency. Consequently, the camera should be more efficient at higher energies and therefore should overcome the loss in resolution that occurs when reconstructing a 2D image from 1D information. So far, this approach has proved fairly successful, especially on smaller sources, but it requires more complex circuitry and reconstruction algorithms [47, 50-54].

Standard and experimental gamma cameras utilizing scintillation crystals are not an option in NSECT imaging because at the higher gamma energies NSECT utilizes, there are no solutions to the two design compromises listed above. To effectively stop the gamma rays and achieve adequate detection efficiency, the crystals would be too thick to achieve any spatial resolution. Additionally, at 511 keV, septal penetration is approximately 50% on high-energy collimators, which already has compromised spatial resolution and system efficiency [47, 54]. This penetration would only increase with gamma energy, requiring even thicker collimators, further reducing spatial resolution and system efficiency.

2.4.3 Semi-Conductors – Superior Energy Resolution

Several groups have attempted to further improve on camera design by using room-temperature semi-conductor devices, specifically Cadmium Zinc Telluride (CZT). CZT is a semi-conductor and not a scintillator; therefore, it provides superior energy resolution. This approach increases the ability to discriminate between incident photon energies allowing the reduction of background noise caused by scattered photons (which increases resolution) and the concurrent use of two isotopes (dual-isotope imaging) [55-58].

CZT is expensive and requires that many little crystals be coupled together to form the detector face. To save costs, several groups have arranged the crystals in a

single strip with a parallel-slat collimator. The imaging principal is similar to the parallel-slat method mentioned above, as rotation of the strip detector provides information to reconstruct a 2D image [55-58]. As costs have decreased, several groups have begun using full arrays of CZT detectors. These detectors function and image in a manner similar to traditional Anger cameras, providing 2D planar images [59-61].

While room-temperature semi-conductors are becoming more popular for typical nuclear medicine uses, their energy resolution and efficiency at higher gamma energies are too poor for NSECT uses [42, 62].

Other groups have explored the use of segmented HPGe detectors to obtain position sensitive information without the use of collimators. This concept was explored in the late 1980s to early 1990s [63] and has reemerged recently utilizing pulse shape algorithms to provide up to 0.5 mm resolution in all three dimensions. These algorithms are very computationally expensive. Crystals segmented into 2 mm to 5 mm squares provide an approximate energy resolution of 1.5-2.5 keV FWHM at 1.3 MeV. They also provide about 20% efficiency [64-66].

Segmented HPGe detectors also seem a poor choice for NSECT because of their low efficiency and energy resolution equivalent to that of room-temperature semiconductor devices. They are also very expensive in both monetary cost and computation time required to determine position.

In summary, energy resolution between the energies of 50-511 keV is approximately 5%-12% FWHM for inorganic scintillators [67] and 2.5% for room-temperature semi-conductors [68]. At these same energies, HPGe semi-conductor detectors have an energy resolution of <1% FWHM. Even though energy resolution degrades with increasing incident gamma energy, HPGe detectors maintain their superior resolution advantage over the others [42]. This increased resolution comes at the cost of poorer detector efficiency. There are other disadvantages to the use of HPGe detectors: (i) they are bulky, (ii) they must be operated at low temperatures, and (iii) the detector face is a single element approximately 7 cm in diameter, eliminating its ability to provide spatial information.

2.4.4 RMC for spatial information

In 2002 NASA launched the Reuven Ramaty High Energy Solar Spectroscopic Imager (RHESSI), which captures and images high-energy X-rays and gamma-rays at energies equivalent to those that NSECT utilizes (RHESSI energy resolution is 3keV –17 MeV with a spectral resolution of ~1 keV). Here, HPGe detectors (almost identical to those used currently in NSECT imaging) are used to obtain spectral information while Rotation Modulation Collimators (RMCs) placed in front of the detectors provide spatial information. The RMCs consist of 2 parallel-slat collimators with the same phases that are placed a distance (20 – 50 cm) apart from one another. As they rotate together in

front of the detector, the collimators modulate the number of gamma rays that reach the detector (Figure 3). It is possible to reconstruct 2D images by counting the number of incident gamma rays at each energy level at each collimator angle. These modulation profiles (counts vs. collimator angle) are unique to the source's position in the imaging plane. It is important to note that the collimators do not have to attenuate all the incident photons, but rather they only need to provide sufficient attenuation to modulate the incident gamma flux [69-73].

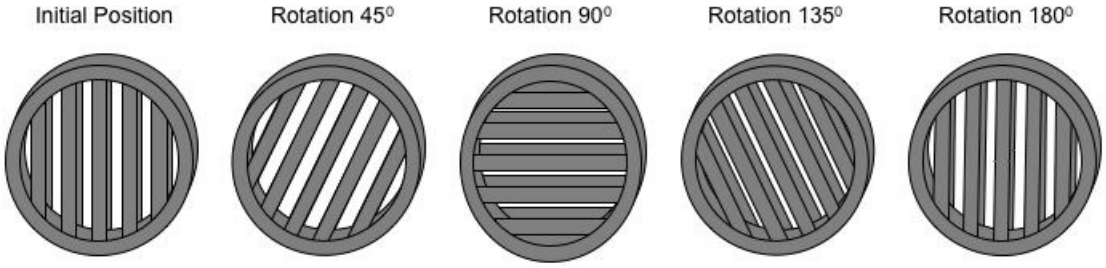

Figure 3. Change in event transmission as collimators rotate about the z-axis. Note how after one half a rotation, the collimation is identical to that of the initial position.

The RMC concept will be explained in further detail in Chapter 3.

2.5 MLEM Reconstruction Method

A standard Anger camera with a parallel-hole collimator produces 2D planar images (2D projection of a 3D object) of the radioactivity within the body. It can also be used to create CT slices in SPECT imaging by collecting planar data at many different angles around the body. Here, data from each row along the square camera head (for

instance: along the axial direction) is used to create a sinogram (signal strength at each radial position at each camera angle). Using this data, 2D images of slices along the body (i.e. transaxial slices) can be reconstructed using the inverse 2D radon transform or filtered back projection (FBP). FBP is an option in this application because the signal at each data element at each angle is assumed to be the sum of all data along a 1D line orthogonal to that detector element [74].

In Anger cameras with rotating slit collimators, the detected signal in each slit is assumed to be the sum along a 2D plane orthogonal to that slit. Again, a sinogram is formed from the signal strength at each slit at each collimator angle. Here, 2D planar images are reconstructed in much the same manner as axial slices are reconstructed in CT imaging [47]. By rotating the camera around the body and rotating the collimator at each camera rotation angle, axial slices of a 3D volume can be reconstructed [53].

In the system described herein, the data collected at each angle is the sum of a 3D volume of 2D planes orthogonal to the detector face. The goal is to reconstruct 2D planar images of activity within the body. At each collimator angle NSECT data is the sum of a 3D volume, not a 2D plane or 1D line. Here, reconstruction via back projection techniques is not an option. To create meaningful images, CT reconstruction techniques must be augmented with probabilities describing the system's behavior. In this thesis the Maximum Likelihood Expectation Maximization (MLEM) algorithm [75] is used for image reconstruction.

Outlined below is a MLEM implementation with respect to the projections obtained by the RMC:

Observed data, obs (1 x θ_I): At each energy level, the observed data is a 1D matrix consisting of the number of gamma rays counted at each collimator angle, θ_i, where *I* is the total number of angles.

Probability Matrix, P (M x θ_I): The MLEM algorithm depends on a matrix that contains the probability that the counts at each collimator angle, θ_i, originated at each pixel, *m*, where *M* is the total number of pixels in the imaging plane. This plane is perpendicular to the axis of rotation and parallel to the face of the detector. The probability matrix can be determined mathematically from the geometry of the system or by measuring or simulating the RMC response to a point source located at each pixel within the imaging plane.

Prediction, p^n (1 x M): The initial guess at the reconstructed image. This can be obtained through an initial "back projection" (multiplying the observed data by the probability matrix), or by setting each pixel to the same, non-zero, value.

The algorithm for iteration n+1 is given by (1):

$$p_m^{n+1} = \frac{p_m^n}{\sum_{\theta_i=1}^{I} P_{m\theta_c}} \sum_{\theta_i=1}^{I} \frac{P_{m\theta_i} obs_{\theta_i}}{\sum_{m=1}^{M} P_{m\theta_i} p_m^n} \tag{1}$$

If more than one RMC camera is used, the information from each camera can be combined with the following extension of the above equation:

$$p_m^{n+1} = \frac{p_m^n}{\sum_{camera=1}^{cameras} \sum_{\theta_i=1}^{I} P_{camera,m\theta_c}} \sum_{camera=1}^{cameras} \sum_{\theta_i=1}^{I} \frac{P_{camera,m\theta_i} obs_{camera,\theta_i}}{\sum_{m=1}^{M} P_{camera,m\theta_i} p_m^n} \quad (2)$$

There are several advantages to EM reconstructions. First, they are based on the Poisson nature of photon counting. When there are many counts, it is not problematic to ignore the statistical nature of the noise, but as count rates decrease, iterative approaches are more able to accommodate statistical noise, thus providing improved reconstruction quality. Second, EM algorithms are better suited to handle imperfect data through the use of the probability matrix. Third, the log likelihood of the observations given the current prediction is a natural measure of goodness. The concavity of this function guarantees that each iteration is a step toward convergence. This property implies that care must be taken when choosing the number of iterations as the algorithm is designed to converge on a single point. This is especially important for data that is noisy or from extended sources, as information may be lost or incorrectly reconstructed [75]. NSECT data has very low counts, and the imaging conditions are less than ideal; therefore, MLEM is the proper choice for NSECT reconstruction.

When applying the MLEM algorithm, the number of reconstructed pixels is chosen by the user when defining the probability matrix. This is a double edged sword.

While it is particularly beneficial for the proposed imaging system as reconstruction can be attempted when incomplete data may exist, it is impossible to make something out of nothing. Image quality may suffer if reconstruction is attempted in an under-determined system. When defining the number of pixels, the user should take into account the sources of information, such as the number of collimator angles and the number of camera views, to ensure a well conditioned system.

2.6 Research Goal

The purpose of this doctoral thesis is to develop a gamma camera suitable for use with NSECT imaging. The camera must operate in the near-field (0.5 m or less) at high-energies (0.5 – 1.5 MeV) while providing high-resolution (1% FWHM) spectroscopic images with a planar FOV. This thesis tests the feasibility of the camera for NSECT applications in human and small animal imaging. Inherent limitations of the camera designs, possible applications to homeland security and future directions for this research are discussed accordingly.

3. The Rotation Modulation Collimator Camera

The previous chapter introduced NSECT and its potential for non-invasive elemental imaging. It then established a need for a high-energy position sensitive gamma camera, as current gamma cameras do not meet the energy resolution requirements for NSECT. This chapter introduces and explains the proposed imaging solution: a RMC camera adapted from space-based technology. The gamma detector of choice (HPGe) is used to obtain the energy spectrum, while the RMC modulates the incoming gamma rays to provide spatial information.

In order to design an optimal imaging system, the functionality of the RMC must be understood in the near-field. This chapter first describes the design, development and testing of a prototype camera. It then discusses the inability of far-field models to describe the near-field behavior of the camera. Finally, a new model is developed to describe the observed near-field behavior.[1]

3.1 RMC Design

A schematic of the RMC camera is depicted in Figure 4. The object space x,y,z coordinate system is fixed at the detector face with the x,y plane (target plane) flush to the detector face and the z-axis extending out of the detector as the axis of rotation. The

[1] A majority of this chapter was published in [76, 78]

image plane is parallel to the face of the detector and positions of gamma sources on this plane are defined by their x,y,z object space location. The z-distance (SID) is measured from the face of the detector to the image plane. The z-distance between the two collimators is referred to as 'separation.' The collimator closest to the image plane is large enough in diameter to ensure that it is in the path of all incoming gamma rays. Consequently, the field of view is not limited by collimator size. With the collimator slats aligned horizontally (parallel to the x-axis), the slats are a certain 'slat width' in the y-direction and have a 'slat height' in the z-direction. The distance between the slats is referred to as the 'slot width.' The sum of the slat width and slot width is referred to as the 'pitch' [76].

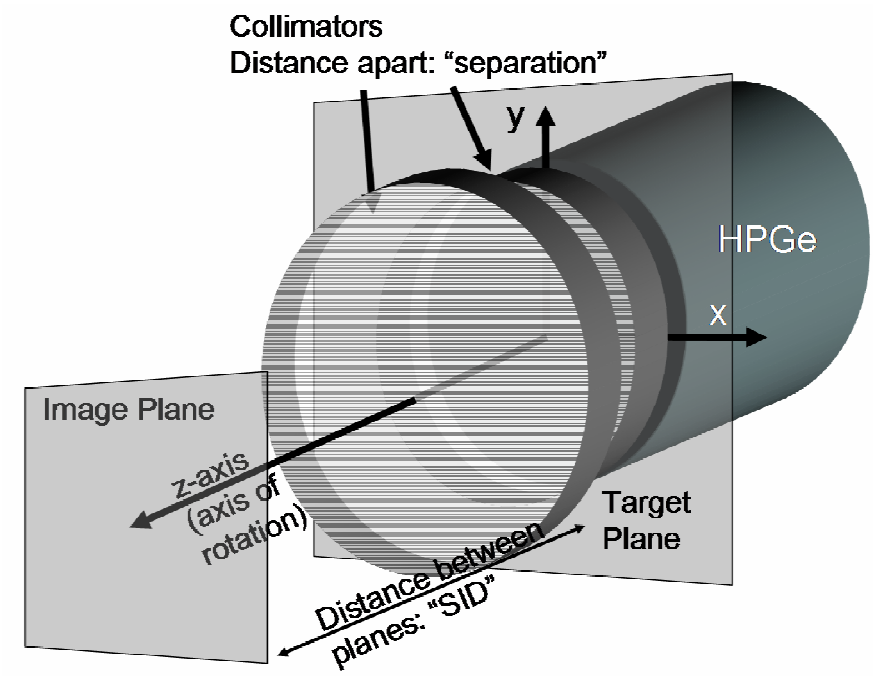

Figure 4. Schematic of RMC system.

As the RMC rotates about the z-axis, a certain number of counts are detected by the detector at each collimator angle, θ_i. The resulting observation matrix contains the number of counts at each angle. This information is used to reconstruct a 2D image consisting of *M* pixels by using a probability matrix, P, which contains the probability that the counts at each collimator angle, θ_i, originated at each pixel, *m*, located at a location (x,y or r_m,θ_m) in a plane perpendicular to the axis of rotation in space [77]. Figure 5 depicts the image plane and several collimator dimensions.

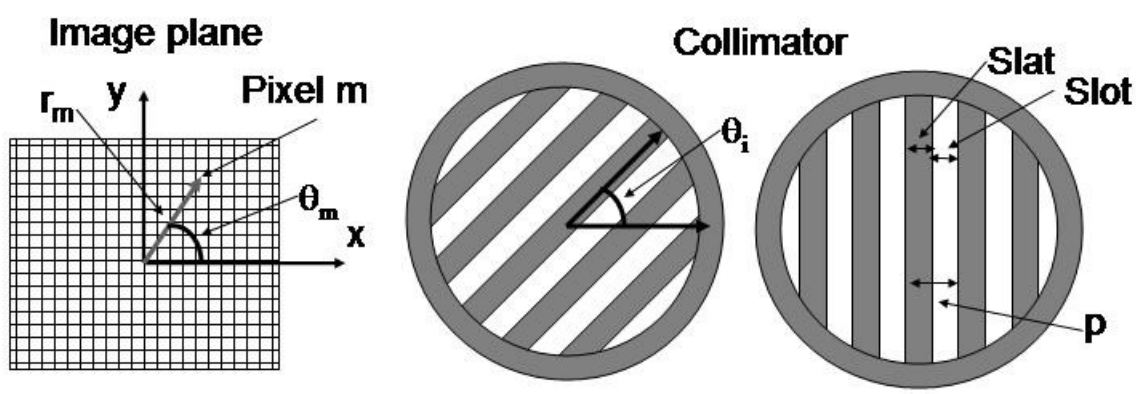

Figure 5. Dimensions associated with the imaging plane and collimators.

3.2 Prototype Camera

A prototype RMC was constructed (see Figure 6). Extruded aluminum was used to build a rectangular frame. This frame held two collimators composed of lead slats separated by plastic 'slots.' A piece of plastic PVC pipe was fitted around each end of the frame, and the entire unit then rested on rollers. To rotate the RMC, a steel ring gear was fitted around the frame and coupled to a gear that was fixed to a computer controlled

rotational stage. The prototype RMC was designed for flexibility: the distance between the collimators can be varied, and the collimator slats and slots can be exchanged for ones with different widths and heights [76].

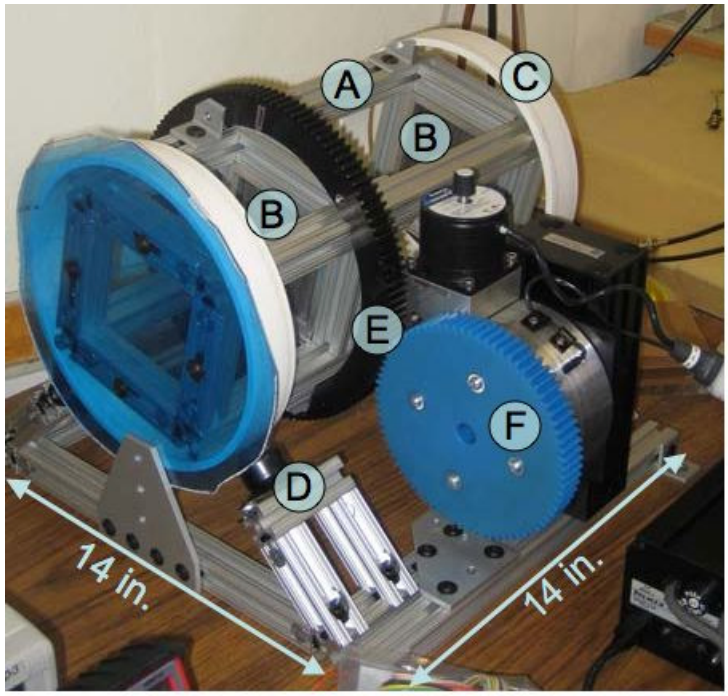

Figure 6. Prototype RMC. A rectangular frame (A) holds the 2 collimators (B), which are made of lead and plastic. These slats and slots can be switched out or slid along the frame to test different configurations. The frame (A) is fitted inside PVC pipe (C) which allows the RMC to roll on rollers (D). A metal ring gear (E) is coupled to a plastic gear (F) mounted to a rotational stage to provide controlled rotation.

To test the RMC's ability to modulate gamma rays, a 17.9 μCi point source of ^{22}Na (which emits both 0.511 MeV and 1.274 MeV gamma rays) was positioned at various locations within the x,y image plane. Measurements were taken with an HPGe detector located directly behind the rear collimator of the RMC. The RMC orientation and point source locations are listed in Table 2. For each RMC orientation, modulation

profiles were obtained for four different point source locations by recording the number of gamma rays detected in a two-minute timeframe at 10° intervals between 0° and 180°, resulting in 19 measurements per location. Figure 7 is a picture of the experimental setup [76].

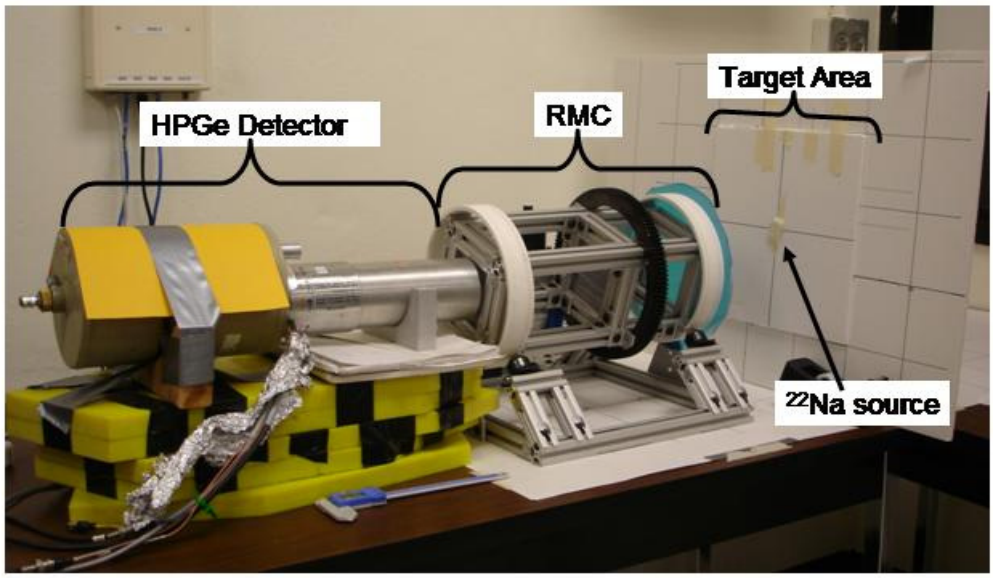

Figure 7. Experimental setup including, HPGe detector, RMC and point source on an imaging plane (the poster board).

The prototype camera successfully modulated the incoming gamma rays. The following behavior was observed. There was no modulation when the point source was located at the axis of rotation; when the radius between the point source and the axis of rotation increased, the modulation profiles thinned. The modulation profiles for the 1.274 MeV gamma rays were less distinct than those for the 0.511 MeV gamma rays. This is due to an increased gamma ray penetration of the lead slats. Figure 8 depicts

modulation profiles from RMC orientation 4 (SID 50 cm, separation 20 cm) for the four different point source locations and is representative of the results obtained from the four different RMC orientations [76].

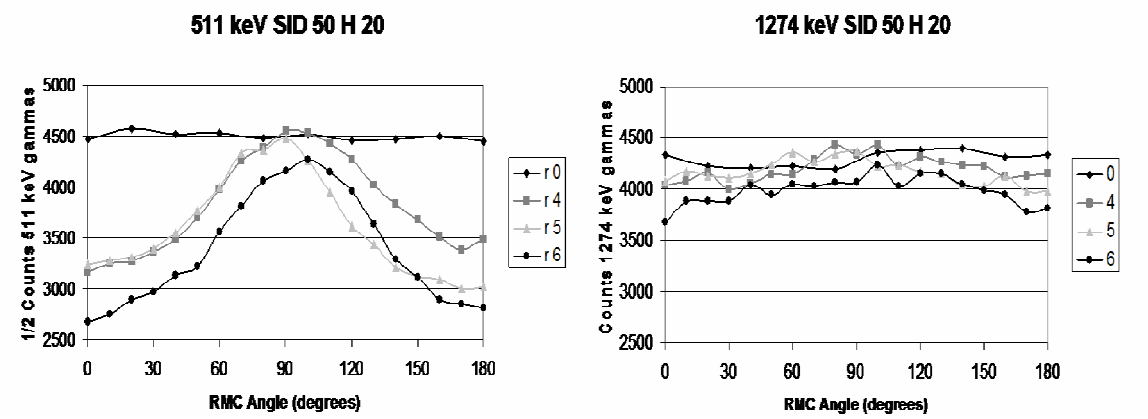

Figure 8. Modulation profiles obtained for 0.511 MeV gamma rays (left) and 1.274 MeV gamma rays (right) with the RMC at SID 50 cm and separation 20 cm. To aid visual comparison the 0.511 MeV counts have been halved. Error bars are approximately the same height as the markers.

Table 2. RMC orientations. Constant parameters were: slat width: 0.5mm, slot width: 1.0mm, slat height: 15mm and point source energy: 0.511 MeV and 1.274 MeV. The point source was always located along the y-axis, so the y-axis location was also a measure of the source's radius from the axis of rotation.

RMC Orientation	*Distance to Detector (cm)*	*Separation Between Collimators (cm)*	*Point Source Location (radius, cm)*
1	40	10	0, 4, 5 and 6
2	40	20	0, 3, 4 and 5
3	50	10	0, 5, 6 and 7
4	50	20	0, 4, 5 and 6

3.3 Near-Field Models

3.3.1 Schnopper and Hurford Model

A geometric model for the far-field application of the RMC was developed by Schnopper, et al. [73] and Hurford, et al. [69]. F_{im} describes the probability of a signal being generated from a point source located at position, m, when the collimator is at angle, θ_i.

$$F_{im} = \frac{1}{4}\left[1 + \frac{8}{\pi}\cos\left(\frac{2\pi \tan^{-1}\left(\frac{r_m}{SID}\right)\cos(\theta_i - \theta_m)}{\tan^{-1}\left(\frac{pitch}{separation}\right)}\right)\right] \tag{3}$$

where r_m is the radius of the point source from the axis of rotation on the imaging plane, *SID* is z-distance between the imaging plane and the detector, θ_m is the angular position of the point source on the imaging plane, *pitch* is the slat and slot width added together, and *separation* is the distance between the two collimators [78].

An initial study was performed using the Schnopper and Hurford model to conduct a near-field simulation and reconstruction of images [77]. Figure 9 depicts near-field modulation as predicted by this model.

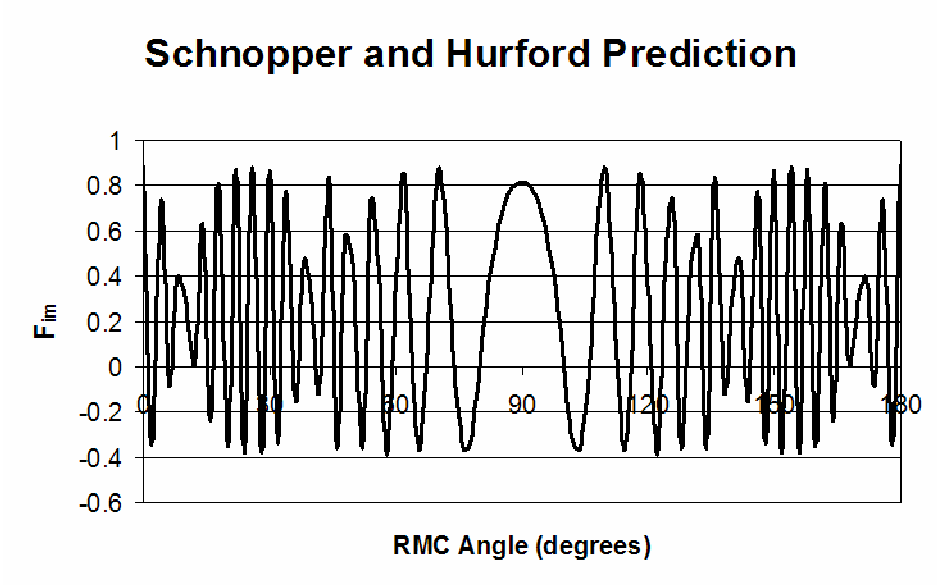

Figure 9. Schnopper and Hurford predicted near-field modulation profile for camera configuration 4 (SID 50 cm, separation 20 cm, pitch 0.15 cm).

It is apparent that the near-field behavior predicted by (3) does not match the behavior observed from testing with the prototype camera. This is because many assumptions that are valid for a focus of infinity (as is assumed in space-based imaging) are no longer valid in the near field. In the near-field the incoming gamma rays cannot be assumed to be in parallel. The model becomes invalid in the near-field when the angular pitch of the collimator ($\tan^{-1}(r_m/SID)$) becomes less than the angular distance between the source and the detector ($\tan^{-1}(pitch/separation)$). When this occurs, the bottom of the cosine expression in (3) is less than the top, causing rapid fluctuations in the calculated value of F_{im} over a 180° collimator rotation [78]. A new model is necessary to accurately describe the near-field behavior.

3.3.2 Proposed Near-Field Model

This section proposes a new near-field gamma camera model. This model was developed for this thesis to accurately describe the geometry of the proposed RMC imaging system and it is used to verify experimental and simulated behavior.

First, let us assume a point source located on the axis of rotation. Gamma rays can penetrate the entire length of the collimator in the vertical direction, but only a certain distance, $2l$, in the horizontal direction. The parameter l is calculated as shown below (4), by adding a similar triangle created by the first collimator to that created by the second collimator. Essentially, l is the distance dictated by the geometric angle of acceptance defined by the collimator's slots and slats [78].

$$l = (SID - separation)\frac{slot\ \ width}{slat\ \ height} + separation\frac{slot\ \ width}{slat\ \ height} \tag{4}$$

This distance, $2l$, and the vertical distance, $2v$, define a rectangle of acceptance (ROA).

Figure 10 illustrates the model geometry. The top picture shows the front-on view of the collimator, as seen from the perspective of a point source. The rectangle of acceptance is drawn overtop. The bottom picture shows the point source, collimators (light color indicates slots, dark color indicates slats) and HPGe detector as seen from the side. The geometric acceptance angle dictates the distance in the horizontal direction, l, that the rays can pass through the collimator. In a non-ideal model, the distance $2l$ would be affected by high energy gamma rays penetrating the slats [78].

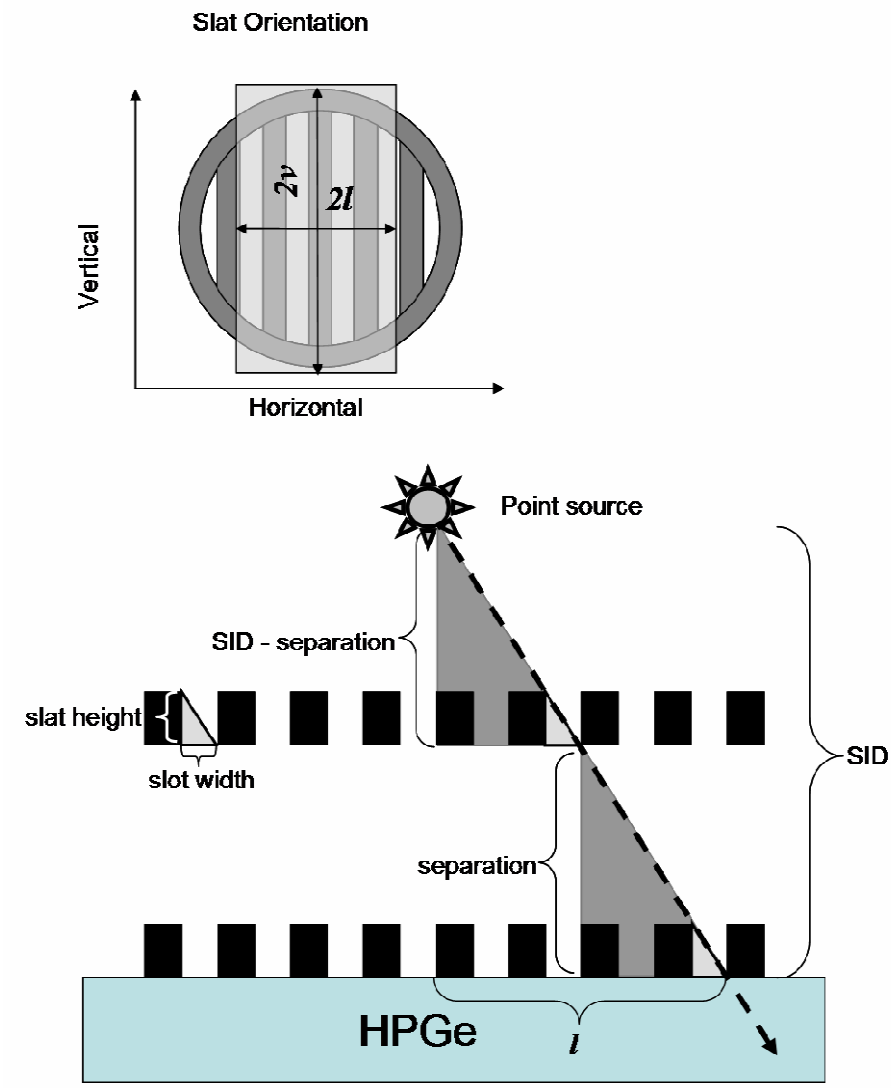

Figure 10. Top: front view of collimator. Bottom: Side view of collimator depicting point source, collimators and detectors.

As the collimators rotate, this ROA continues to have the same area, and rotates like a propeller pinned to the collimator. The same area of the detector is visible to the point source at all collimator angles. Thus, no modulation occurs for point sources located along the axis of rotation [78].

Let us also assume that the length of the ROA extends to infinity in the vertical direction, $2v$, but remains fixed at $2l$ in the horizontal direction. As the collimator rotates, the ROA sweeps out an area of acceptance in space. An off-axis point source will only be able to "see" the detector when it is inside the ROA. The farther away the point source is (in terms of either SID or radial distance on the imaging plane), the less time it will remain inside the ROA because each angular step translates into a larger arc. The above concept is illustrated in Figure 11A which shows the rectangle of acceptance sweeping out an area of acceptance in space. The further away the point source is, the less time it will remain inside the ROA. At 0° points A and B are inside the rectangle, at 20° only point B is inside and at 45° both points are outside [78].

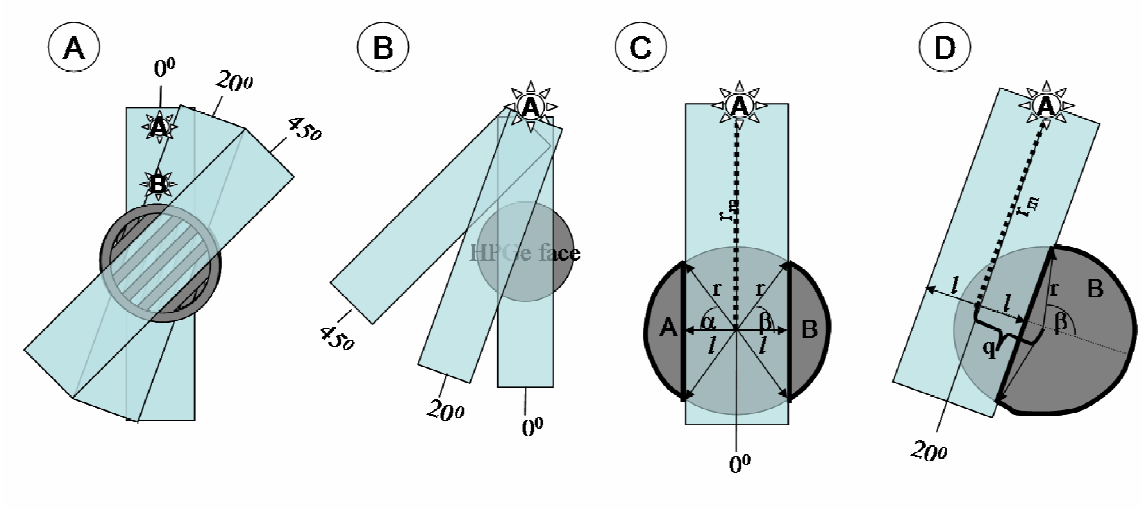

Figure 11. Illustrations of the geometry of the rotating ROA.

This view is binary, as either the point source "sees" the detector or it does not. The resulting modulation profile would be a square wave, with cutoffs at zero once the

point source is outside the ROA. However, this is not the case. Once a source is located inside the rectangle of acceptance, the modulation profile begins to slope upward from baseline, reaching its maximum when the angle of the collimator (θ_c) is equal to the angle of the point source (θ_m) [78].

For such a profile to occur, let us assume that the axis of rotation of the ROA is pinned to the point source, instead of to the center of the collimator. This is akin to rotating the point source and leaving the camera fixed, rather than rotating the collimator and leaving the point source fixed (Figure 11 A vs. B). This alternate view depicted in Figure 11B shows the area of the detector the point source can "see" as the ROA rotates about the point source. Figure 11C shows the geometry determining the area of the detector face "seen" when the collimator is aligned with the point source (maximum area). Finally, Figure 11D shows the model geometry as the ROA rotates [78].

The number of gamma rays detected from the point source is proportional to the area of the detector face that is covered by the ROA and can be calculated in the following manner:

$$\theta = \left|\theta_m - \theta_C\right| \tag{5}$$

$$q = r_m * \sin\theta \tag{6}$$

$$\alpha = \begin{cases} 2\cos^{-1}[(q+l)/r] \text{ if } (q+l) \leq r \\ 0 \text{ otherwise} \end{cases} \quad (7)$$

$$\beta = \begin{cases} 2\cos^{-1}[(l-q)/r] \text{ if } \mathrm{abs}(l-q) \leq r \\ 2\pi \text{ otherwise} \end{cases} \quad (8)$$

$$F_{im} = \pi r^2 - \tfrac{1}{2} r^2(\alpha - \sin\alpha) - \tfrac{1}{2} r^2(\beta - \sin\beta) \quad (9)$$

Note: area of a semicircle defined by angle ϕ and radius r, is defined: $\tfrac{1}{2} * r^2 * (\phi - \sin\phi)$

$$r_S = \sqrt{SID^2 + r_m^2} \quad (10)$$

$$S_{im} = \frac{F_{im}}{4\pi r_S^2} \quad (11)$$

where S_{im} is the area (in terms of the solid angle) that can be "seen" by a point source located at pixel, m, (which is defined in the imaging plane by radius, r_m, and angle, θ_m) when the collimator is at angle θ. F_{im} is equal to the area of detector face minus the area of semicircle A minus the area of semicircle B. SID is the z-distance between the detector face and imaging plane; θ is the relative angle between the point source and the RMC; q is the distance between the centerline of the rectangle of acceptance and center of the detector; α and β are the angles that define the semicircles A and B (Figure 11 C & D) [78].

The modulation profiles predicted by the geometric model confirm trends that were observed in the experimental data. Moving the point source further away in the z-direction will increase the area of detector that the point source can see, but this is negated by the decrease in solid angle (see Figure 12 A vs. B) resulting in a modulation

profile with a smaller peak when the source is farther away. Additionally, by keeping the angular location (θ_m) the same but changing the radial distance (r_m) of the source from the axis of rotation, the modulation profile becomes thinner as the radius increases (Figure 12C). When the radius is kept the same but the angular location of the source is changed, the modulation profile shape remains the same, but the location of peak changes to correspond with θ_m (Figure 12D) [78].

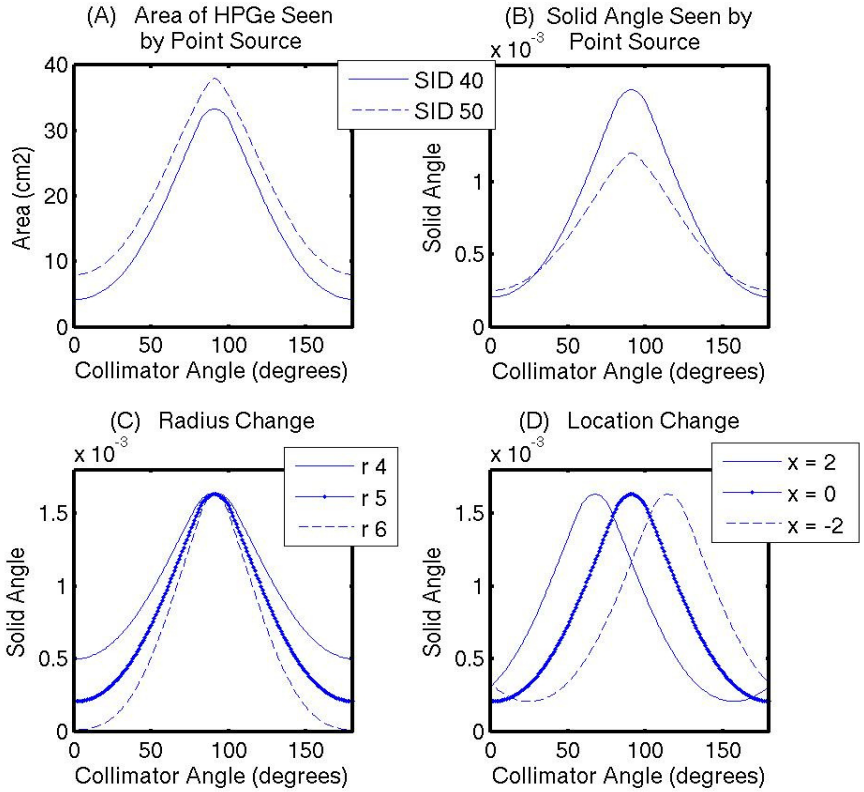

Figure 12. Modulation profiles predicted by the geometry of the collimator. (A) The area of the detector seen by a source 40 and 50 cm away and (B) the matching solid angle seen by each source. Note how more area is seen by the SID 50 cm source, but less solid angle. (C) Shows the effect of keeping the angular location the same and changing the radius from 4 to 6 cm, while (D) shows the effect of keeping the radius the same and changing the angular location of the point source.

Using the above observations, four characteristics of the modulation profile have been identified: peak location, FWHM, maximum and minimum value (see Figure 13). These vary depending on the point source's location in space, causing a modulation profile to be unique to a location. As reconstruction of images depends on the ability to distinguish between neighboring pixel's modulation profiles, a profile with a thin FWHM and large maximum to minimum value would provide both differentiation and signal strength.

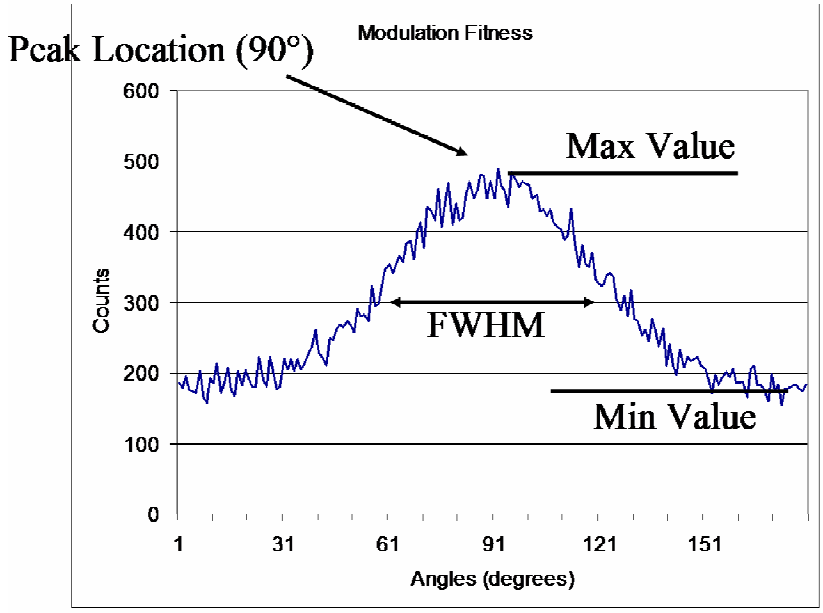

Figure 13. Modulation profile with four distinguishing characteristics labeled: peak location, FWHM, maximum value and minimum value. These characteristics will vary depending on the location of the gamma source.

The geometric model is an idealized model and not a prediction of absolute modulation profile shape. It addresses only the basic pattern of modulation by only

accounting for the distance from the source to the detector, the source's location on the imaging plane, and slot width and slat height. A more definitive model would take into account all RMC design parameters including slat width, collimator separation, collimator alignment, and high-energy gamma ray penetration of the collimator slats. However, the development of a near-field model is necessary in order to understand the geometric basis of RMC functionality in the near-field. Figure 14 shows a comparison between the near-field model and the experimentally collected data. As shown, taking into account all the other variables does not change the overall modulation profile behavior as the peak number of counts will occur where predicted by the model, and the basic modulation profile curve will remain the same. The largest difference between a modulation profile predicted by this model and one generated by an actual RMC is caused by penetration of the slats by the high-energy gamma rays. This penetration causes the "floor" of the modulation profile to rise while the peak counts remain essentially the same. Thus, as the gamma energy increases, the peak in the modulation profile is lost in the background noise [78].

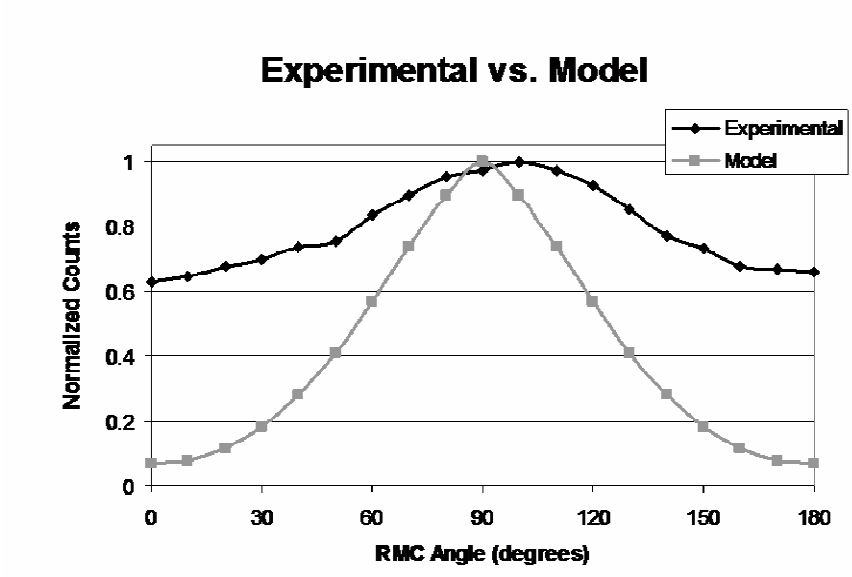

Figure 14. Experimentally collected data compared to near-field model prediction from camera orientation 4 (SID 50 cm, separation 20 cm, pitch 1.5 cm).

3.4 Summary

This chapter presented a basic overview of the RMC camera. Then the design, construction, and testing of a prototype was covered. While the modulation profiles were wide and barely visible for the 1.274 MeV gamma rays, it is encouraging that any modulation profile was visible when using slats 0.5 mm in width by 15 mm in height. These slats were comprised of a small amount of lead and should be easily penetrated by high-energy gamma rays. To reconstruct images, however, absolute collimation of the incident gamma rays is not necessary, only adequate modulation. If some modulation was achieved using those slats, it should be possible to identify reasonable collimator parameters that provide adequate modulation for reconstruction and

maintain reasonable camera efficiency within the expected energy range of NSECT (0.3 and 1.5 MeV) [76].

Once an adequate RMC orientation is identified, future generations of cameras can be constructed taking into account the lessons learned from the prototype camera. Specifically (i) the aluminum frame and steel ring gear were too bulky and attenuated some the gamma rays and (ii) the small area of the first collimator limited the field-of-view. The distance of the source from the axis of rotation is limited by the ratio of SID to separation multiplied by the difference between the radius of the collimator and radius of the detector face. Gamma rays from sources located greater than this distance away from the axis of rotation would come over the top of the first collimator and only be attenuated by the second. Many modifications can be incorporated into the next generation RMC design such as a less bulky, less attenuating frame and drive mechanism and a larger first collimator that permits an adequate FOV [76].

Experimentally acquired data did not match far-field models presented in the literature, and these existing models fail in the near-field. A new near-field model to explain RMC behavior in the near-field was developed. Due to the model's inability to account for septal penetration, this model should not be used to determine the dimensions of a functional RMC, as the largest design challenge will be to determine an RMC design that provides enough stoppage so that the modulation profile peak remains

visible above the background. Chapter 4 will describe the development of a Monte Carlo model that can overcome the near-field model's shortcomings.

4. Monte Carlo Simulation

The previous chapter described near-field data acquired from experimental testing of the RMC and the geometric model to justify the modulation behavior. However, this geometric model is unsuitable for use in identifying useable RMC parameters, as it cannot account for septal penetration. This chapter describes the development of a Monte Carlo simulation of the RMC in GEANT4. This simulation environment will facilitate careful optimization of the RMC parameters for NSECT applications.[2]

4.1 GEANT4

GEANT4 is a Monte Carlo simulation package developed by CERN for applications in high-energy physics, specifically the modeling of interactions between high energy particles and matter [79]. GEANT4 is used for NSECT Monte Carlo modeling because of its ability to track interactions of high-energy neutrons in matter. Our research group recently published a manuscript verifying GEANT4's ability to successfully model the NSECT interrogation environment [80]. Modeling of the RMC camera involves a different set of parameters than the typical NSECT setup consisting of: neutron source, target and HPGe detectors. For the research described in this thesis a

[2] Note: a majority of this of this chapter is drawn from [76]

GEANT4 model world is developed that consists of a gamma ray source, RMC and HPGe detector. The gamma ray source produces gamma rays between 0.5 and 1.5 MeV which interact with the material in the RMC and the HPGe. GEANT4's particle interaction libraries will be able to simulate septal penetration and allow for accurate RMC modeling.

The GEANT4 toolkit is a collection of C++ class libraries and data libraries [79]. A common C++ code base was established for all NSECT applications to build upon [80]. A flexible model world is built on top of this code base consisting of the gamma ray source, RMC collimators (modeled as slats floating in space) and an HPGe detector (Figure 15). The collimators are modeled simply as slats to reduce simulation complexity and run-time. In reality, a collimator support structure would be necessary, but it will be constructed from a material with low attenuation properties. The advantage of this flexible model is that it only has to be compiled once. The user can specify and change specific variables at run time without re-compiling the model. This simulation allows for changes to the following collimator dimensions (slat width, slot width, slat height, collimator separation, distance to source (SID), slat material and collimator offset), as well as point source location and gamma ray energy. To ensure no gamma rays go over the top of the first collimator the outer radius of the collimators has been expanded. The image plane is not physically limited by the outer dimensions of the collimators [76].

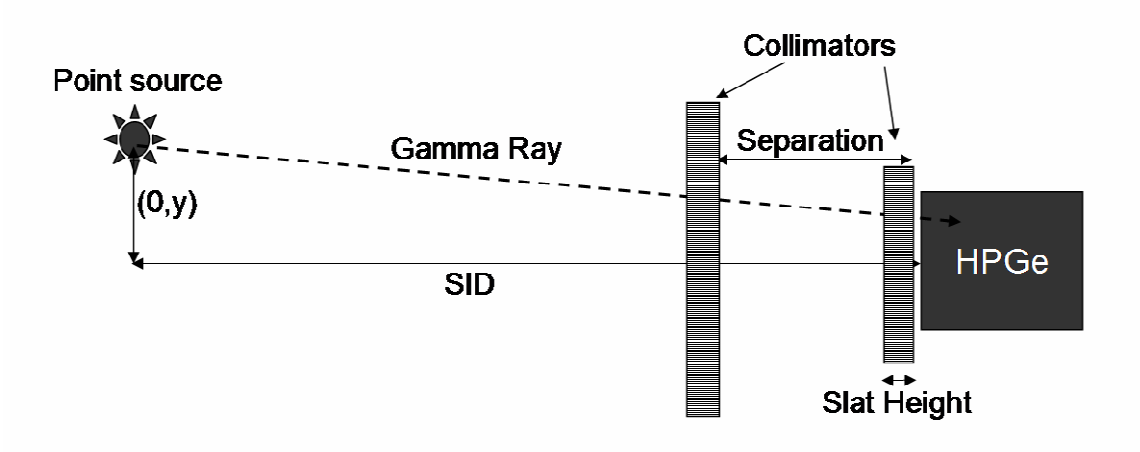

Figure 15. Schematic of the GEANT4 simulation with the point source, two collimators and HPGe.

The simulation proceeds as follows:

An ideal gamma point source emits gamma rays in all directions, with only a small fraction reaching the detector. To save simulation time, the gamma rays emitted from the point source are aimed only in the direction of the detector. However, if they were aimed solely at the detector face, the solid angle of the emitted gamma rays would decrease as the SID increased. This solid angle inconsistency would prevent comparison of modulation profiles obtained for gamma sources at different locations. The solid angle is held constant by aiming the gamma rays at an expanding target plane located at the face of the detector (see Figure 4 in Chapter 3). This target plane increases in size as the point source moves away from the detector and gamma rays follow a path from the source to a randomly selected location on the target plane. This expanding target plane

ensures that a detector located 5 cm away sees four times the number of gamma rays as one located 10 cm away [76].

4.2 GEANT4 Verification

To compare the GEANT4 simulations to the experimental data, simulations were conducted with both 0.511 MeV and 1.274 MeV point sources generating 100,000 counts at each collimator angle from 0° to 180° in 10° increments. The simulations were conducted in the same configurations as used to test the prototype (see Table 2 in chapter 3) [76].

The Monte Carlo simulation produced similar modulation profiles to those obtained experimentally. Accurate modeling of both 0.511 MeV and 1.274 MeV gamma rays was achieved (see Figure 16 and Figure 17) [76].

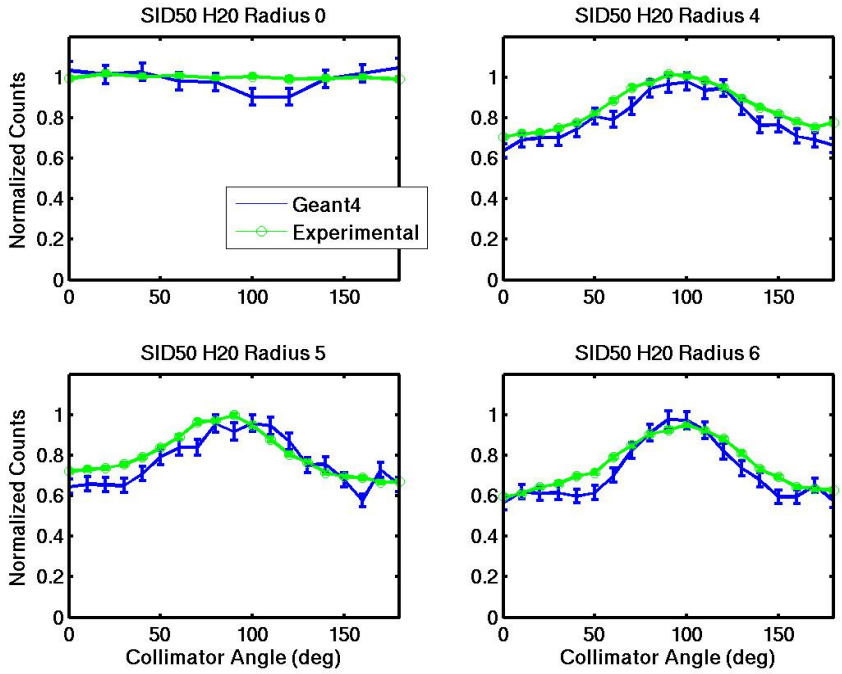

Figure 16. Experimental vs. Monte Carlo results for RMC orientation 4 (SID 50 cm, separation 20 cm, gamma ray energy 511 keV) at four different radii. There were more experimental counts than simulated data counts resulting in error bars located inside the data marker for the experimental data.

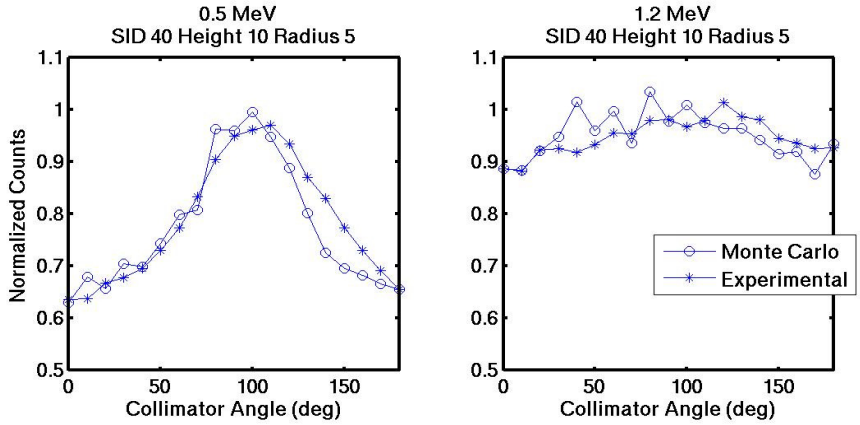

Figure 17. Side by side comparison of modulation profiles obtained by experiment (*) and Monte Carlo simulation (o) for both 511 keV (left) and 1.274 MeV (right) gamma energies. The data is from RMC orientation 1 (SID 40 cm, separation 10 cm) with the point source located at a radius of 5 cm.

In Figure 16 and Figure 17 visual comparisons of the experimental and Monte Carlo results show that similar profiles are obtained. Septal penetration in both the experiment and simulation results in less distinct modulation profiles for the 1.274 MeV gamma rays. In Figure 17 the distinct peak seen in the 0.511 MeV data is hardly visible for the 1.274 MeV data [76].

The modulation profiles from the experimental, Monte Carlo and geometric model [78] are shown in Figure 18. The figure shows modulation profiles for SID 40 cm and SID 50 cm, normalized to the SID 40 counts. Note how the peaks of all three profiles are aligned, but that only the experimental and Monte Carlo data are similar because the geometric model is unable to account for penetration of the lead slats. The figure also reflects the decrease in counts that occurs when the source is moved farther away from the detector. From 40 cm to 50 cm, $1/r^2$ decreases 36%; correspondingly, the peak counts decrease about 30% [76].

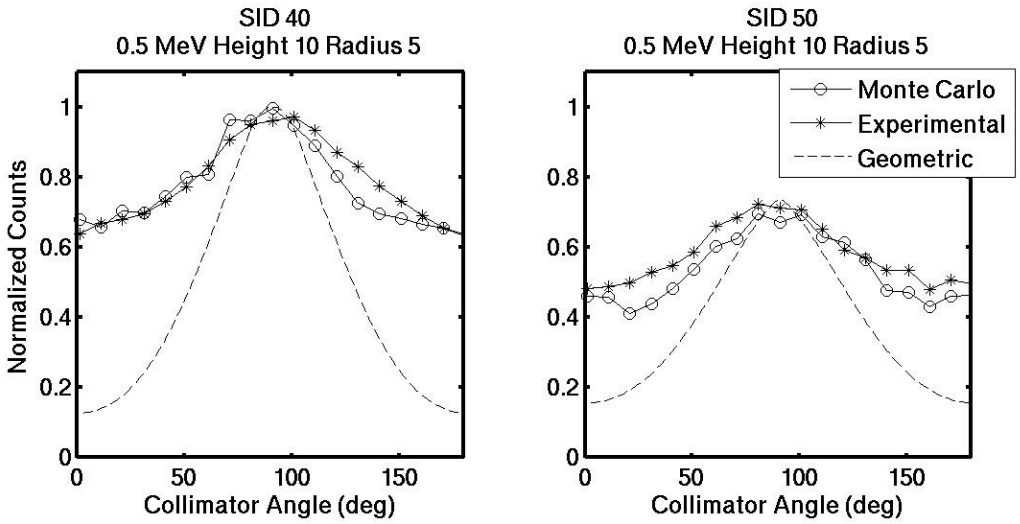

Figure 18. Modulation profiles obtained by experiment (*), Monte Carlo simulation (o) and geometric model (--) of a point source located at a 5 cm radius and an SID of 40 cm (left) and 50 cm (right). The data from each SID 50 data set was normalized by the maximum counts from the SID 40 cm data. The RMC geometry: separation 10 cm, slat height 1.5 cm, slat width 0.05 cm and slot width 0.1 cm.

The geometric model predicts that no modulation will occur when a point source is located on the axis of rotation. This is also the maximum number of counts that can be obtained from a point source located anywhere on a plane parallel to the front face of the detector located a certain SID away. For each RMC orientation in Table 2, the counts were recorded for a point source located on the axis of rotation and the average of these counts were used to normalize the modulation profiles obtained from other point source locations at that RMC orientation. This allowed numerical comparison between the simulation and experimental data. The counting error was propagated through normalization resulting in normalized experimental counts: $E \pm \sigma_E$ and normalized

simulated counts: $S \pm \sigma_S$. Count rates are considered to have an error of $\pm\sigma$ where σ is defined as the square root of the counts [76].

The number of overlapping data points (defined as a point plus or minus its error) was counted for each data set and the percentage of overlapping points calculated. For point source locations not on the axis of rotation there were 19 data points (1 every 10°) while for sources on the axis of rotation there were only 10 data points (1 every 20°). Better agreement was seen for the 1.274 MeV data than for the 0.511 MeV data with only 2 data sets matching below 68% (one standard deviation). Results are shown in Table 3 [76].

Table 3. Comparison between Monte Carlo simulation and experimental data. Percent overlap over 68% (i.e. greater then one standard deviation) is highlighted in gray.

SID (cm)	*Separation (cm)*	*Radius (cm)*	*% Overlap 0.5 MeV*	*% Overlap 1.2 MeV*
40	10	0	80	80
		4	73.7	84.2
		5	63.2	89.4
		6	21.1	15.8
40	20	0	70	70
		3	36.8	94.7
		4	52.6	68.4
		5	57.9	78.9
50	10	0	80	90
		5	63.2	84.2
		6	78.9	84.2
		7	52.6	47.3
50	20	0	100	70
		4	52.6	89.4
		5	68.4	78.9
		6	52.6	89.4

4.3 Summary

This chapter described the development of a Monte Carlo simulation. In order to determine an adequate RMC geometry, the simulation must accurately model real-world performance. The Monte Carlo simulation produced similar modulation profiles to those obtained experimentally. In both the experimental and simulated data, the modulation profiles were less distinct for the 1.274 MeV gamma rays than for the 0.511 MeV. This is expected because higher energy gamma rays have greater penetrating power. Additionally, a decrease in overall counts was observed as the source was moved farther away from the detector, as expected [76].

While there was a visual similarity between the Monte Carlo and experimental data, the data analysis found that the data sets for a wide range of implementation parameters matched below one standard deviation. This indicates a less than ideal match. There are many factors that would prevent a closer match between the experimental and simulated data. In the prototype the slats and slots were not perfectly aligned, the slots were comprised of plastic and not air, the aluminum frame and ring gear attenuated some of the gamma rays. Additionally, the 0.511 MeV gamma rays from ^{22}Na were not from a specific point, but were instead generated by the annihilation reaction which causes an inherent blur. Separately, all these discrepancies are expected to have minimal effects on the measured modulation profiles. The next chapter will discuss the system tolerance for slat alignment and initial results show a high tolerance

for offset. High-energy gamma rays and not significantly attenuated by plastic. The frame and gear were not in the flight path of a majority of the incident gamma rays. The inherent annihilation blur is on the order of millimeters. However, when all of these discrepancies are combined, the net result will be experimental modulation profiles that are slightly different from those generated in an ideally configured simulation. A large majority of the mismatched camera orientations and point source locations were with the 0.511 MeV gamma rays. These gamma rays are more likely to be modulated than the higher energy 1.274 MeV gamma rays. Thus, camera orientation inconsistencies are more likely to be significant factors for the 0.511 MeV gamma rays than the 1.274 MeV gamma rays [76].

Despite these disparities, the Monte Carlo simulation environment is an adequate tool for use in identifying RMC parameters that can be used to image gamma rays in the near field. The RMC has eight parameters (SID, separation, slat height, slat width, slot width, field-of-view, slat alignment and slat material) that all affect modulation profiles and consequently, image reconstruction quality. Iterating through these parameters in a simulation environment is a more practical and efficient technique to establish a RMC design that functions in the energy range of interest and provides images feasible for clinical applications. Chapter 5 will cover the optimization of the above parameters using this Monte Carlo simulation [76].

5. Optimization of RMC Parameters

The last two chapters described experimental RMC testing, the development of a geometric model and then the development and verification of a Monte Carlo simulation environment. In this chapter, the geometric model and the Monte Carlo simulation will be used to determine an optimal RMC design.

Before determining an optimal design, the advantage of the two collimator system is addressed. Then, six system parameters are optimized: height, slat offset, slat material, slat height, slot width and slat width.[1]

5.1 Two Collimator Design

Before addressing the rest of the RMC design, it is important to understand how two separated collimators function differently from a single collimator. In the geometric model, the calculation of the region of acceptance does not depend on one or two collimators. It appears that a one-collimator design with slat height, x, will have the same angle of acceptance as a two-collimator design with slat height, $x/2$, (thereby having the same overall slat height). However this is not the case. Figure 19 shows the possible collimator intercepts for a gamma originating on the axis of rotation. These intercepts were adapted from [54]. For a one-collimator RMC there are two possible slat

[1] Several optimization techniques were presented at [82].

orientations: the gamma ray source can be on axis with a slat or a slot. For a two-collimator RMC there are four possible orientations, with the gamma ray source on axis with a slot or slat coupled with aligned or unaligned slats. As the illustration demonstrates, the angle of acceptance fluctuates depending on the location of the gamma ray source, the location of the collimator slats, and the number of collimators. In the two-collimator design, if the gamma ray passes through the first collimator, it then must also pass through the second. As the first collimator is closer to the gamma ray source than in a one collimator system, the angle of acceptance through the first collimator is smaller. Additionally, the gamma ray must be on the proper trajectory to pass through the second set of slats. This effectively tightens the angle of acceptance and allows fewer gamma rays to reach the detector face; therefore, a two collimator design should produce modulation profiles with a smaller FWHM.

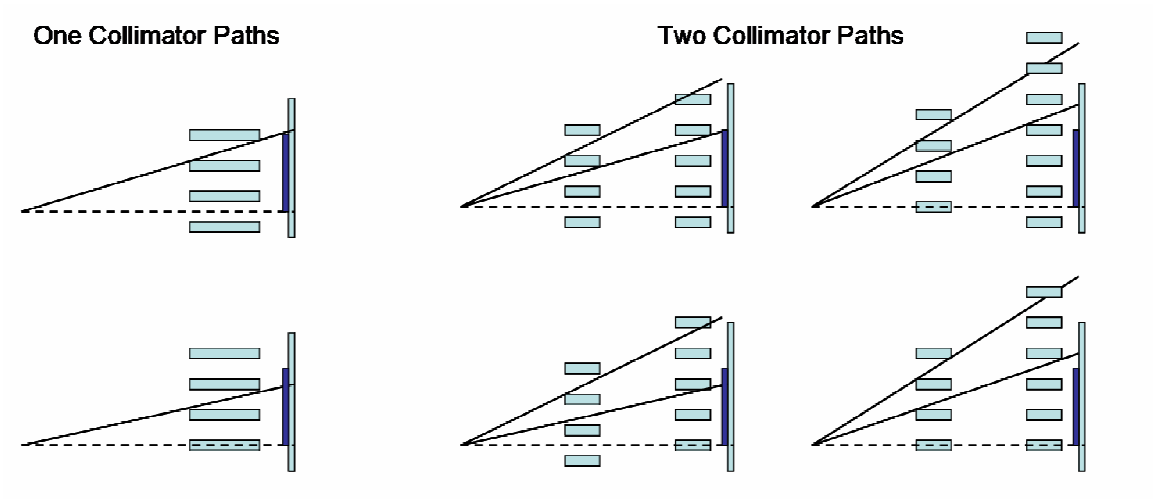

Figure 19. Angle of acceptance for various collimator slat orientations. Note how allowable gamma paths fluctuate depending on orientation.

To determine the impact of two collimators vs. one collimator of twice the slat height, a Monte Carlo simulation was run with the parameters listed in Table 4.

Table 4. One collimator vs. two collimator Monte Carlo simulation parameters.

Parameter	*Value*	
Collimator angles	0° to 180° in 2° increments	
Gamma events at each angle	10,000	
Point source location	x = 0, y = 5 cm	
Point source strength	1 keV, 500 keV, 1 MeV	
Slot width	1.5 mm	
SID	10 cm	
Slat width	1.5 mm	
Separation	0 cm	5 cm
Slat Height	3 cm	1.5 cm

Three different set of simulations were run. Each time varying one of three RMC parameters as the rest were held constant to the dimensions listed above. The SID was varied at 10, 15 and 20 cm; the slat width was varied at 1, 1.5 and 2 mm; the slat height was varied at 1, 1.5 or 2 cm (2 collimators) or 2, 3 or 4 cm (1 collimator). The maximum number of counts (*max*), peak to valley height (*PV*) and FWHM was measured for each modulation profile (see Figure 13 in Chapter 3). Then, the difference between the two collimator and one collimator data was calculated. In Table 5 below:

$$\Delta\ counts = \frac{\max_2 - \max_1}{\sqrt{\max_2 - \max_1}} \tag{13}$$

$$\Delta\ PV = \frac{PV_2 - PV_1}{\sqrt{PV_2 - PV_1}} \tag{14}$$

$$\Delta\ FWHM = FWHM_2 - FWHM_1 \tag{15}$$

where *1* denotes the one-collimator RMC and *2* denotes the two-collimator RMC. The $\Delta counts$ and ΔPV are calculated in the above manner to take into account counting errors caused by the Poisson nature of counting noise.

Table 5. Change in modulation profile shape at different RMC configurations.

Changing RMC variable	*1 keV*			*500 keV*			*1 MeV*		
	Δ *counts*	Δ *PV*	Δ FWHM	Δ *counts*	Δ *PV*	Δ FWHM	Δ *counts*	Δ *PV*	Δ FWHM
SID (cm)									
10	-2.22	-2.22	-4	1.18	1.22	-14	0.78	0.97	-26
15	-2.98	-2.98	0	-0.79	-0.80	-2	-0.08	0.06	-34
20	-3.42	-3.80	2	-0.68	-0.88	4	0.05	0.0	14
Slat width (mm)									
1	-0.81	-0.81	-10	1.67	1.59	-12	0.35	0.59	-12
1.5	-2.22	-2.22	-4	1.18	1.22	-14	0.78	0.92	-26
2	-4.48	-4.48	-6	0.60	0.93	-18	0.43	0.98	0
Slat Height (cm)									
2	-3.69	-3.69	-7	0	0.28	-2	-1.0	-0.34	-2
3	-2.22	-2.22	-4	1.22	1.22	-14	0.78	0.94	-26
4	-1.58	-1.58	-10	3.38	2.73	-20	1.83	1.49	-12

At 1 keV when there is no septal penetration, the one-collimator design is more efficient (ΔPV and $\Delta counts$ are negative – indicating more gamma rays reached the detector with the one-collimator design) and has a larger FWHM. However, as gamma energy increases and septal penetration increases, ΔPV and $\Delta counts$ become positive indicating that the two-collimator model allows more gamma rays to reach the detector. This increased efficiency occurs while the FWHM remains thinner for the two-collimator design. This finding indicates a more efficient camera, with a tighter peak in the

modulation profile which is preferable in collimator design. The above results can be seen in Figure 20 below. Note in the 1 MeV case that the modulation profile for the two-collimator design is more distinct than those from the one-collimator design. In summary, a two-collimator model behaves differently then a one-collimator model and is preferred for NSECT imaging due to its superior performance at higher gamma energies.

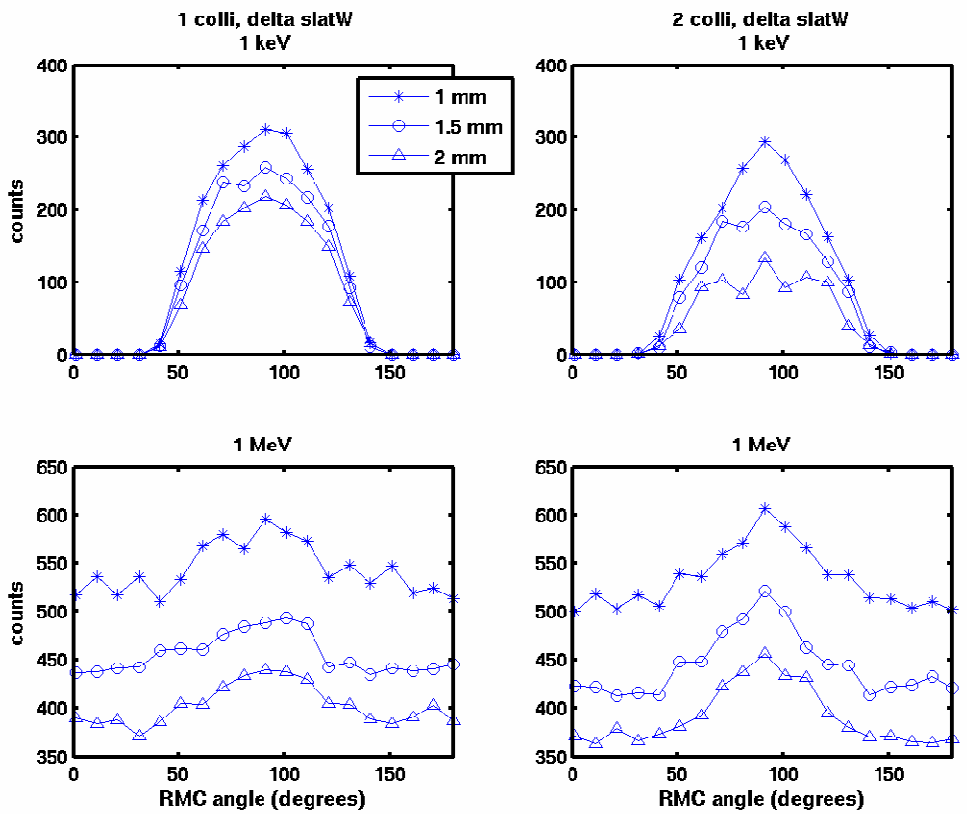

Figure 20. Simulated modulation profiles. Left column plots are from a RMC with one collimator twice the slat height as the two collimator design on the right column. Top row plots are with 1 keV gamma rays and bottom row plots are with 1 MeV gamma rays.

5.2 Separation

The experimental data obtained from the prototype camera showed an apparent trend that the collimator separation had no real effect on modulation profile. To examine this further the Monte Carlo simulation was run with parameters listed in Table 6 below.

Table 6. RMC configuration for Monte Carlo experiment on affect of separation on modulation profile.

Parameter	*Value*
Collimator angles	0° to 180° in 10° increments
Gamma events at each angle	10,000
Point source location	x = 0, y = 4, 5, 6 cm
Point source strength	500 keV
Separation	5, 10, 20 cm
SID	Height + 5 to 30 cm in increments of 5 cm
Slat height	2 cm
Slat width	1, 2, 3 mm
Slot width	Slat width to 4 mm in increments of 1 mm
Offset between slats	Offset, aligned

The above parameter range provided 594 modulation profiles consisting of 19 data points each. Of these, 108 RMC configurations were identical except for a variation in separation between 5, 10 and 20 cm. These grouped data sets were then compared to determine similarity. For each grouped data set the number of points that overlapped within one standard deviation (where standard deviation is the square root of the number of counts) was calculated for each modulation profile comparing separation 5 to

separation 10, separation 10 to separation 20, and separation 20 to separation 5 individually and finally all three separations together. If greater then 68% of the points in a modulation profile set overlapped, the sets were considered a match. Results are shown in Table 7 below.

Table 7. Results of modulation profile comparisons between RMC configurations with different separations.

Sets	*# Match at > 68%*	*% total*
5 to 10	108	100
10 to 20	97	89.8
20 to 5	97	89.8
All 3 match	71	65.7

A larger number of data points overlap between any two modulation profiles than between all three; however, a majority of the grouped sets had overlapping modulation profiles. Figure 21 is an example of modulation profiles from grouped RMC configurations. Due to both visual and numerical comparison, the conclusion is reached that the distance between collimators has little effect on modulation profile shape. Using this knowledge, a separation of 5 cm is chosen so that the SID may be as close as possible to the detector to increase efficiency.

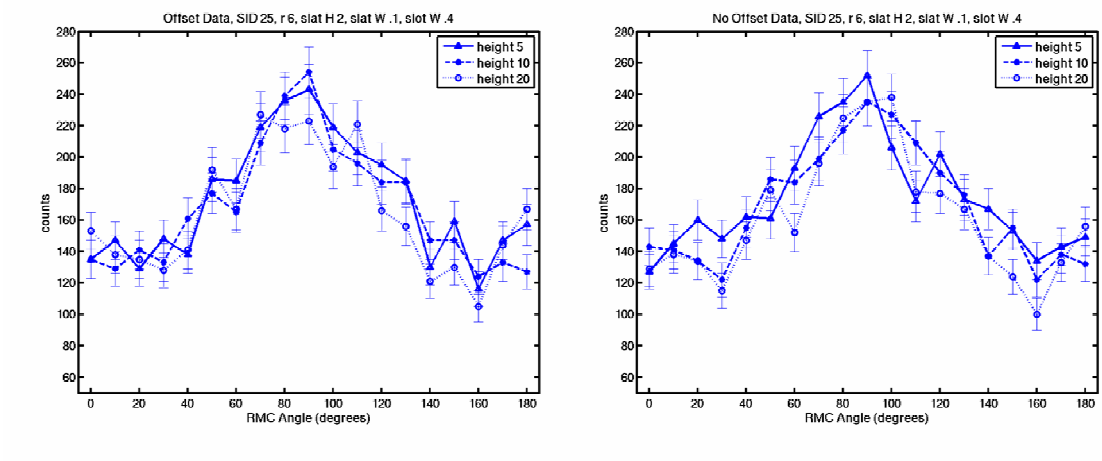

Figure 21. Modulation profiles from matching RMCs that only vary in separation (5, 10 and 20 cm). Pictured at left is data from RMCs with offset slats and at right is data from aligned slats.

5.3 Slat Offset

Using the data set generated for section 5.2, the effect of offset vs. aligned slats was also studied. There were 297 pairs of RMC configurations that varied only slat alignment (offset or not). Again, for each modulation profile pair the number of overlapping data points was calculated. The total number of pairs with over 68% overlapping data points was found to be 284 of 297, or 95.6%, indicating a similarity between the pair. This similarity is noticeable when comparing the left and right plots in Figure 21. It is concluded that slat offset has minimal effect on the modulation profile shape. Offset slats are chosen to more realistically mimic imperfections in collimator construction.

5.4 Collimator Material

There are several low-melting point lead alloys available. One use for these alloys is in radiation oncology to build custom fitted patient shielding. As these materials are readily available, easily molded and already used in shielding, they were tested against solid lead as possible collimator slat materials. There is the possibility they may improve and simplify construction of future RMCs.

The following materials, shown below in Table 8, were tested:

Table 8. Properties of possible collimator materials.

Name	*Composition*	*Equivalent Z*	*Density (g/cm^3)*
Low 158	Bismuth – 58% Lead – 26.7% Tin – 13.3% Cadmium – 10%	81.5	9.57
Low 203	Bismuth – 52.5% Lead – 32% Tin – 15.5%	77.6	9.69
Low 217-440	Bismuth – 48% Lead – 28.5% Cadmium – 14.5% Antimony – 9%	74.76	10.13
Low 255	Bismuth – 55.5% Lead – 44.5%	82.5	10.43
Lead	Lead – 100 %	82	11.34

A Monte Carlo simulation was run with the parameters listed below in Table 9:

Table 9. RMC configurations for test of different collimator materials.

Parameter	*Value*		
Collimator angles	0° to 180° in 5° increments		
Gamma events at each angle	10,000		
Point source strength	500 keV		
SID (cm)	11, 19		15
Point source location (x,y) (cm)	(4,4) (4,12) (12,4) (12,12)		(8,8)
Separation (cm)	5		
Slat height (mm)	15	15	20
Slat width (mm)	1	1.5	2
Slot width (mm)	3	4	2
Offset between slats	aligned		

Twenty-seven modulation profiles were generated for each collimator material and the peak to valley and FWHM were calculated for each. Additionally, the number of overlapping data points from each material's modulation profile to the lead's modulation profile was calculated.

Figure 22 shows a comparison between the average FWHM and peak to valley for each material. While lead appears to have a smaller FWHM and a higher peak to valley, which is advantageous, all fall within the error of the other materials. However, when the number of overlapping data points were calculated, only the low 255 modulation profiles matched those from lead (70% of the profiles matched within one standard deviation). The rest of the materials produced no overlapping profiles. This finding is expected as none of the tested materials had a higher density than lead and only low 255 had a higher equivalent Z. Gamma stopping power is directly proportional

to both the Z and the density of the material. For these reasons, lead will remain the slat material of choice; it appears to perform better, is denser and is only 0.5 lower in equivalent Z.

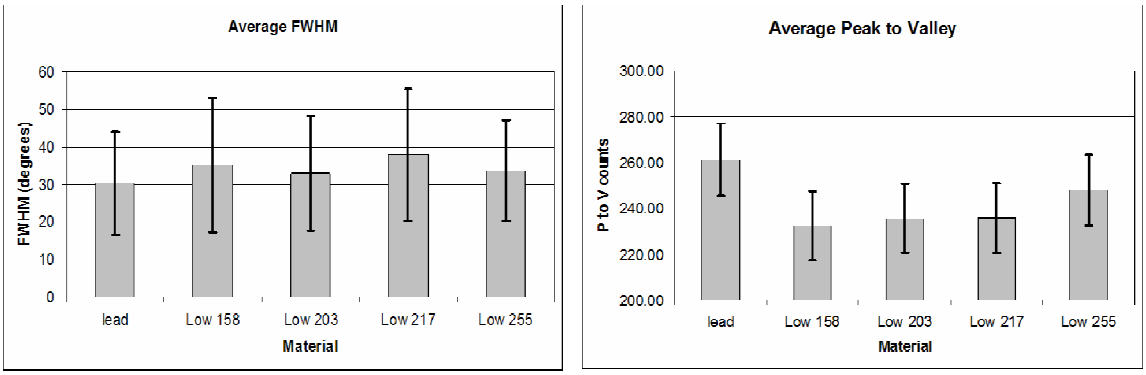

Figure 22. Average FWHM (left) and peak to valley (right) of modulation profiles obtained testing various collimator slat materials.

5.5 Slat Height, Slat Width and Slot Width

Initial testing demonstrated that there was no simple way to distinguish between the individual effects of slat height, slat width and slot width on modulation profiles. For example, reconstructing images from RMCs where only the slat height was varied resulted in different trends when another variable was changed and then the slat height variance repeated. These results suggest that the slat height, slat width, and slot width are correlated variables. Thus, these variables need to be optimized simultaneously.

First, the effect of modulation profile shape on reconstruction quality had to be determined. A complete probability matrix (modulation profiles from each pixel in the

entire 10 x 10 imaging plane) was generated for 15 different RMC orientations. They are listed in Table 10 below.

Table 10. 15 different RMC configurations used to determine effect of slat height, slat width and slot width on image quality.

Parameter	*Value*		
Collimator angles	0° to 180° in 5° increments		
Gamma events at each angle	10,000		
Point source strength	500 keV		
SID (cm)	13		
Separation (cm)	5		
Offset between slats	unaligned		
Field of View	3-13 cm x 3-13 cm (1 cm pixels)		
Setup Number	Slat height (mm)	Slat width (mm)	Slot width (mm)
1	10	2	2
2	20	1	2
3	20	2	2
4	20	2	3
5	20	2	4
6	20	1	4
7	20	3	4
8	20	4	4
9	25	2	3.5
10	25	2	4
11	25	3	4
12	30	1	1.5
13	30	1.5	1.5
14	30	2	2
15	30	2.5	3

Point source reconstructions were done at four locations within the image plane: (4,4) (4,12) (12,4) and (12,12). For each reconstructed image, three variables were

measured: (i) *range*, the minimum pixel value subtracted from the maximum pixel value, (ii) *spread*, an average of the point spread function in both the x and y direction, and (iii) *rank*, position of point source in sorted list of reconstructed pixel values (i.e. if the point source was located at (4,4) and that corresponding pixel in the reconstructed image was the brightest, its rank was 100). Each image was given a score based on the range, spread and rank of each reconstructed image and the score was directly proportional to the image quality.

For each full data set, the FWHM, maximum value and minimum value were measured in the modulation profiles from points (4,4) (4,12) and (12,12). A series of regressions were performed in Matlab [81] to determine which combination of modulation profile parameters best predicted the score of the reconstructed image. Only two parameters (average peak to valley and the ratio of the minimum values of (12,12) to (4,4)) were necessary to produce an accurate regression. The computed R^2 term for the regression was 0.88 and the two-tailed p-value < 0.01; indicating a good regression. For the 1 MeV data, three parameters (average peak to valley, minimum of (12,12) and minimum of (4,4)) were necessary to produce an accurate regression. Here R^2 was 0.76 and the p-value was <0.01, again indicating an accurate regression.

Second, with the regression model that predicted image quality based on modulation profile shape completed, Monte Carlo simulations were run producing

modulation profiles for three points, (4,4), (4,12) and (12,12) at 160 different RMC configurations, listed below in Table 11.

Table 11. Parameters producing 160 different RMC configurations.

Parameter	*Value*
Collimator angles	0° to 180° in 5° increments
Gamma events at each angle	10,000
Point source strength	500 keV, 1 MeV
SID (cm)	11, 19
Separation (cm)	5
Offset between slats	unaligned
Slat Height (mm)	10 by 5 to 30
Slat Width (mm)	0.5 by 0.5 to 3
Slot Width (mm)	Slat width by 0.5 to 4

Using the regressions developed above, the predicted image quality score was calculated for each RMC setup. Figure 23 depicts the predicted score vs. the peak to valley (PV) measurement of the modulation profiles (a measure of efficiency) for the 500 keV data. There is a clear inverse relationship between the two, which is expected, as the relationship is the standard collimated gamma camera tradeoff [46]. Further data analysis was performed to determine an acceptable tradeoff between the two.

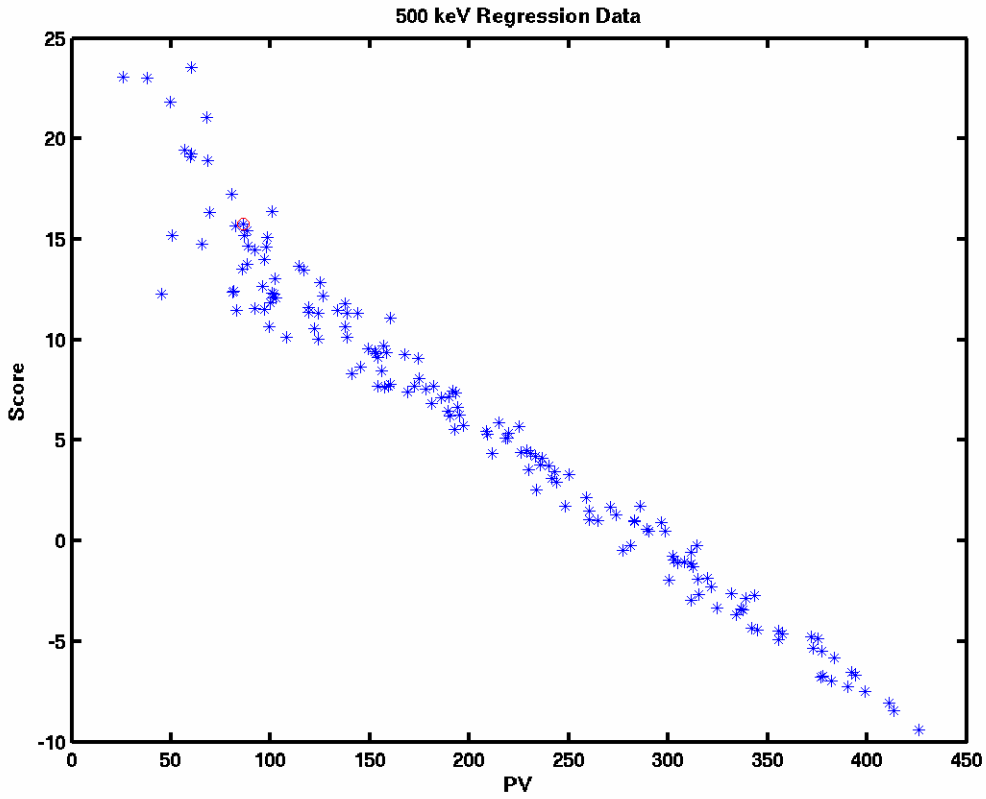

Figure 23. Image quality score vs. peak to valley for 500 keV gamma rays. There is a clear inverse relationship between image quality and camera efficiency.

Figure 24 depicts the average predicted scores sorted by slat height, slat width and slot width for both 500 keV and 1 MeV data. There is a distinct trend in the slat height data and while a trend is seen between score and slot width, it is within the error bars. Both trends confirm that as efficiency decreases, by either increasing the slat height or decreasing the slot width, the score increases. Due to the distinct correlation between slat height and predicted image quality score, images and modulation profiles were visually inspected to confirm findings. Visual inspection of the 1 MeV gamma energy

data found that modulation profiles from RMCs with less the 25 mm slats were unrecognizable and mainly noise. Using this input, the field was narrowed to RMC designs from either 25 or 30 mm slat heights. Figure 25 shows the score vs. efficiency plots for both the 500 keV and 1 MeV data for only 25 mm and 30 mm slat height RMCs. Many designs with reasonable efficiency and predicted scores for one energy level performed poorly for the other. After sifting through the results, a design was chosen that provides a reasonable tradeoff between efficiency and the predicted image quality score for both 500 keV and 1 MeV gamma rays (slat height 30 mm, slat width 3 mm, slot width 3.5 mm).

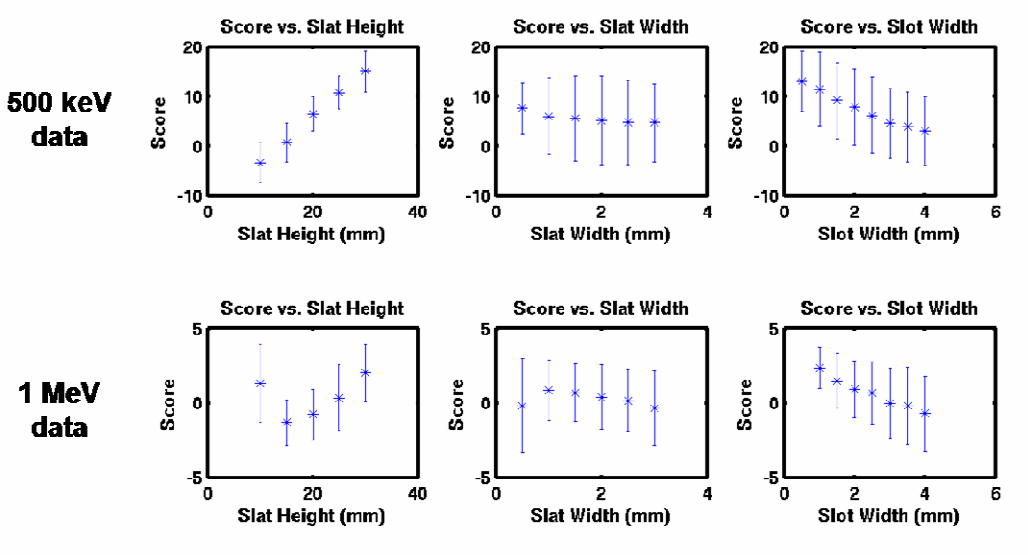

Figure 24. Average predicted score sorted by RMC dimension. Top: 500 keV data, bottom: 1 MeV data. Left: sorted by slat height, middle: sorted by slat width, right: sorted by slot width.

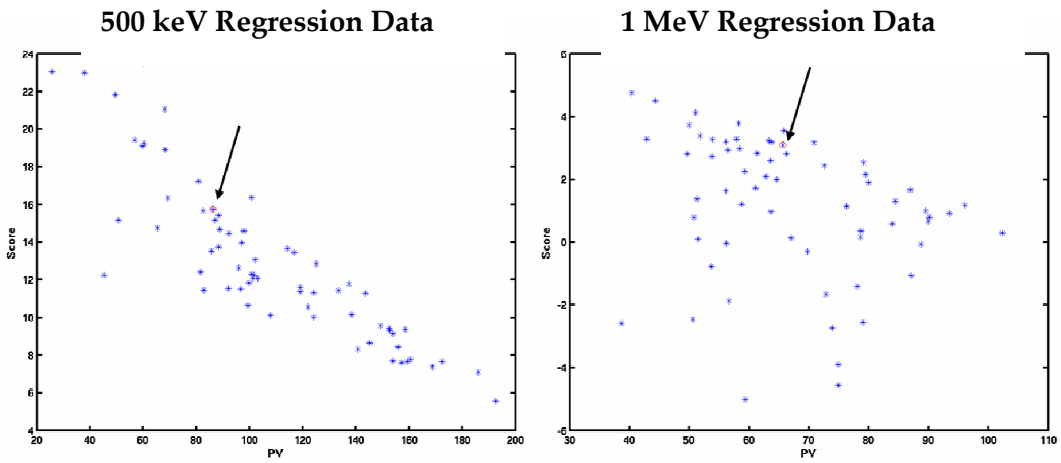

Figure 25. Predicted image quality score vs. efficiency for 25 or 30 mm slat height RMCs. Left: 500 keV data. Right: 1 MeV data. The arrow points to the point from the chosen design.

5.6 Summary

An RMC design was chosen by systematically testing each of the individual RMC parameters. In testing two collimators versus one, it was found that at low energies one collimator is preferable, but in the energy range of interest (500 – 1000 keV) two collimators provide a more distinct modulation profile. This is because the first collimator initially thins the incident gamma rays before they are able to reach the second.

A second collimator is necessary, but the distance between the two does not matter if that separation is between 5 and 20 cm. A separation of 5 cm was chosen to allow for the camera to be placed closer to the object of interest. Additionally, the slats can be aligned or offset. This is most likely due to the high-energy gamma rays. Septal

penetration blurs the slight difference in acceptance angle between aligned and unaligned slats. An offset alignment was chosen as this seems more easily achievable goal in manufacture then perfect alignment.

Several different low-melting point lead alloys were tested as the slat material. All except for one had a lower equivalent Z and all were less dense. As both Z and density affect stopping power, tests confirmed that lead was the most effective collimator material. This is acceptable as new slats will not have to be made on a regular basis, eliminating the need for using the easily moldable alloys. Lead is the collimator material of choice.

Finally, slat height, slat width and slot width were determined. Using a regression analysis between modulation profile shape and predicted image quality score it was apparent there is a trade off between image quality and detector efficiency. This is the same tradeoff conventional gamma cameras face. Further data analysis identified a set of parameters that provide reasonable image quality and efficiency for both 500 keV and 1 MeV gamma rays.

In the next chapter the chosen RMC design will be used to reconstruct images for both a small animal FOV (10 cm x 10 cm) and a human FOV (25 cm x 25 cm).

6. Imaging Limits of Near-Field RMC Camera

Preliminary image reconstructions indicated that planar images could not be reconstructed without first performing a systematic study to determine the imaging limits on the RMC system. This chapter investigates the optimal FOV for imaging, addresses the limits of the imaging system and finally provides reconstructed line images generated from Monte Carlo simulation data. The quality of the reconstructed images is assessed based on three figures of merit: (i) signal-to-noise ratio (SNR), (ii) the FWHM of the reconstructed line, and (iii) a measure of the linearity of the imaged line source.

As mentioned in Chapter 2, reconstruction with the MLEM algorithm allows the user to choose the number of pixels in the reconstructed image without regard for the amount of information in the system. However, an under sampled system is a concern for image quality. Herein, two different image sizes were chosen, 10 x 10 pixels and 25 x 25 pixels. To test the resolution limits, pixel size was decreased while keeping the number of pixels the same. This removed the sampling rate variable from the problem. The amount of information in the system remained the same, and only the reconstructed pixel size changed. In a typical FOV approach, the FOV remains the same, and the number of pixels increases as the pixel size decreases. Given that the limits on the

system depend on the amount of unique information available for reconstruction, keeping the number of pixels constant was deemed the best approach.

6.1 Field of View for Small Animal Imaging (10 x 10 pixels)

6.1.1 Visual Inspection

To provide a rough estimate of image quality, point source images were reconstructed using the near-field model to provide observation profiles and probability matrices. The near-field model is used instead of a GEANT4 simulation for two reasons: (i) only a rough image approximation is necessary (there is no need to simulate septal penetration), and (ii) improved time and efficiency (the near-field model generates the probability matrix, observation matrix and reconstructed image in seconds, whereas GEANT4 generates a probability matrix in hours). Point sources were reconstructed in a 10 pixel by 10 pixel FOV at various pixel sizes and FOV positions in order to determine where the FOV should be located in space for each pixel size. The RMC permutations listed in Table 12 were explored.

Table 12. RMC configurations for testing 10 x 10 FOV.

Parameter	*Value*
Collimator angles	0° to 180° in 1° increments
Pixel size	0.5 cm to 1.5 cm in 0.25 cm increments
Center of FOV (radial location from z-axis)	2 cm to 24 cm in 2 cm increments
SID	19 cm
Separation	5 cm
Slat Height	2 cm and 3 cm
Slot Width	0.1 to 0.4 cm in .05 cm increments
Slat Width	n/a for model

The reconstructed point source images for each radial FOV location were visually inspected. As the slat height increased and the slot width decreased, the image quality improved across all radial FOV locations and different pixel sizes. For each pixel size, a different radial location of the FOV provided the best image quality. Additionally, as pixel size decreased, image quality decreased, regardless of FOV location. As demonstrated in Figure 26, there appears to be a limit to the system's ability to reconstruct images. Further analysis of the probability matrix revealed the causes of this limit, which is discussed in the next section.

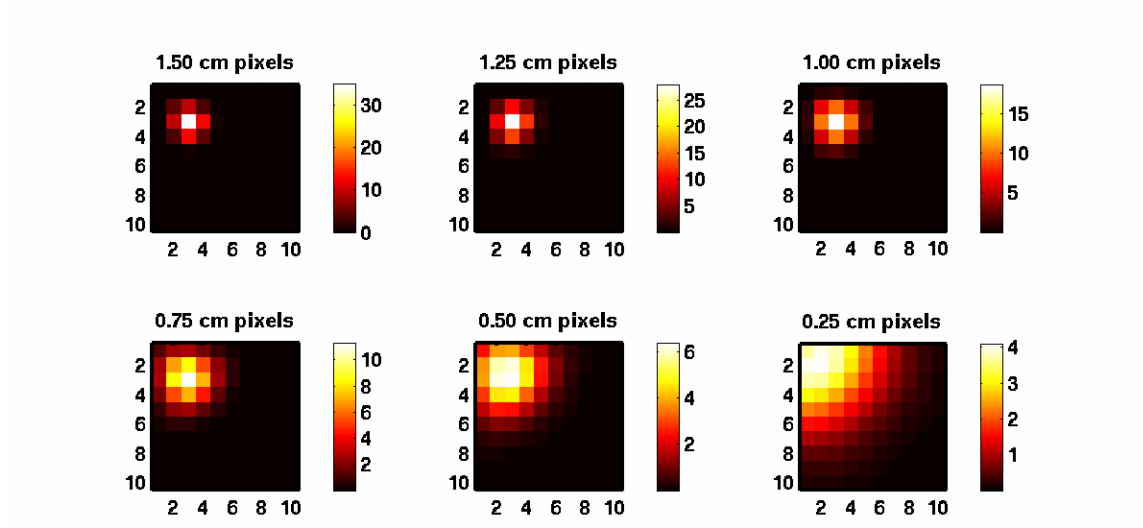

Figure 26. Point source reconstructions for a 10 x 10 pixel four camera system at the optimal radius for each pixel size. Note how the image quality decreases with pixel size.

6.1.2 Data Analysis

The optimal location of the FOV is related to the uniqueness of the probability matrix. Generally, as the uniqueness of the matrix increases, the MLEM algorithm better identifies the pixels the observed signal originated from. The probability matrix from each radial FOV was examined in detail for the specific case of 0.1 cm slot width and 3.0 cm slat height (see Table 12 above). As the trend of improved image quality for increasing slat heights and decreasing slot widths was seen at all radial locations and pixel sizes, it was unnecessary to examine more then one probability matrix from each radial location and pixel size. This specific case was chosen as it produced the best overall images. Four parameters of the probability matrix were measured. The first parameter, *delta max*, is the difference between the peak height of the maximum valued

modulation profile and the peak height of the minimum valued modulation profile. A high *delta max* implies a more unique matrix. The second parameter, *correlation all*, is defined as follows. Each modulation profile is correlated against all other modulation profiles in the probability matrix. For each profile, the number of profiles significantly correlated with a two-tailed p-value of < 0.05 is recorded. The average number of correlated profiles for each profile within the probability matrix is defined as *correlation all.* A high *correlation all* implies a less unique matrix. The third parameter, *correlation close*, measures the number of correlated profiles that have peaks within 45° of one another. Finally the fourth parameter, *percent overlap*, measures the number of pixels that overlap from one FOV to another when using multiple camera views. The lower the *percent overlap* is, the more unique the information in the system is. Figure 27 below depicts the four measured parameters based on the radial location of FOV and the reconstructed pixel size.

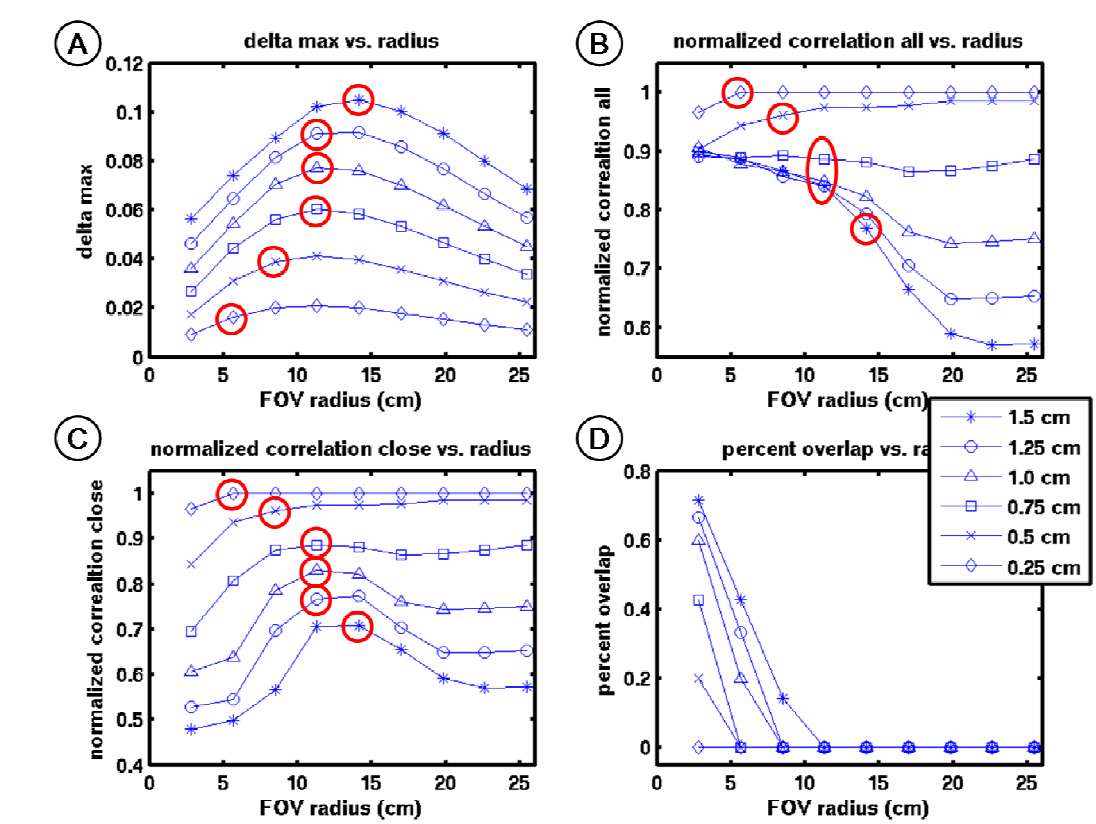

Figure 27. Probability matrix parameters for a 10 by 10 pixel FOV using 4 cameras (A) delta max (B) correlation all (C) correlation max (D) percent overlap. The circled points indicate the radius at which best visual image quality occurred.

Several trends are notable in Figure 27.

1. The radius where best image quality occurred is at or one data point away from the radius of the maximum *delta max* point for each pixel size.
2. *Delta max* increases with increasing pixel size.
3. All radii of best visual quality occur when the *percent overlap* is 0%.
4. Both *correlation close* and *correlation all* decrease with increasing pixel size.

5. Close inspection of plots B and C show that the *correlation all* and *correlation close* values intersect once the radius is sufficiently far away from the axis of rotation.

Trends 4 and 5 are consistent with the geometry of the system. As the FOV moves farther away from the axis of rotation, the polar angle between pixels decreases. This effect is compounded by smaller pixel size. For example, a point at (2,2) is located at a polar angle of 45°. For a 1 cm pixel size the nearest neighbor at (2,3) has a polar angle of 56.3°, while a 0.5 cm pixel neighbor at (2,2.5) has a polar angle of 51.34°. As the radius increases, this effect increases. A pixel at (9,9) has a polar angle of 45°; its 1 cm pixel neighbor (9,10) has a polar angle of 48.0°, while the 0.5 cm pixel neighbor (9,9.5) has a polar angle of 46.5°. The radius of intersection between *correlation close* and *correlation all* is at the radius of best visual quality for pixel sizes 0.75, 0.5 and 0.25, while it is one after the radius of best visual quality for pixel sizes 1.5, 1.25 and 1.0.

All four parameters have an effect on the uniqueness of the system; therefore, they affect the reconstruction quality. Results showed that as the *delta max* increased, image quality increased. Conversely, as the correlation between matrix elements increased, image quality decreased. Based on the above noted observations, the system must be within the following boundaries to allow acceptable reconstruction for small animal imaging:

1) The FOV must fall at a radius were the maximum *delta max* occurs.

2) This radius of maximum *delta max* must also occur before the *correlation close* merges with *correlation all*.

6.1.3 Effect of additional cameras on reconstruction quality

The four cameras in the above system were centered in each Cartesian quadrant (Figure 28). This experimental setup led to symmetry of the system on either side of the 45° line (Figure 29). If eight cameras were used, centered at 22.5° and 67.5° in each quadrant, each camera's FOV would overlap its neighbor more than in the four-camera system. However, the individual probability matrices would not be symmetric (Figure 28 and Figure 29).

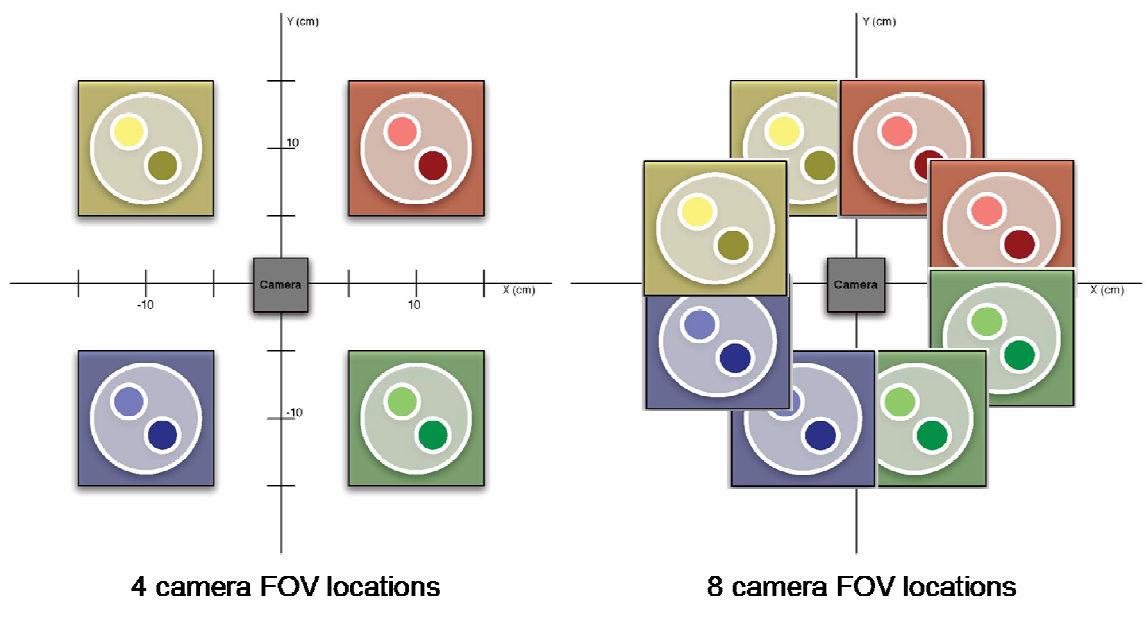

Figure 28. FOV locations for 4 camera views (left) and 8 camera views (right)

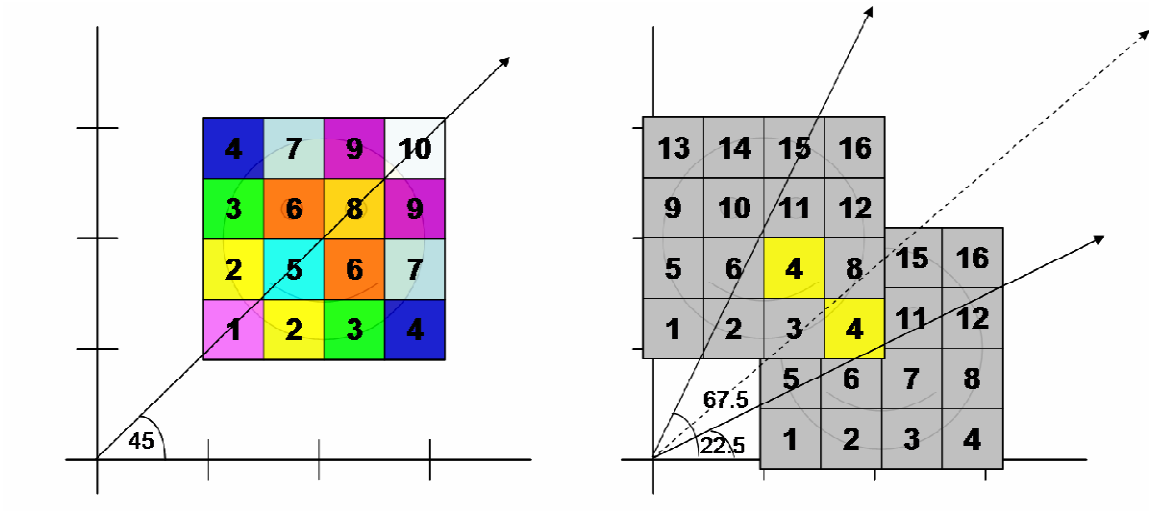

Figure 29. FOV modulation profile symmetry for 4 camera FOV (left) and 8 camera FOV system (right). The 4 camera FOV lies on the 45 degree line, creating symmetry (pixels 2, 3, 4, 6, 7, 9), while the 8 camera FOV is off centered, and in this case only pixel 4 crosses the plane of symmetry.

Figure 30 shows a schematic representation of a FOV from both the four and eight-camera systems. The two systems should have similar *delta max* values as the FOV is within the same radial distance away from the axis of rotation resulting in similar extreme values. As demonstrated in Chapter 3 (Figure 13), two things affect modulation profile shape. *Radius* affects the modulation profile height and shape, while *angle* affects the peak location. As shown in Figure 30, more pixels from the eight-camera system exist along the same radial line. In general, these pixels cover a larger angular spread as compared to the four-camera system; therefore, this geometry indicates that *correlation all* will remain about the same because the radii will be similar between pixels. However, *correlation close* will decrease in the eight-camera system as compared to the

four-camera system because the angular location of different pixels will be less similar. Adding twice the amount of information into the system from an additional four cameras and reducing *correlation close* has the possibility enhance image reconstruction quality over the four-camera system.

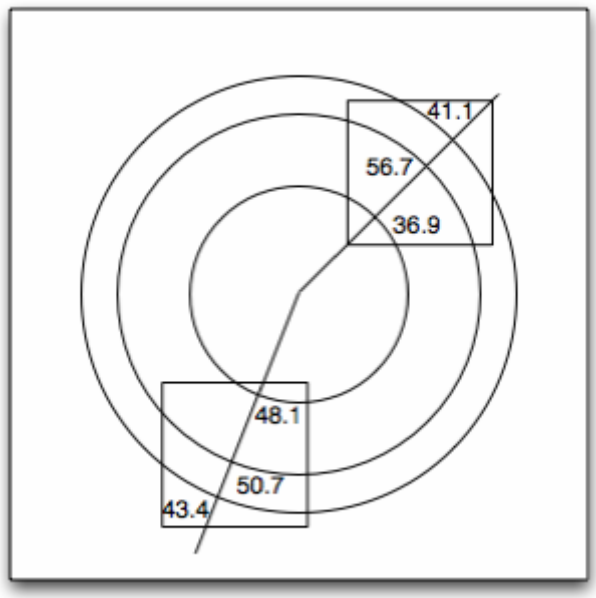

Figure 30. A FOV from the 4-camera (top) and 8-camera (bottom) system. The angular spread between the two outside pixels is listed. Note how the radial lines cover more pixels inside the 8 camera FOV, but that the angular spread is on average larger.

To test the effect on image quality, point source images were reconstructed as in section 6.1.1, except that eight-camera views were used. The center of the FOVs were located the same radii away as before, but now centered at 22.5° and 67.5° in each quadrant. Visual inspection of the results yielded a new optimal radial location for each

pixel size. Image quality was affected based on FOV radius and RMC setup as before (Figure 31).

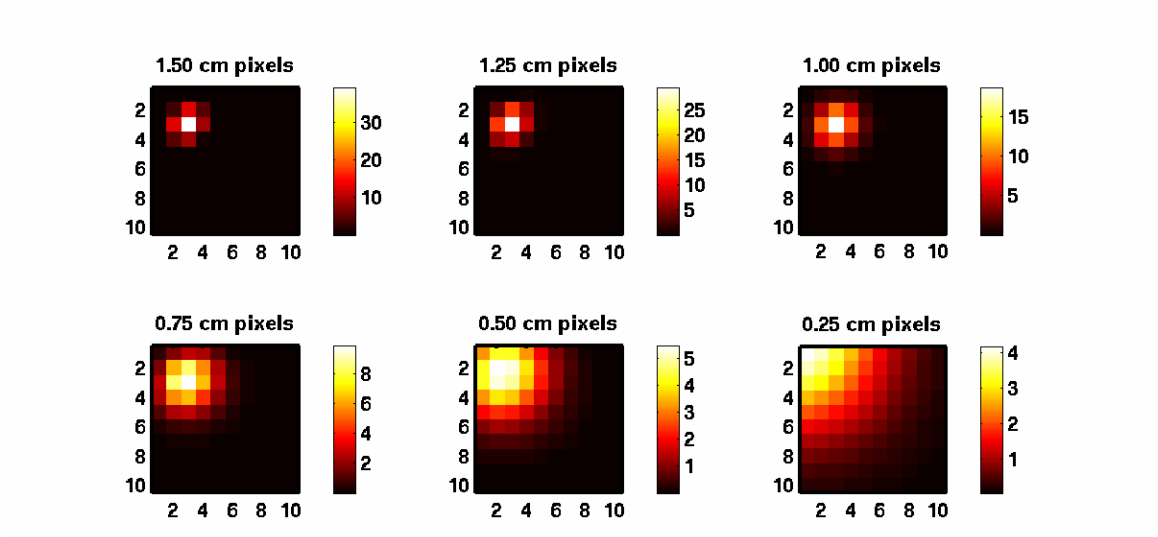

Figure 31. Point source reconstructions for a 10 x 10 pixel eight camera system at the optimal radius for each pixel size. Note how the image quality decreases with pixel size.

Visual inspection shows that, compared to the four-camera system, the 1.5 cm and 1.25 cm pixel images are improved, while the rest remained about the same. To determine the cause, the properties of the probability matrices were measured for each camera view and then averaged together as in section 6.1.2. Figure 32 shows the probability matrix parameters for both the four and eight-camera systems at the 1.25, 1.0 and 0.75 cm pixel sizes. As expected, the d*elta max* values remained about the same. In the 1.5 and 1.25 cm pixel data, there was a significant drop in *correlation close*. Additionally, *correlation all* merged with the *correlation close* value several radii after the ideal FOV location. This observation explains the marked improvement for the 1.5 and

1.25 cm images. However, as the pixel size decreases so does the change in *correlation close*. This small drop in *correlation close* from the four to the eight-camera system was not enough to improve the quality of images comprised of smaller pixel sizes. Not enough unique information was added to the system to increase image quality.

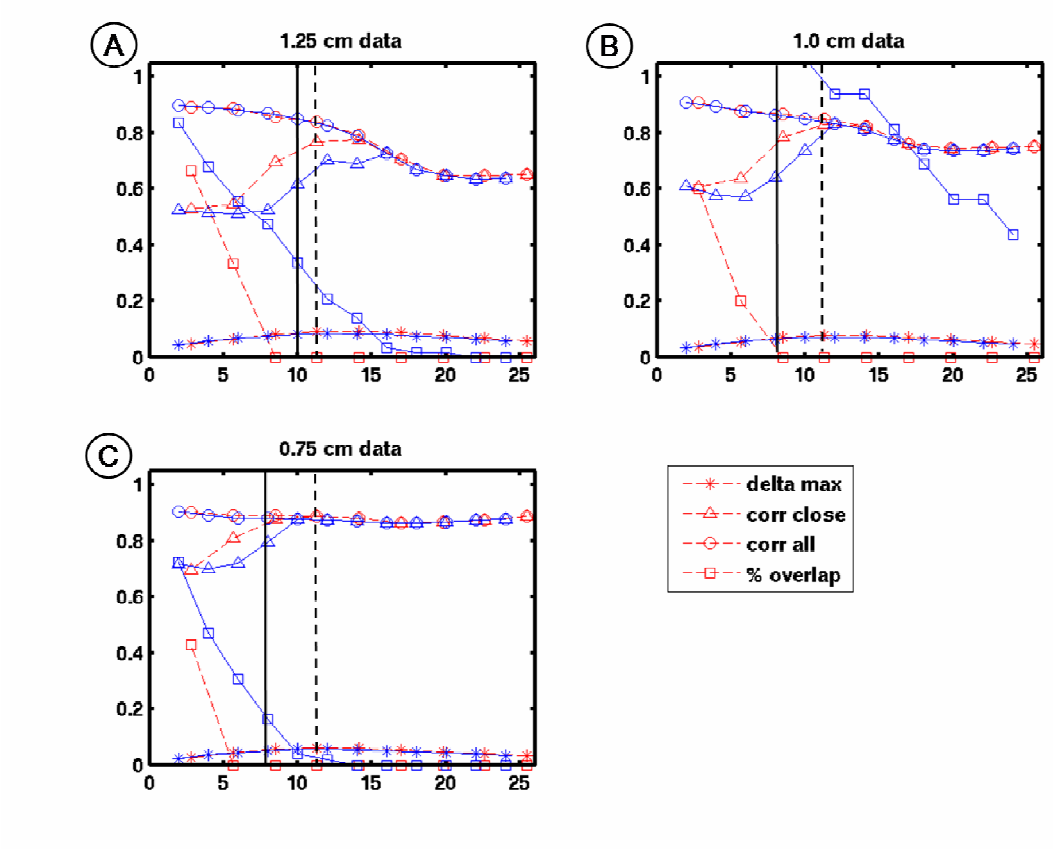

Figure 32. Probability matrix parameters for 1.25 cm pixels (A), 1.0 cm pixels (B) and 0.75 cm pixels (C) for both the 8 camera (solid lines) and 4 camera (dashed lines) systems. The vertical lines indicate the optimum FOV radius for each system.

6.2 Field of View for Imaging Humans (25 x 25 pixels)

The system was also explored for a 25 x 25 pixel FOV – large enough to view a region of interest in a human. Again, point source images were reconstructed as in section 6.1.1, except that eight camera views were used as in section 6.1.3 and the FOV was increased to 25 x 25 pixels. A four-camera system was also evaluated; however, preliminary results demonstrated that this system was unable to reconstruct acceptable images. Visual inspection identified a FOV radial center of choice and showed diminishing image quality as the pixel size decreased (Figure 33).

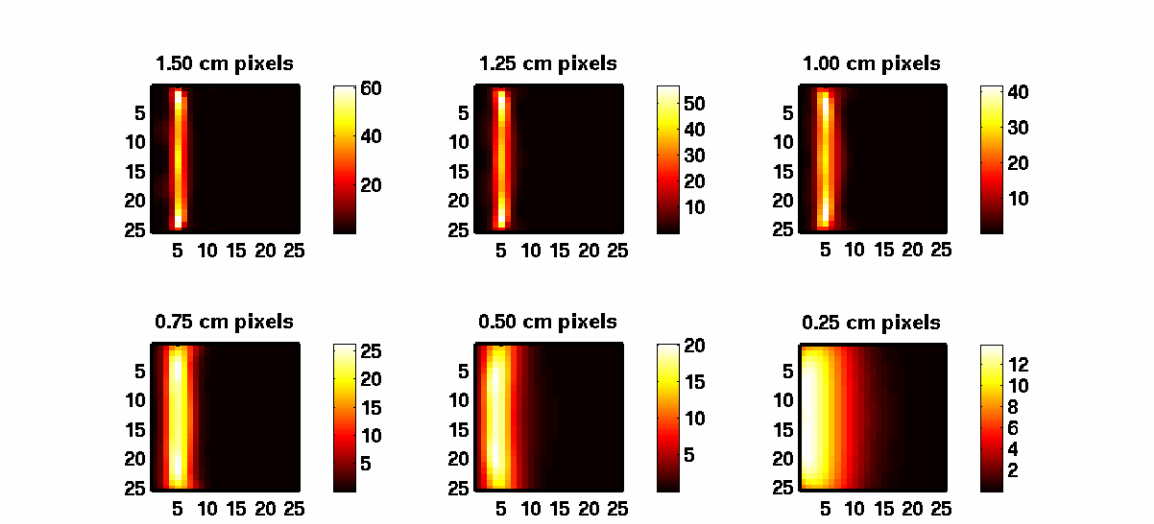

Figure 33. Line source reconstructions for a 25 x 25 pixel eight camera system at the optimal radius for each pixel size. Note how the image quality decreases with pixel size.

As in section 6.1.2, the probability matrix properties were measured. Due to the increase in the FOV, *delta max* was expected to be higher and the *correlation close* and *correlation all* measures were expected to be less then the 10 x 10 pixel systems. More

pixels covering a larger region should have less in common with one another. Finally, *percent overlap,* was expected to increase as the large FOVs would overlap more of one another. Figure 34 shows the plots of the properties.

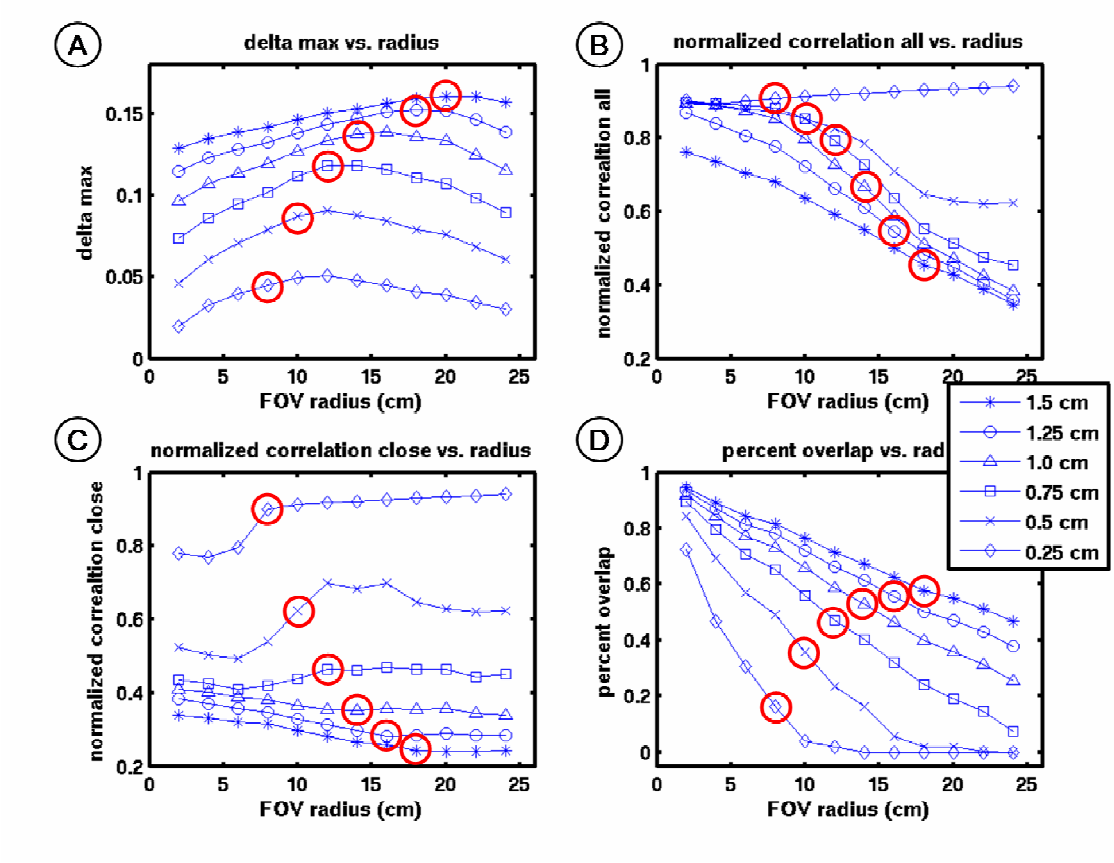

Figure 34. Probability matrix parameters for a 25 x 25 pixel FOV using 8 cameras (A) delta max (B) correlation all (C) correlation max (D) percent overlap. The circled points indicate the radius at which best visual image quality occurred.

As expected for the 25 x 25 pixel system, *delta max* is higher, *correlation max* and *correlation close* are lower and *percent overlap* is higher than in the 10 x 10 pixel system. The 25 x 25 pixel system provides more unique probability matrices, as *correlation close* and *correlation all* do not intersect for any pixels larger then 0.5 cm. Although *percent*

overlap is significantly raised, this does not seem to have much of an adverse effect on image quality. The modulation profiles from individual pixels provide different information relative to their encompassing FOV. This indicates that despite pixels overlapping between FOVs, each FOV provides unique information to the system. However, due to the overlap, increasing the number of FOVs does not linearly increase the unique information in the system. Overall, image quality was acceptable for the 1.5 cm to 0.75 cm pixel sizes. This finding is also supported by the improved probability matrix properties for the 25 x 25 pixel system as opposed to the 10 x 10 pixel system.

6.3 Reconstructed Image Quality Metrics

Once the effect of both probability matrix composition and FOV placement on image quality had been determined, images were reconstructed. To measure the reconstruction quality of images, a large Monte Carlo simulation was performed, obtaining a modulation profile for point sources every 0.5 cm over a vast FOV using the optimal RMC parameters chosen in chapter 5. The Monte Carlo simulation parameters are listed below in Table 13.

Table 13. Monte Carlo parameters to test image quality.

Parameter	*Value*
Collimator angles	0° to 180° in 3° increments
Gamma events at each angle	10,000
Point source strength	500 keV
SID	19 cm
Separation	5 cm
Slat Height	3 cm
Slat Width	3 mm
Slot Width	3.5 mm

This large data set was used to create smaller probability matrix data sets for the 10 x 10 four-camera, 10 x 10 eight-camera, and 25 x 25 eight-camera configurations at 0.5 cm, 1.0 cm and 1.5 cm pixel sizes. The locations of the FOVs were placed at the optimal positions identified above. Three types of reconstructions were performed for each camera / FOV configuration.

1. M*ath*, a reconstruction using the geometric model (this is the best case with no blur, counting fluctuations or septal penetration).
2. *Exact*, where the probability matrix was formed with the point source located exactly in the center of the pixel and observation matrices were created from the probability matrix. This reconstruction tested the effect of septal penetration but not blur or counting fluctuations.
3. *Random*, where the probability matrix was formed by averaging the modulation profiles from the center of the pixel and its eight closest

neighbors located 0.5 cm away in the x or y direction. The observation profiles were then formed by randomly choosing one of the 9 component modulation profiles. This accounted for septal penetration, counting fluctuations and blur.

It was expected that the *math* reconstructions would perform the best followed by the *exact* and finally *random*, because at each step more uncertainty and noise are added into the system.

For each camera configuration a line was reconstructed at every horizontal and vertical position within the image. This method resulted in 20 reconstructed images for the 10 x 10 FOV and 50 for the 25 x 25. For each line three image quality metrics were calculated. The first metric, *SNR*, is defined as the maximum value on the line divided by the mean background of the image. *SNR* is expected to increase with increasing image quality. The second metric, *FWHM*, is the FWHM of the line spread of pixels perpendicular to the line at each pixel of the line. A thin line will have a low *FWHM*. The third metric, *linearity*, is the root mean square of the difference between the pixel location of the maximum value to the expected location of the maximum value. A low *linearity* value indicates a straight line.

6.3.1 10 x 10 Image Reconstructions

Figure 35 depicts the reconstructions for the 10 x 10 FOV for a vertical line in the center of the image and a horizontal line one row from the top of the image. Visual inspection shows that as the pixel size grows the line becomes thinner and more distinct. Additionally, the image quality decreases as the system becomes more unknown and variable, with the *math* reconstruction performing the best and the *random* performing the worst. Of note, there is inconsistency in reconstruction performance between the different images. For example, the vertical line reconstruction is located in the same spot as the true image, however the horizontal line is located at the top line and its true image is one line below the top. The eight-camera system seems to outperform the four-camera system for the 1.5 cm pixels, while the four-camera system performs better for the 0.5 cm pixels. Both systems perform about the same on the 1.0 cm pixels.

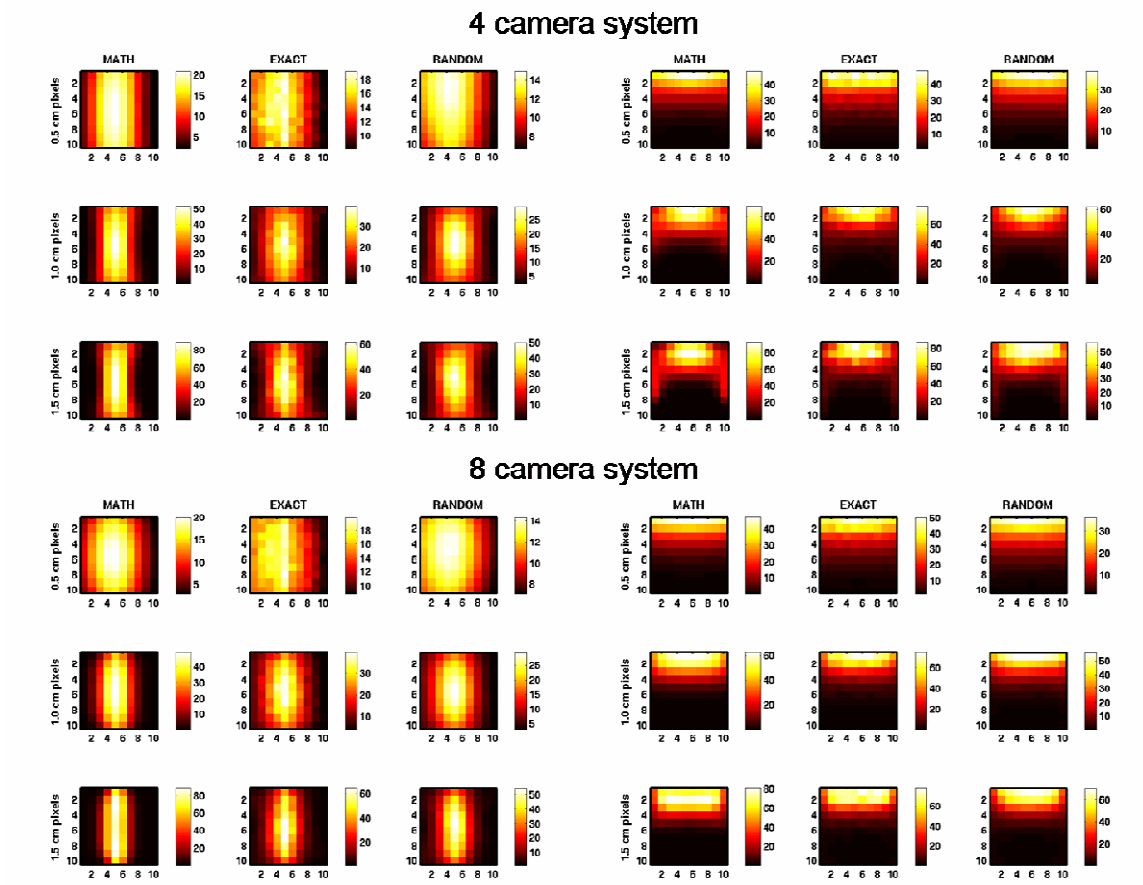

Figure 35. Images of a horizontal line (left) and vertical line (right) in a 10 x 10 FOV. On the top is the four camera system, and on the bottom is the eight. In each group of nine the rows are 0.5 cm, 1.0 cm and 1.5 cm pixels and the columns are the math, exact and random reconstructions.

Figure 36 shows the image quality measurements for the 10 x 10 images. The left column is the mean of all 20 images, while the right column is for just the vertical lines from Figure 35. The four-camera and eight-camera data are listed next to one another for each pixel size. As pixel size increases, the *SNR* measure increases while the *FWHM* and *linearity* measures decrease indicating improved image quality. Careful inspection of the

numbers confirms both visual evidence and the conclusions reached in section 6.1.3. Namely, the eight-camera system out performs the four-camera at larger pixel sizes, there is no apparent difference at middle pixel sizes, and the four-camera system is better at low pixel sizes.

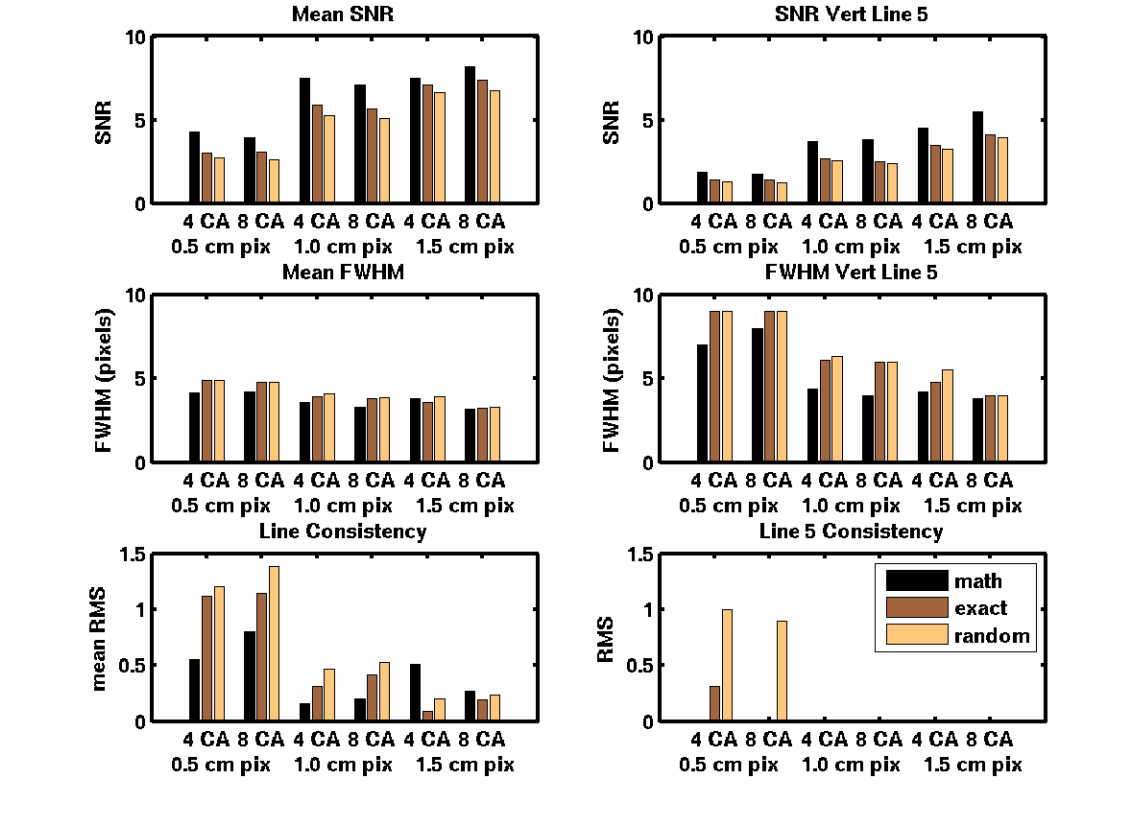

Figure 36. Image quality measurements comparing the different 10 x 10 image systems. The left column shows the mean of the measurements for all 20 reconstructions, while the right shows the measurements for the vertical line.

6.3.2 25 x 25 Image Reconstructions

Figure 37 shows the reconstructed image of a vertical and horizontal line in the 25 x 25 pixel FOV. As with the 10 x 10 pixel systems, image quality improves as pixel

size increases and image quality degrades as the system becomes more variable. However, image reconstruction quality varied with the location of the line source. Reconstructed images of lines located in the center of the image were well-defined and straight; whereas, images of lines located near the edges were ill-defined and curved. Additionally, artifacts begin to appear in the 1.0 cm pixel images and become very apparent in the 1.5 cm pixel images.

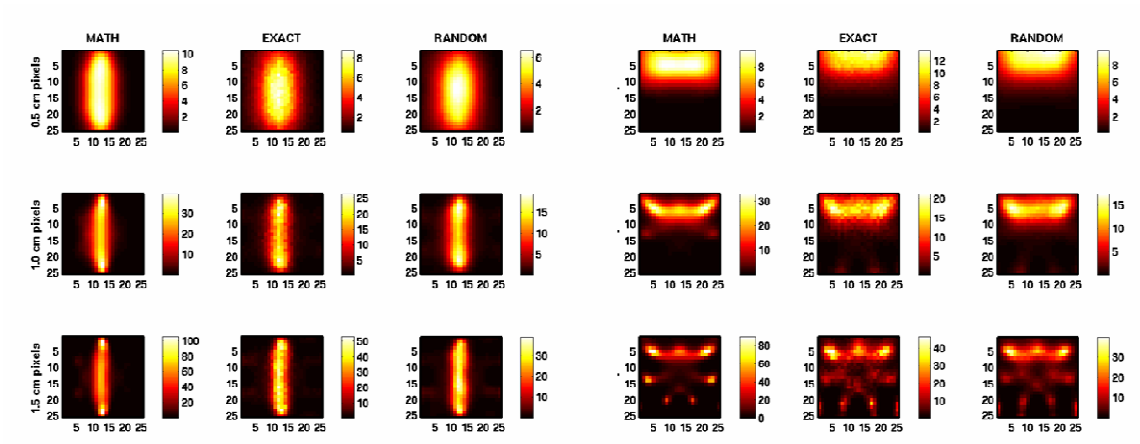

Figure 37. Images of a vertical (right) and horizontal (left) line in a 25 x 25 pixel FOV. The rows delimit 0.5 cm, 1.0 cm and 1.5 cm pixels (top to bottom) while across is the math, exact and random reconstruction methods.

Figure 38 depicts the image quality measurements for the 25 x 25 FOV. The left column depicts averages across all 50 images, while the right column shows the measurements for the vertical line depicted in Figure 37. For the average of the 50 images, the *SNR* improves from the 0.5 to 1.0 cm pixel images, and remains about the same for the 1.5 cm pixel images. For each pixel size, the *SNR* decreases as system variability increases. Very little difference is noted with respect to *FWHM* while *linearity*

has a sharp increase from 1.0 to 1.5 cm pixels. This is due to the appearance of artifacts. Measurements for a line at the center of the image show an improvement in *SNR* and *FWHM* as compared to the average across all images. These increased image quality metrics are indicative of the trend that reconstruction quality of lines in the center of the image is superior to that of lines toward the edge.

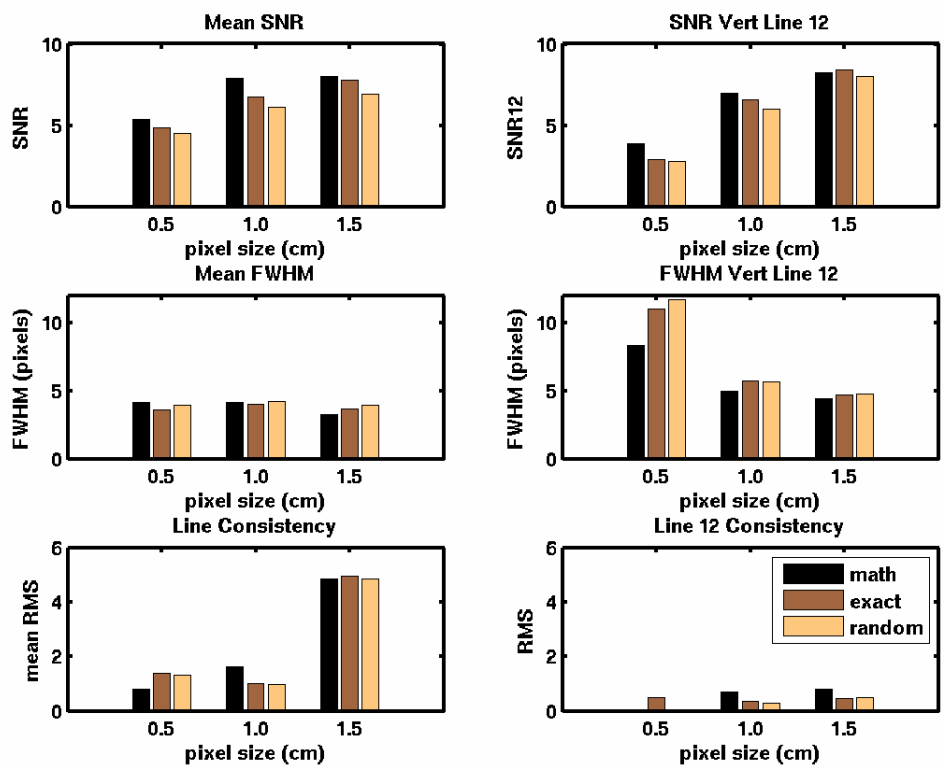

Figure 38. Image quality measurements comparing the different 25 x 25 image systems. The left column shows the mean of the measurements for all 20 reconstructions, while the right shows the measurements for the vertical line.

6.4 Summary

There is a fundamental limit on the reconstruction ability of the RMC camera system. This limit is dependant on the uniqueness of the probability matrices needed to

reconstruct the FOV. A more unique probability matrix will result in better image quality. This is apparent as image quality improves from the 0.25 pixel size up to the 1.5 cm pixel size.

The number of cameras needed to reconstruct a 10 x 10 pixel FOV varies depending on pixel size, and larger pixels benefit from a greater number of cameras. With the larger pixel size, more unique information is captured in each FOV when using eight cameras. As the pixel size reduces, there is less unique information and adding four more cameras to the system does not improve reconstruction quality.

For the 25 x 25 pixel FOV system, many 1.0 cm pixel images achieved reasonable reconstruction quality; however, artifacts are noticeable in several of the reconstructed images.

Regardless of the number of cameras or pixels, images comprised of pixels less than 1 cm in size have poor resolution. Therefore, use of this camera for small animal imaging is not feasible. 1.0 cm pixels reconstructed consistently for both the 10 x 10 and 25 x 25 pixel FOVs. It appears that 1.0 cm pixels may be acceptable for gross human imaging.

Despite some favorable results, the overall results suggest that while some images may reconstruct well, the system is not sufficiently robust for use in NSECT imaging of humans or small animals due to chronic under-sampling. As explained in

Chapter 2, MLEM allows reconstruction of under-sampled systems; in this case, the under-sampling is too severe.

It is difficult to determine the exact sampling of this camera system. Chapter 3 discussed that increasing the collimator angles from 180 to 625 had no impact on image quality. The conclusion reached was that adding more interrogation angles did not increase the amount of unique information in the system. However, it would be wrong to assume that the modulation profile only counts as one piece of information. An acceptable estimate is to divide 180° (full camera rotation) by the average FWHM of the profiles in the probability matrix and multiply that number by two to determine the optimal angular sampling rate. Additionally, it is known that increasing the number of camera views does aid image reconstruction, so this must add to the amount of unique information in the system. Multiplying the angular sampling rate by the number of cameras provides a rough estimate of the sampling of the system.

For the four-camera 10 x 10 system, the average FWHM was 30°, providing a sampling measure of 48. This number is well below the 100 pixels that were reconstructed. For the eight-camera 10 x 10 system, the average FWHM was also 30°. This system has a sampling measure of 96, which is close to the 100 pixels. Finally, the eight-camera 25 x 25 system has an average FWHM of 14°, which provides a sampling measure of 224, well below 625 pixels. This constant under-sampling in all systems could account for the inconsistencies in reconstruction. While some images are in a

location that allows reasonable image reconstruction, some are not. Adding more cameras to the system would add more information, but not in a linear fashion. Each new camera FOV does not add completely different information, as FOVs overlap and modulation profiles within the FOVs are similar to one another. This camera system is unable to reach an adequate sampling rate; therefore, image reconstruction ability is not robust enough for the proposed NSECT use.

7. Summary, Conclusion and Future Work

NSECT is a promising interrogation imaging method with the potential to identify and map elemental concentrations within the body. This modality has potential applications for both identifying cancerous regions and monitoring patients with various liver diseases.

Current position sensitive gamma cameras do not operate in the energy range of interest. This thesis focused on exploring a space-based gamma imaging technique in order to develop near-field, high-energy, position-sensitive gamma camera for use with NSECT.

7.1 Summary

Chapter 3 explained the concept of using a RMC coupled with a solid-state HPGe detector. The detector provides superior energy resolution while the RMC provides spatial information through gamma ray modulation. To understand the behavior in the near-field, a prototype camera was constructed and tests showed a behavior different from that expected in the far-field. A new geometric model was developed to explain the gamma ray modulation in the near-field. This model explains general modulation behavior but does not account for septal penetration.

Chapter 4 discussed the development of a Monte Carlo simulation environment to explore aspects of the RMC design. Results from the simulation matched experimental data collected with the prototype camera. Unlike the geometric model from Chapter 3, this environment simulated all aspects of the camera and gamma ray interactions. A Monte Carlo simulation is necessary to speed camera development as it is time and cost prohibitive to determine a camera design using the prototype camera.

Chapter 5 described the systematic testing and identification of optimal RMC parameters. Six parameters were tested. First, slats comprised of lead outperformed slats comprised of low-melting-point alloys. Second, the differences between various collimator separation and slat offset configurations were found to be minimal. A separation of 5 cm was chosen to allow for increased efficiency and offset slats were chosen to mimic construction imperfections. Finally, slat height, slat width and slot width were tested together by fitting a regression to various modulation profile properties. As with other gamma cameras, there is an inverse relationship between camera efficiency and image quality. Based on the above findings, a design was chosen that was a reasonable compromise between efficiency and image quality.

Chapter 6 determined the fundamental limits on the imaging system by analyzing the uniqueness of modulation profiles that comprise a probability matrix. This uniqueness is affected by the location of the FOV and the size of the pixels. Reconstructions were performed on data obtained from a Monte Carlo simulation.

While some acceptable imaging configurations existed, the system's behavior was inconsistent for both small animal and human fields of view.

7.2 Conclusion

The functionality of the RMC in the near-field was explored, analyzed and fully explained. The effect of various RMC parameters on gamma modulation was determined. Despite the identification of optimal RMC and image plane parameters, the quality of the reconstructed images does not currently support the application of NSECT for either small animal or human imaging. This inconsistency is due to the severe under-sampling of the system. While MLEM can account for under-sampling, there is just not enough unique information in the system to ensure reasonable image reconstruction for near-field NSECT imaging.

7.3 Future Work

While camera functionality is too uncertain in the near-field for use with NSECT, it may be acceptable in the mid-field. NSECT has potential to be applied to monitoring of cargo containers for homeland security. In order to scan a large object (several meters across), the camera would have to be located at least several meters away. This increased SID would narrow the modulation profiles significantly. Thinner modulation profiles result in an increased angular sampling rate, adding more information to the system.

Increased information has the possibility to provide a correctly sampled system and more accurate image reconstructions.

This hypothetical scenario was tested in a Monte Carlo simulation with the following parameters. The HPGe detector was expanded to a radius of 35 cm to simulate the bank of HPGe detectors needed for this sort of operation. The parameters listed in Table 14 were used in the simulation:

Table 14. Monte Carlo simulation of hypothetical Homeland Security application.

Parameter	*Value*
Collimator angles	0° to 180° in 3° increments
Gamma Ray Energy	500 keV
Gamma Ray Events	20,000 per angle
Pixel Size	40 cm
Pixel Number	25 x 25
FOV Radial Center	10 m
SID	10 m
Separation	0.5 m
Slat Height	5 cm
Slat Width	0.3 cm
Slot Width	0.35 cm

Figure 39 depicts four different reconstructed images obtained from the above simulated data. These are indeed acceptable image reconstructions. At this mid-range distance, the average FWHM is 3°, resulting in an approximate sampling measure of 960 for an eight-camera system. This measure is 50% greater than the 625 pixels in the reconstructed image. Although these results are highly preliminary and a rigorous study

is necessary to establish feasibility, the knowledge gained in this thesis supports the hypothesis that mid-field NSECT interrogation may provide the correct amount of unique information needed to reconstruct images.

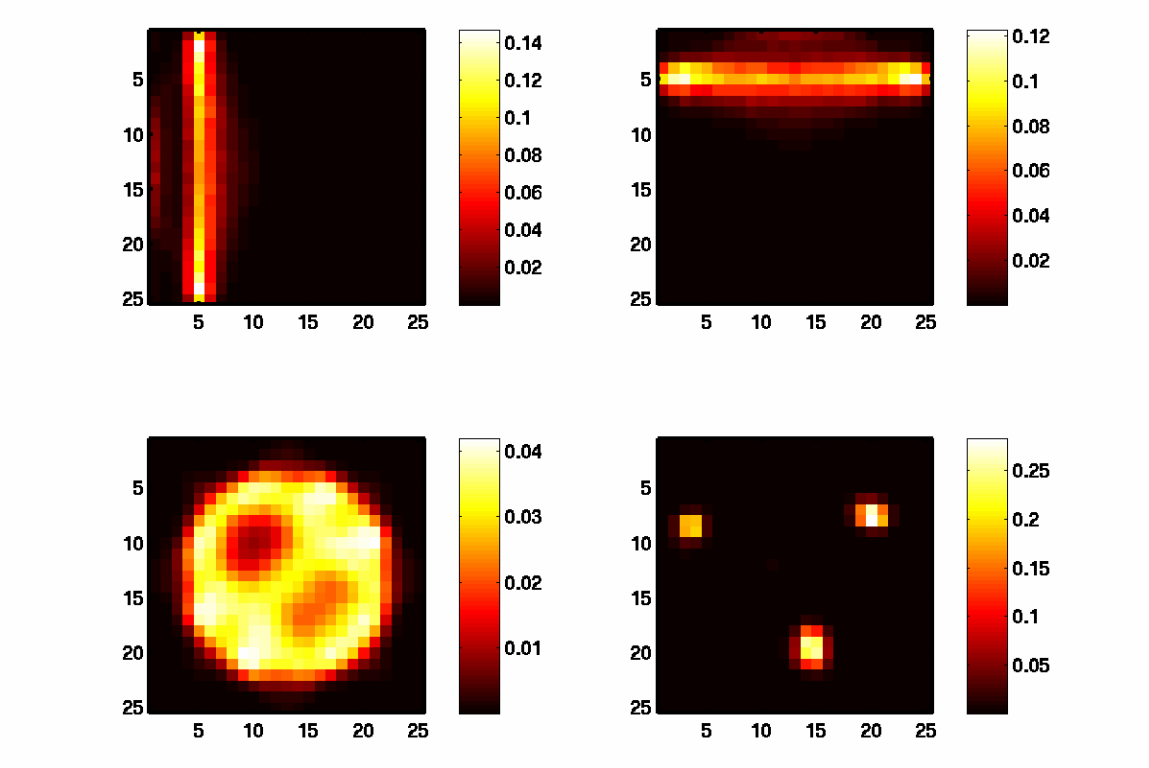

Figure 39. Four reconstructed images obtained from mid-field simulated data.

While NSECT imaging of humans is not possible using this camera system, other possibilities exist to obtain images. Currently, the first-generation CT technique is being used, and is a valid, yet time-consuming, option [44]. Additionally, as detector and crystal technologies improve, it may still be possible to design a position-sensitive gamma camera for use in the near-field at high gamma energies.

References

1. Andrasi, E., Suhajda, M., Saray, I., Bezur, L., Ernyei, L., Reffy, A. , *Concentration of elements in human brain: glioblastoma multiforme.* Sci. Total Env., 1993. **139/140**: p. 399-402.

2. Katoh, Y., Sato, T., Yamamoto, Y., *Use of instrumental neutron activation analysis to determine concentrations of multiple trace elements in human organs.* Arch. Env. Health, 2003. **58**(10): p. 655-661.

3. Milman, N., Laursen, J., Podenphant, J., Staun-Olsen, P. , *Iron, copper, zinc, and selenium in lumen liver tissue measured by X-ray fluorescence spectrometry.* Scand. J. Clin. Lab. Invest., 1983. **43**: p. 691-697.

4. Persigehl, M., Schicha, H., Kasperek, K., Klein, H.J., *Trace element concentration in human organs in dependence of age.* Beitr. Path., 1977. **161**: p. 209-220.

5. Stedman, J.D., Spyrou, N.M., *Major and trace element concentration differences between right and left hemispheres of the 'normal' human brain.* Nutrition, 1995. **11**(5): p. 542-545.

6. Yoshinaga, J., Imai, H., Nakazawa, M., Suzuki, T., *Lack of significantly positive correlations between elemental concentrations in hair and organs.* Sci. Total Env., 1990. **99**: p. 125-135.

7. Yukawa, M., Suzuki-Yasumoto, M., Amano, K., Terai, M., *Distribution of trace elements in the human body determined by neutron activation analysis.* Arch. Env. Health, 1980. **35**(1): p. 36-44.

8. Carl, G.F., Critchfield, J.W., Thompson, J.L., McGinnis, L.S., Wheeler, G.A., Gallagher, B.B., Holmes, G.L. Hurley, L.S., Keen, C.L., *Effect of kainate-induced seizures on tissue trace element concentrations in the rat.* Neuroscience, 1989. **33**(1): p. 223-227.

9. Kollmer, W.E., Schramel, P., Samsal, K., *Simultaneous determination of nine elements in some tissues of the rat using neutron activation analysis.* Phys. Med. Biol., 1972. **17**(4): p. 555-562.

10. Palm, R., Wahlstrom, G., Hallmans, G., *Age related changes in weight and concentrations of zinc and copper in the brain of the adult rat.* Lab. Anim., 1990. **24**: p. 240-245.

11. Takahashi, S., Hatashita, S., Taba, Y., Sun, X.Z., Kubota, Y., Yoshida, S., *Determination of the spatial distribution of major elements in the rat brain with X-ray fluorescence analysis.* J. Neurosci. Meth., 2000. **100**: p. 53-63.

12. Takahashi, S., Takahashi, I., Sato, H., Kubota, Y., Yoshida, S., Muramatsu, Y., *Determination of major and trace elements in the liver of Wistar rats by inductively coupled plasma-atomic emission spectrometry and mass spectrometry.* Lab. Anim., 2000. **34**: p. 97-105.

13. Takahashi, S., Sun, X.Z., Kubota, Y., Takai, N., Nojima, K., *Histological and elemental changes in rat brain after local irradiation with carbon ion beams.* J. Radiat. Res., 2002. **43**: p. 143-152.

14. Szerdahelyi, P., Kozma, M., Ferke, A. , *Zinc deficiency-induced trace element concentration and localization changes in the central nervous system of albino rat during postnatal development. II. Atomic absorption spectrophotometric examinations.* Acta. Histochemica, 1982. **70**(2): p. 172-182.

15. Bhatnagar, M., Rao, P., Bhatnagar, C., Bhatnagar, R., *Trace element concentration in various tissues following fluoride administration to female mice.* Indian J. Exp. Biol., 2003. **41**: p. 652-654.

16. Danielsen, A., Steinnes, E., *A study of some selected trace elements in normal and cancerous tissue by neutron activation analysis.* J. Nuclear Med., 1970. **11**(6): p. 260-264.

17. Garg, A.N., Weginwar, R.G., Chutke, N.L., *Radiochemical neutron activation analysis of Fe, Co, Zn, Sb, and Se in biomedical and environmental samples.* Sci. Total Env. , 1993. **139/140**: p. 421-430.

18. Yaman, M., Atici, D., Bakirdere, S., Akdeniz, I., *Comparison of Trace Metal Concentration in malign and Benign Human Prostate.* J. Med. Chem., 2005. **48**: p. 630-634.

19. Gulati, N., Mangal, P.C., *Trace element profiles in skin-tumor and tissues of tumor-bearing mice.* Indian J. Cancer, 1985. **22**: p. 308-314.

20. Mangal, P.C., Verma, K.B., *Effect of induced skin cancer on the concentrations of some trace elements in the mouse.* Indian J. Med. Res., 1979. **69**: p. 290-295.

21. Wei, Y.Y., Chung, C., *Analysis of experimental absorption and excretion in mice bearing malignant ascites* Biol. Trace Elem. Res., 1994. **43-45**: p. 397-403.

22. Geraki, K., Farquharson, M.J., Bradley, D.A., *X-ray fluorescence and energy dispersive x-ray diffraction for the quantification of elemental concentrations in breast tissue.* Phys. Med. Biol., 2004. **49**: p. 99-110.

23. Ng, K.H., Bradley, D.A., Looi, L.M., Seman Mahmood, C., Khalik Wood, A., *Differentiation of elemental composition of normal and malignant breast tissue by instrumental neutron activation analysis.* Appl. Radiat. Isot., 1993. **44**(3): p. 511-516.

24. Ng, K.H., Bradley, D.A., Looi, L.M. , *Elevated trace element concentrations in malignant breast tissues.* British J. Rad., 1997. **70**: p. 375-382.

25. Cesareo, R., Viezzoli, G., *Trace element analysis in biological samples by using XRF spectrometry with secondary radiation.* Phys. Med. Biol., 1983. **28**(11): p. 1209-1218.

26. Ward, N.I., Abou-Shakra, F.R., Durrant, S.F., *Trace elemental content of biological materials: a comparison of NAA and ICP-MS analysis.* Biol. Trace Elem. Res., 1989. **26-27**: p. 177-187.

27. Zeisler, R., Ostapczuk, P., Stone, S.F., Stoeppler, M., *Effective tools for trace element characterization of tissue: neutron activation analysis and voltammetry.* Sci. Total Env., 1993. **139/140**: p. 403-410.

28. Bender, J., Kapadia, AJ, Sharma, AC, Tourassi, GD, Harrawood, BP, Floyd, CE *Breast cancer detection using Neutron Stimulated Emission Computed Tomography: prominent elements and dose requirements.* Medical Phys., 2007. **34**(10).

29. Brewer, G., *Wilson Disease*, in *Harrison's Principles of Internal Medicine*, D. Kasper, Fawci, AS, Longo, DL, Braunwald, E, Hauser, SL, Jameson, JL, Editor. 2005, McGraw Hill: NY. p. 2313-2315.

30. Powell, L., *Hemochromatosis*, in *Harrison's Principles of Internal Medicine*, D. Kasper, Fawci, AS, Longo, DL, Braunwald, E, Hauser, SL, Jameson, JL, Editor. 2005, McGraw Hill: NY. p. 2298-2303.

31. Tierney, L., McPhee, SJ, Papadkis, MA, ed. *Current Medical Diagnosis and Treatment*. 45 ed. 2006, McGraw Hill: NY.

32. Wood, J., Wnriquez, C, Ghuge, N, Tyzka, JM, Carson, S, Nelson, MD, Coates, TD, *MRI R2 and R2* mapping accurately estimates hepatic iron concentration in transfusion-dependent thalassemia and sickle cell disease patients.* Blood, 2005. **106**(4): p. 1460-1465.

33. Bonkovsky, H., Rubin, RB, Cable, EE, Davidoff, A, Pels Rijcken, TH, Stark, DD, *Hepatic Iron Concentration: Noninvasive Estimation by Means of MR Imaging Techniques.* Radiology, 1999. **212**: p. 227-234.

34. Alustiza, J., Artexe, J, Castiella, A, Agirre, C, Emparanza, JI, Otazua, P, Garcia-Bengoechea, M, Barrio, J, Mujica, F, Recondo, JA, *MR quantification of Hepatic Iron Concentration.* Radiology, 2004. **230**: p. 479-484.

35. Angelucci, E., Giovagnoi, A, Valeri, G, Paci, E, Ripalti, M, Miretto, P, McLaren, C, Brittenham, GM, Lucarelli, G, *Limitations of Magnetic Resonance Imaging in Measurement of Hepatic Iron.* Blood, 1997. **90**(12): p. 4736-4742.

36. Villeneuve, J., Bilodeau, M, Lapage, R, Cote, J, Lefebvre, M, *Variability in hepatic iron concentration measurement from needle-biopsy specimens.* J. Hepatology, 1996. **25**: p. 172-177.

37. Fuentealba, C., Aburto, EM *Animal models of copper-associated liver disease.* Comp. Hepa., 2003. **2**(5).

38. Kato, J., Kobune, M, Kohgo, Y, Sugawara, N, Hisai, H, Nakamura, T, Sakamaki, S, Sawada, N, Niitsu, Y *Hepatic iron deprivation prevents spontaneous development of fulminant hepatitis and liver cancer in Long-Evans Cinnamon rats* J Clin. Invest., 1996. **98**: p. 923-929.

39. Malhi, H., Bhargava, KK, Afriyie, MO, Volenberg, I, Schilsky, ML, Palestro, CJ, Gupta, S, *99mTc-mebrofenin scintigraphy for evaluating liver disease in a rat model of Wilson's disease.* J. Nuc. Med., 2002. **43**(2): p. 246-252.

40. Sugawaraa, N., Ikedaa, T, Sugawaraa, C, Kohgob, Y, Katob, J, Takeichic, N *Regional distribution of copper, zinc and iron in the brain in Long-Evans Cinnamon (LEC) rats with a new mutation causing hereditary hepatitis.* Brain Res., 1992. **588**(2): p. 287-290.

41. Terada, K., Sugiyama, T, *The Long-Evans Cinnamon rat: an animal model for Wilson's disease.* Pediatr. Int. , 1999. **41**: p. 414-418.

42. Knoll, G.F., *Radiation Detection and Measurement*. 3 ed. 2000, Hoboken, NJ: Wiley.

43. Sharma, A., Tourassi, GD, Kapasia, AJ, Crowell, AS, Kiser, MR, Hutcheson, A, Harrawood, BP, Howell, CR., *NSECT: Elemental Composition of a Mouse.* Medical Phys, 2007. (to be submitted).

44. Kapadia, A.J., *Accuracy and Patient Dose in Neutron Stimulated Emission Computed Tomography for Diagnosis of Iron Overload: Simulations in GEANT4*, in *Dissertation Biomedical Engineering*. 2007, Duke University.

45. Floyd, C., Bender, JE, Sharma, AC, Kapadia, AJ, Xia, JQ, Harrawood, BP, Tourassi, GD, Lo, JY, Crowell, AS, Howell, CR., *Introduction to Neutron Stimulated Emission Computed Tomography.* Phys Med Biol, 2006. **51**: p. 3375-3390.

46. Bushberg, J., Seibert, JA, Leidholdt Jr, EM, Boone, JM, *The Essential Physics of Medical Imaging*. 2 ed. 2002, Philadelphia, PA: Lippincott Williams & Wilkins.

47. Webb, S., Binnie, DM, Flower, MA, Ott, RJ, *Monte Carlo modeling of the performance of a rotating slit-collimator for improved planar gamma-camera imaging.* Phys Med Biol, 1992. **37**(5): p. 1095-1108.

48. Macfarlane, D., Cotton, L, Ackerman, RJ, Minn, H, Ficaro, EP, Shreve, PD, Wahl, RL, *Triple Head SPECT with 2-[fluorine 18]fluoro-2-deoxy-D-glucose (FDG): Initial Evaluation in Oncology and Comparison with FDG PET.* Radiology, 1995. **194**: p. 425-429.

49. McGoron, A., Mao, X, Georgiou, MF, Kuluz, JW, *Computer phantom study of brain PET glucose metabolism imaging using a rotating SPECT/PET camera.* Computers in Bio. Med., 2005. **35**: p. 511-531.

50. Britten, A.J.a.K., R., *Performance assessment of a slat gamma camera collimator for 511 keV imaging.* Phys Med Biol, 1999. **44**: p. 1735-1741.

51. Kamali-Asl, A., Sarkar, S, Shahriari, M, Agha-Hosseini, H, *Slit slat collimator optimization with respect to MTF.* App. Rad. Isotopes, 2005. **62**: p. 461-468.

52. Lodge, M., Binnie, DM, Flower, MA, Webb, S, *The experimental evaluation of a prototype rotating slat collimator for planar gamma camera imaging.* Phys Med Biol, 1995. **40**: p. 427-448.

53. Lodge, M.A., Webb, S., Flower, M.A., Binnie, D.M., *A prototype rotating slat collimator for single photon emission computed tomography.* IEEE Trans. Med. Imag., 1996. **15**(4): p. 500-511.

54. Webb, S., Flower, MA, Ott, RJ, *Geometric efficiency of a rotating slit-collimator for improved planar gamma-camera imaging.* Phys Med Biol, 1993. **38**: p. 627-638.

55. Gagnon, D., Zeng, GL, Links, JM, Griesmer, JJ, Valentino, FC, *Design Considerations for a New Solid-State Gamma-Camera: SOLSTICE.* Proc. IEEE NSS, San Diego, 2001: p. 1156-1160.

56. Gagnon, D., Penn, MS, Lee, D, Urbain, JL, Tung, CH, Kline, B, Bender, PJ, Mercer, DL, Griesmer, JJ,, *Use of SOLSTICE Rotating-Slat Solid-State Camera for Small Animal Imaging.* Proc. IEEE NSS, Norfolk, 2002: p. 1367-1369.

57. Wang, W., Hawkins, W, Gagnon, D, *3D RBI-EM reconstruction with spherically-symmetric basis function for SPECT rotating slat collimator.* Phys Med Biol, 2004. **49**: p. 2273-2292.

58. Zeng, G., Gagnon, D, Mattherws, CG, Kolthammer, JA, Radachy, JD, Hawkins, WG, *Image reconstruction algorithm for a rotating slat collimator.* Medical Phys, 2002. **29**(7): p. 1406-1412.

59. Brzymialkiewicz, C., Tornai, MP, McKinley, RL, Bowsher, JE, *Evaluation of Fully 3-D Emission Mammotomography With a Compact Cadmium Zinc Telluride Detector.* IEEE TMI, 2005. **24**(7): p. 868-877.

60. Eisen, Y., Mardor, I, Shor, A, Baum, Z, Bar, D, Feldman, G, Cohen, H, Issac, E, Haham-Zada, R, Blitz, S, Cohen, Y, Glick, B, Falk, R, Rodebush, S, Blevis, I, *NUCAM3 - A Gamma Camera Based on Segmented Monolithic CdZnTe Detectors.* IEEE TNS, 2002. **49**(4): p. 1728-1732.

61. Muller, B., O'Conner, MK, Blevis, I, Rhodes, DJ, Smith, R, Collins, DA, Phillips, SW, *Evaluation of a Small Cadmium Zinc Telluride Detector for Scintimammography.* J Nuc Med, 2003. **44**(4): p. 602-609.

62. McGregor, D., Hermon, H, *Room-temperature compound semiconductor radiation detectors.* Nuc. Inst. Met. Phys. Resh., 1997. **395**: p. 101-124.

63. Hasegawa, B., Stebler, B, Rutt, BK, Martinez, A, Gingold, EL, Barker, CS, Faulker, KG, Cann, CE, Boyd, DP, *A prototype high-purity germanium detector system with fast photon-counting circuitry for medical imaging.* Medical Phys, 1991. **18**(5): p. 900-909.

64. Piqueras, I., Beck, FA, Duchene, G, Medina, P, Santos, C, Villaume, D, *Segmented germanium detector developments for Compton Camera application.* Nuc. Inst. Met. Phys. Resh. A, 2004. **525**: p. 275-278.

65. Vetter, K., Kuhn, A, Deleplanque, MA, Lee, IY, Stephens, FS, Schmid, GJ, Beckedahl, D, Blair, JJ, Clark, RM, Cromaz, M, Diamond, RM, Fallon, P, Lane, GJ, Kammeraad, JE, Macchiavelli, AO, Svensson, CE, *Three-dimensional position sensitivity in two-dimensionally segmented HP-Ge detectors.* Nuc. Inst. Met. Phys. Resh. A, 2000. **452**: p. 223-238.

66. Vetter, K., Burks, M, Mihailescu, L, *Gamma-ray imaging with position-sensitive HPGe detectors.* Nuc. Inst. Met. Phys. Resh. A, 2004. **525**: p. 322-327.

67. Karp, J., Surti, S, Daube-Witherspoon, ME, Freifelder, R, Cardi, CA, Adam, LE, Bilger, K, Muehllehner, G, *Performance of a brain PET camera based on Anger-logic gadolinium oxyorthosilicate detectors.* J. Nuc. Med., 2003. **44**(8): p. 1340-1349.

68. Ryan, J., Donmez, B, Macri, JR, McClish, M, McConnell, ML, Miller, RS, Widholm, M, Hamel, LA, Julien, M, *Development of CZT Strip Detector Modules for 0.05 to 1 MeV Gamma-Ray Imaging and Spectroscopy.* Proc. SPIE, 2003. **4851**: p. 885-894.

69. Hurford, G.J., Schmahl, E.J., Schwartz, R.A., Conway, A.J., Aschwanden, M.J., Csillaghy, A., Dennis, B.R., Johns-Krull, C., Krucker, S., Lin, R.P., McTiernen, J., Metcalf, T.R., Sato, J., Smith, D.M., *The RHESSI Imaging Concept.* Solar Physics, 2002. **210**(1-2): p. 61-86.

70. Lin, R.P., Dennis, B.R., Hurford, G.J., et. al., *The Reuven Ramety High-Energy Solar Spectroscopic Imager (RHESSI).* Solar Physics, 2002. **210**(1-2): p. 3-32.

71. Lin, R.P., Krucker, S., Hurford, G.J., Smith, D.M., Hudson, H.S., Holman, G.D., Schwartz, R.A., Dennis, B.R., Share, G.H., Murphy, R.J., Emslie, A.G., Johns-Krull, C., Vilmer, N., *REHSSI observations of particle acceleration and energy release in an intense solar gamma-ray line flare.* Astrophysical J, 2003. **595**: p. L69-L76.

72. Lin, R.P.P.I. *HESSI-SMEX Proposal*. 1997 [cited 2005; Available from: http://hesperia.gsfc.nasa.gov/~kim/toc.html.

73. Schnopper, H., Bradt, HV, Rappaport, S, Boughan, E, Burnett, B, Doxsey, R, Mayer, W, Watt, S., *Percise Location of Sagittarius X-ray sources with a Rocket-Borne Rotating Modulation Collimator.* Astrophysical J., 1970. **161**: p. L161-L167.

74. Webb, S., ed. *The Pysics of Medical Imaging*. Medical Science Series. 1988, Adam Hilger: Bristol.

75. Lange, K., Carson, R., *EM reconstruction algorithms for emission and transmission tomography.* J. Comp. Assist. Tomo., 1984. **8**(2): p. 306-316.

76. Sharma, A., Tourassi, GD, Kapadia, AJ, Harrawood, BP, Bender, JE, Crowell, AS, Kiser, MR, Howell, CR, Floyd Jr., CE, *Design and Development of a High-Energy Gamma Camera for use with NSECT Imaging: Feasibility for Breast Imaging.* IEEE TNS, 2007. **54**(5): p. 1498-1505.

77. Sharma, A., Floyd, CE, Harrawood, B, Tourassi, G, Kapadia, A, Bender, J, Lo, J, Howell, C., *Rotating slat collimator design for high-energy near-field imaging.* Proceedings of the 2006 SPIE Symposium on Medical Imaging, 2006. **6142**: p. 405-413.

78. Sharma, A., Turkington, TG, Tourassi, GD, Floyd, CE, *Near-Field High-Energy Spectroscopic Gamma Imaging Using a Rotation Modulation Collimator.* (to be submitted)

79. CERN, *GEANT4*, Available from: http://geant4.web.cern.ch/geant4/.

80. Sharma, A., Harrawood, BP, Bender, JE, Tourassi, GD, Kapadia, AJ, *Neutron Stimulated Emission Computed Tomography: a Monte Carlo simulation approach.* Phys. Med. Biol., 2007. **52**: p. 6117-6131.

81. MathWorks, *Matlab*.

82. Sharma, AC, Kapadia, AJ, Harraworrd, BP, Tourassi, GD. *Optimization of a Rotating Modulation Collimator for NSECT Imaging.* Proceedings of the 2007 IEEE NSS-MIC. Honolulu, HI, Nov. 2007.

Biography

Name: Amy Congdon Sharma

Date of Birth: May 18, 1979

Place of Birth: Fairfax, Virginia

Education

Duke University, Durham, NC

- Biomedical Engineering, PhD, December 2007
    - Dissertation: "Development and Design of a Near-Field High-Energy Gamma Camera for use with Neutron Stimulated Emission Computed Tomography"
- Biomedical and Electrical Engineering, BSE, May 2001
    - Departmental Graduation with Distinction – Biomedical Engineering
    - Pratt School of Engineering Undergraduate Research Fellow

Scholarship, Grants and Awards

NIH Training grant no. 1-T32-EB001040 (2003-2005)

Graduate Fellowship, Department of Biomedical Engineering, Duke University, Durham, NC (2005-2007)

Student Travel Award. Imaging and Neutrons 2006 Workshop, Spallation Neutron Source, Oak Ridge National Laboratory, Oak Ridge, TN, Oct 2006.

IEEE 2006 MIC Trainee Award. IEEE NSS-MIC. San Diego, CA, Nov. 2006.

Student Travel Award. NRBC 2006 Workshop, IEEE NSS-MIC. San Diego, CA, Nov. 2006.

Member IEEE

Yearbook of Nuclear Medicine Abstract Selection:

Publication titled "Introduction to Neutron Stimulated Emission Computed Tomography" selected for abstraction, 2006

Peer Reviewed Publications

Sharma, AC, Harrawood, BP, Bender, JE, Tourassi, GD, Kapadia, AJ. "Neutron Stimulated Emission Computed Tomography: a Monte Carlo Simulation Approach." *Phys. Med. Biol.*, vol. 52, pp 6117-6131, Oct 2007.

Sharma, AC, Tourassi, GD, Kapadia, AJ, Harrawood, BP, Crowell, AS, Kiser, MR, Howell, CR, Floyd, CE. "Design and Development of a High-Energy Gamma Camera for use with NSECT Imaging: Feasibility for Breast Imaging." *IEEE TNS,* vol. 54, no. 5, pp 1498-1505, Oct 2007.

Bender, JE, Kapadia, AJ, **Sharma, AC**, Tourassi, GD, Harrawood, BP, Floyd, CE Jr., "Breast cancer detection using Neutron Stimulated Emission Computed Tomography: prominent elements and dose requirements," *Medical Physics*, vol. 34, no.10, pp 3866-3871, Oct 2007.

Kapadia, AJ, **Sharma, AC**, Bender, JE, Tourassi, GD, Howell, CR, Crowell, AS, Kiser, MR, Harrawood, BP, Floyd, CE. "Neutron Stimulated Emission Computed Tomography for Diagnosis of Breast Cancer." *IEEE TNS* (in press July 2007).

Floyd, CE, **Sharma, AC**, Bender, JE, Kapadia, AJ, Xia, JQ, Harrawood, BP, Tourassi, GD, Lo, JY, Kiser, MR, Crowell, AS, Pedroni, RD, Marci, RA, Tajima, S, Howell, CR. "Neutron Stimulated Emission Computed Tomography: Background Corrections." *Nuc. Inst. And Meth. B.* vol. 254, no. 2, pp 329-336, Jan 2007.

Floyd, CE, Bender, JE, **Sharma, AC**, Kapadia, AJ, Xia, J, Harrawood, BP, Tourassi, GD, Lo, JY, Crowell, A, Howell, CR. "Introduction to Neutron Stimulated Emission Computed Tomography." *Phys Med Biol.* vol. 51, pp 3375-3390, Jul. 2006. URL: http://stacks.iop.org/0031-9155/51/3375
**** Abstract in the *Yearbook of Nuclear Medicine***

Palmeri, ML, **Sharma, AC**, Bouchard, RR, Nightingale, RW, Nightingale, KR. "A Finite Element Method Model of Soft Tissue Response to Impulsive Acoustic Radiation Force," *IEEE Trans. Ultrason., Ferroelect., Freq. Contr.*, vol. 52, no. 10, pp. 1699-1712, Oct. 2005.

Manuscripts to be Submitted

Floyd, CE, Kapadia, AJ, Bender, JE, **Sharma, AC**, Xia, JQ, Harrawood, BP, Tourassi, GD, Lo, JY, Corwell, AS, Kiser, MR, Howell, CR. "Neutron Stimulated Emission Computed Tomography of a Multi-element Phantom."

Sharma, AC, Tourassi, GD, Turkington, TG, Floyd, CE. "Near-Field High-Energy Spectroscopic Gamma Imaging Using a Rotation Modulation Collimator."

Sharma, AC, Tourassi, GD, Kapasia, AJ, Crowell, AS, Kiser, MR, Hutcheson, A, Harrawood, BP, Howell, CR. "NSECT: Elemental Composition of a Mouse."

Conference Proceedings

Sharma, AC, Kapadia, AJ, Harraworrd, BP, Tourassi, GD. "Optimization of a Rotating Modulation Collimator for NSECT Imaging." *Proceedings of the 2007 IEEE NSS-MIC*. Honolulu, HI, Nov. 2007.

Sharma, AC, Tourassi, GD, Kapadia, AJ, Crowell, AS, Kiser, MR, Hutcheson, A, Harrawood, BP, Howell, CR, Floyd, CE. "Elemental Spectrum of a Mouse Obtained via Neutron Stimulation." *Proceedings of the 2007 SPIE Symposium on Medical Imaging*, vol. 6510, 65100K, 2007.

Sharma, AC, Tourassi, GD, Kapadia, AJ, Bender, JE, Xia, JQ, Harrawood, BP, Crowell, AS, Kiser, MR, Howell, CR, Floyd, CE. "Development of a High-Energy Gamma Camera for use with NSECT Imaging of the Breast." *Proceedings of the 2006 IEEE NSS-MIC*. San Diego, CA Nov. 2006.

Sharma, AC, Tourassi, GD, Kapadia, AJ, Harraworrd, BP, Bender, JE, Crowell, AS, Kiser, MR, Howell, CR, Floyd, CE. "Design and Construction of a Prototype Rotation Modulation Collimator for Near-Field High-Energy Spectroscopic Gamma Imaging," *Proceedings of the 2006 IEEE NSS-MIC*. San Diego, CA, Nov. 2006.

Kapadia, AJ, **Sharma, AC**, Tourassi, GD, Bender, JE, Howell, CR, Crowell, AS, Kiser, MR, Floyd, CE. "Neutron Spectroscopy of Mouse Using Neutron Stimulated Emission Computed Tomography (NSECT)," *Proceedings of the 2006 IEEE NSS-MIC.* San Diego, CA Nov. 2006.

Kapadia, AJ, **Sharma, AC**, Tourassi, GD, Bender, JE, Howell, CR, Crowell, AS, Kiser, MR, Floyd, CE. "Neutron Stimulated Emission Computed Tomography (NSECT) for Early Detection of Breast Cancer," *Proceedings of the 2006 IEEE NSS-MIC.* San Diego, CA Nov. 2006.

Kapadia, AJ, **Sharma, AC**, Tourassi, GD, Bender, JE, Howell, CR, Crowell, AS, Kiser, MR, Floyd, CE. "Non-Invasive Estimation of Potassium (39K) in Bovine Liver Using Neutron Stimulated Emission Computed Tomography (NSECT)," *Proceedings of the 2006 IEEE NSS-MIC.* San Diego, CA Nov. 2006.

Sharma, AC, Floyd, CE, Harrawood, B, Tourassi, G, Kapadia, A, Bender, J, Lo, J, Howell, C. "Rotating slat collimator design for high-energy near-field imaging" *Proceedings of the 2006 SPIE Symposium on Medical Imaging*, vol. 6142, pp. 405-413, 2006.

Floyd, CE, Bender, JE, Harrawood, BP, **Sharma, AC**, Kapadia, AJ, Tourassi, GD, Lo, JY, Howell, CR. "Breast cancer diagnosis using Neutron Stimulated Emission Computed Tomography: Dose and Count requirements." *Proceedings of the 2006 SPIE Symposium on Medical Imaging*, vol. 6142, pp. 597-603, 2006.

Bender, JE, Floyd, CE, Harrawood, BP, Kapadia, AJ, **Sharma, AC**, Jesneck, JL. "The Effect of Detector Resolution for Quantitative Analysis of Neutron Stimulated Emission Computed Tomography." *Proceedings of the 2006 SPIE Symposium on Medical Imaging*, vol. 6142, pp. 1597-1605, 2006.

Nightingale, KR, MS, Palmeri, ML, Frinkley, KD, **Sharma, AC**, Zahi, L, Trahey, GE. "Ultrasonic Imaging of the Mechanical Properties of Tissues Using Localized, Transient Acoustic Radiation Force," *Proceedings of the 2005 ICASSP*, 2005.

Sharma, AC, Trahey, GE, Frinkley, KD, Soo, MS, Nightingale, KR. "Image processing and data acquisition optimization for Acoustic Radiation Force Impulse imaging of in vivo breast masses." *Proceedings of the 2005 SPIE Symposium on Medical Imaging*, vol. 5750, pp. 205-215, 2005.

Sharma, AC, Soo, MS, Trahey, GE, Nightingale, KR. "Acoustic Radiation Force Impulse Imaging of In Vivo Breast Masses," *Proceedings of the 2004 IEEE Ultrasonics Symposium*, vol. 1, pp. 728-731, 2004.

Nightingale, KR, Soo, MS, Palmeri, ML, **Congdon, AN**, Frinkley, KD, Trahey, GE. "Imaging Tissue Mechanical Properties Using Impulsive Acoustic Radiation Force," *Proceedings of the 2004 IEEE International Symposium on Biomedical Imaging Macro to Nano*, vol. 1, pp. 41-44, 2004.

Congdon, AN, Foley, JL. "Motorized Swing for Child up to Fifty Pounds," *RESNA 2001 Annual Conference Proceedings*. Reno, NV, June 22-26, 2001. 376-378.

Gallippi, CM, Bohs, LN, Anderson, ME, **Congdon, AN**, Trahey, GE. "Lateral Blood Velocity Measurement in the Carotid Artery via Speckle Tracking," *2001 IEEE Ultrasonics Symposium*, vol. 2, pp. 1451-1455, 2001.

Abstracts

Gallippi, CM, Bohs, LN, Anderson, ME, Hernandez-Soria, MS, **Congdon, AN**, Trahey, GE. "Lateral Flow Measurement in the Carotid Artery Using Speckle Tracking." *Ultrasonic Imaging*, vol. 2, pp. 259, 2001.

Posters

Sharma, AC, Tourassi, GD, Harrawood, BP, Kapadia, AJ, Floyd, CE. "Neutron Stimulated Emission Computed Tomography: 2D planar reconstruction of high energy gammas," *Society of Nuclear Medicine 54th Annual Meeting*, Washington, DC, June 2007.

Sharma, AC, Tourassi, GD, Kapadia, AJ, Harraworrd, BP, Crowell, AS, Kiser, MR, Howell, CR, Floyd, CE. "Near-Field High-Energy Gamma Camera for Neutron Stimulated Emission Computed Tomography (NSECT)," *Imaging and Neutron 2006 Workshop*, Spallation Neutron Source, Oak Ridge National Laboratory, Oak Ridge, TN, Oct 2006.

Palmeri, ML, Trahey, GE, Frinkley, KD, **Congdon, AN**, Nightingale, KR. "Imaging tissue mechanical properties using impulsive acoustic radiation force", *Opening conference on interdisciplinary inverse problems at the center for inverse problems at Rensselaer Polytechnic Institute*, 2004.

Congdon, AN, Shih, TE. "Peak Flow Meter." *Biomedical Engineering Society Annual Meeting*. Seattle, WA, October 2000.